Sensitivity studies for the KATRIN experiment

Zur Erlangung des akademischen Grades eines
DOKTORS DER NATURWISSENSCHAFTEN
von der Fakultät für Physik
des Karlsruher Instituts für Technologie
genehmigte
DISSERTATION
von

Diplom-Physiker Wolfgang Käfer
aus Emmendingen

Angefertigt am Institut für Experimentelle Kernphysik
der Fakultät für Physik
des Karlsruher Instituts für Technologie

Erstgutachter:	Prof. Dr. G. Drexlin
Zweitgutachter:	Prof. Dr. W. de Boer

Tag der mündlichen Prüfung: 27.01.2012

KIT - University of the state of Baden-Wuerttemberg and National Research Center of the Helmholtz Association www.kit.edu

Contents

1. Introduction

From the initial proposal of the neutrino by W. Pauli in 1930 as a desperate measure to explain the continuous energy spectra observed in β-decay and their subsequent discovery 26 years later by Cowan and Reines, neutrino physics has evolved to an interesting and fruitful research field in its own right. It provides many interesting insights in the fundamental properties of nature and the history of the universe. In particular, neutrino physics may play a key role in answering important questions, such as:

- What is the energy composition of the universe?
- How did galaxies and galaxy clusters form?
- Why is there matter but no antimatter?
- What happens during a supernovae explosion?
- What are the conditions inside the sun and other stars?

In particular, one fundamental property of the neutrino remains so far undetermined, its rest mass. As discussed in chapter 2, which contains an overview of the current state of neutrino physics, the neutrino mass plays a prominent role in several of these questions. While the neutrino was assumed to be massless for a long time, recent experimental evidence for neutrino oscillations between the three neutrino flavors by the SNO and Super-Kamiokande experiments implies a non-zero rest mass. Since neutrino oscillations are only sensitive to the differences between the squared masses of the different neutrino mass eigenstates, the absolute masses remain unknown. This so far undetermined neutrino mass scale is of interest both as a fundamental ingredient to our understanding in the fundamental properties of matter and as an important parameter in precision cosmology, where the neutrino contributions as hot dark matter influence the formation of structures like galaxy clusters in the universe.

The discovery of neutrino oscillations has renewed the interest in a direct, model independent laboratory measurement of the neutrino mass. The most promising

approach involves the investigation of the kinematics in the β-decay of tritium, where a non-zero neutrino mass manifests itself as missing energy of the decay-electron. So far, only an upper bound of

$$m_{\overline{\nu_e}} < 2.0 \text{ eV} \qquad (90\% \text{ C.L.}) \tag{1.1}$$

has been derived by the Particle Data Group, based on the latest results of the most recent experiments of this type, the Mainz and Troitsk experiments. Upper bounds for the other two neutrino flavors also exist, but are several orders of magnitude above this upper limit.

The KArlsruhe TRItium Neutrino experiment (KATRIN) introduced in chapter 3 is the immediate successor of the Mainz and Troitsk experiments and aims to improve the sensitivity on the neutrino mass to 200 meV (90% C.L.). It uses the same method as its predecessors and investigates the shape of the β-decay spectrum of Tritium. The KATRIN experiment is currently under construction at the Karlsruhe Institute of Technology (KIT). In order to achieve this improvement by an order of magnitude, a dedicated simulation framework to fully understand the properties of the more than 70 m long complex KATRIN experiment is mandatory. This thesis contributes significantly to the development of this simulation framework called Kassiopeia, which is described in chapter 4.

Experience from previous experiments has shown that most of the systematic uncertainties which ultimately limit the sensitivity of an such a β-decay experiment are associated with the tritium source. Improving the understanding of the influence of experimental conditions, in particular from inhomogeneities of important experimental parameters, on the β-spectrum measured in KATRIN is the second major motivation for this thesis. In this context, specific simulation and analysis modules which allow to investigate this influence in unprecedented detail have been developed as part of this thesis. These modules are described in chapter 5. The first module is dedicated to the calculation of β-decay spectra taking into account the experimental conditions within KATRIN. This in turn is used by the two other modules described in this thesis: The event generator framework as part of the trajectory calculation methods within Kassiopeia allows to simulate signal and background processes on an event by event basis. Additionally, an analysis module has been developed, which is being used to investigate the influence of these experimental parameters on the KATRIN sensitivity.

The results of several sensitivity studies performed during this thesis are summarized in chapter 6, starting with the verification of the analysis chain and focusing on the impact of current results from specific test experiments on the systematic uncertainty of KATRIN. Additionally, this chapter contains a sensitivity study for a envisioned second phase of KATRIN. This second phase would feature a detector with a significantly improved energy resolution of about 1 eV, which is three orders of magnitude better than the current detector system.

2. Neutrinos

This chapter gives an overview over the different roles of neutrinos for fundamental physics. The first part of this chapter, Sec. 2.1, is dedicated to the impact of neutrinos in fundamental physics. Of particular importance in the context of this thesis are on-going efforts to determine the masses of neutrinos, which are discussed in Sec. 2.2.

2.1 History, Status and Perspectives of Neutrino Physics

Beginning with a short historical overview in Sec. 2.1.1, this section provides a compact summary of our knowledge about neutrinos, focusing on a short introduction to neutrino oscillations in Sec. 2.1.2 and the role of neutrinos in cosmology in Sec. 2.1.3.

2.1.1 A short history of neutrinos

The neutrino was proposed by W. Pauli in 1930 to solve the mystery of the continuous energy spectra observed in β-decay. The nucleus was believed to consist of discrete energy levels, a picture supported by the discrete lines observed in α and γ decay but at odds with the continuous energy spectrum of β-decay first observed in 1911 by L. Meitner and O. Hahn and 1914 by J. Chadwick. This discovery was met with great skepticism from the beginning and continued to puzzle many scientists. Some scientists even proposed some form of energy non-conservation to explain this unexpected result. Eventually, Pauli proposed the existence of a novel particle participating in the decay, the neutrino, in his famous letter to the "radioactive Ladies and Gentlemen" [1]. This explanation turned out to be correct. In Pauli's case, β-decay is a three body process with the neutron n decaying in a proton p, an electron e and a neutrino[1] $\overline{\nu_e}$

$$n \rightarrow p + e + \overline{\nu_e}. \tag{2.1}$$

[1] in modern terminology, an electron anti-neutrino

In a three body process, the total energy of electron and neutrino is conserved while the energy of the electron is continuous and the undetected neutrino takes away the missing energy. Pauli concluded that the neutrino must have spin $\frac{1}{2}$ and be electrically neutral to conserve angular momentum and charge. Furthermore, it must be extremely light and interact only weakly with ordinary matter, in order to explain the lack of experimental evidence for its existence. Based on this proposal, E. Fermi developed his extremely successful theory of β-decay [2] shortly after in 1934, however it took over 20 years until the neutrino could be directly observed experimentally: In 1956, Cowan and Reines successfully proved the existence of the electron anti-neutrino by measuring the cross section of the inverse β-decay

$$p^+ + \overline{\nu_e} \rightarrow n + e^+. \tag{2.2}$$

In order to achieve a sufficient flux of anti-neutrinos, a nuclear reactor was used as neutrino source. The neutrinos then interacted with protons inside a tank of CdCl solution, creating neutrons and positrons [3]. The annihilation photons of the positrons together with a delayed signal from the neutrons using Cd as neutron absorber served as a clear signature and eventually led to the successful measurement of the inverse β-decay and the discovery of the electron anti-neutrino.

Shortly thereafter in 1962, the muon neutrino joined the particle zoo [4]: Lederman, Schwartz and Steinberger [5] were able to show that the neutrinos produced in the reaction $\pi^\pm \rightarrow \mu^\pm + \nu$ produce only muons and no electrons when interacting with matter. Hence they must be fundamentally different from electron neutrinos. This second neutrino species fit nicely in the then emerging Standard Model of particle physics. Finalized in the 1970s, this model has been a remarkable success for over 40 years and explains the interactions of the smallest constituents of matter we know. Its constituents are shown in Fig. 2.1.

Apart from the elusive Higgs Boson, all particles of the Standard Model (SM) have been detected. The latest discovered is the τ neutrino. However, after the discovery of the third charged lepton – the τ at SLAC in 1975 – the existence of the τ neutrino was expected long before its discovery. Additional indirect evidence for the existence of the τ neutrino was provided by the determination of the number of light neutrino flavors to be 2.84 ± 0.16 at the LEP collider [6]. However, it took 25 years until it was finally directly observed by the DONUT collaboration [7]. This again highlights the tiny cross sections for neutrinos compared to other particles.

The SM assumes neutrinos to be electrically neutral and massless. Furthermore, due to the maximal parity violating structure of the weak interaction, it contains only left-handed neutrinos, therefore it is impossible that they acquire mass via Yukawa couplings to the Higgs as the other fermions do. However, as will be discussed in Sec. 2.1.2, there is now clear experimental evidence from several experiments [8, 9, 10] for neutrino flavor oscillations. Such flavor changes are only possible for massive neutrinos.

In retrospect, the first evidence for neutrino oscillations is over 40 years old. Already in the 1960s, the solar neutrino problem emerged: The sun creates energy via fusion processes, in particular the $p-p$ cycle, and therefore is a huge neutrino emitter [11]. Starting with the Homestake experiment [12], experiments measuring the solar electron neutrino flux consistently measured a lower value than predicted

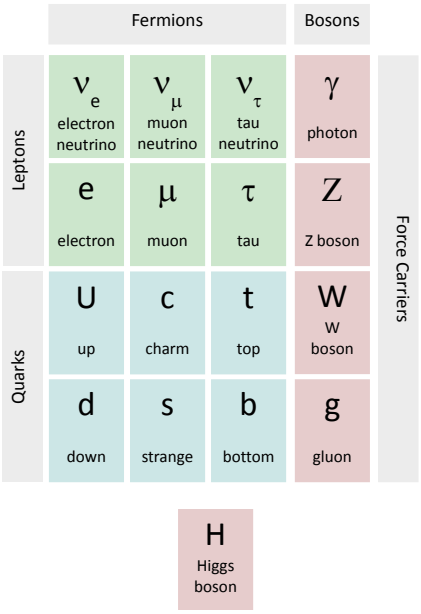

Figure 2.1: **The Standard Model of particle physics**. According to the Standard Model, all ordinary matter consists of 12 fermions with spin $\frac{1}{2}$, 6 quarks and 6 leptons. These fermions interact via gauge bosons: 8 gluons, mediating the strong force, $W^{\pm}$ and Z bosons of the weak interaction and the Photon γ of electromagnetism. The fermions acquire mass via the Higgs mechanism, which introduces so-called Yukawa couplings between their left- and right handed components and the Higgs. Due to the strong force, free quarks cannot be observed, but they immediately combine either to quark-anti-quark pairs (Mesons), or to bound three-quark states like proton and neutron (Hadrons).

by the Standard Solar Model (SSM) (see e.g.. [13] and Fig. 2.2). As a function of the lower energy threshold of the different experiments, only about 30 - 50% of the expected neutrino flux has been observed.

There are two explanations for this: either the SSM is incorrect or the electron neutrinos oscillate on the way to the earth into other flavors. Only at the beginning of this century, this mystery was finally resolved and the second option could be confirmed. The experiments SNO in the Sudbury mine in Canada and Super-Kamiokande in the Kamioka mine in Japan have published evidence for neutrino oscillations. In the case of SNO, the experiment was sensitive to all neutrino flavors via specific detection techniques and indeed found that, while the total solar neutrino flux is in agreement with predictions based on the SSM, only a fraction of them actually arrive as electron neutrinos [8]. The others oscillated into other flavors (ν_μ, ν_τ) on their way to the earth. Super-Kamiokande found the first evidence for oscillation of atmospheric neutrinos [9], which are produced by interactions of cosmic radiation with the atmosphere of the earth. Long base line experiments, in particular K2K, MINOS and KamLAND [14, 15, 16] were able to confirm this result

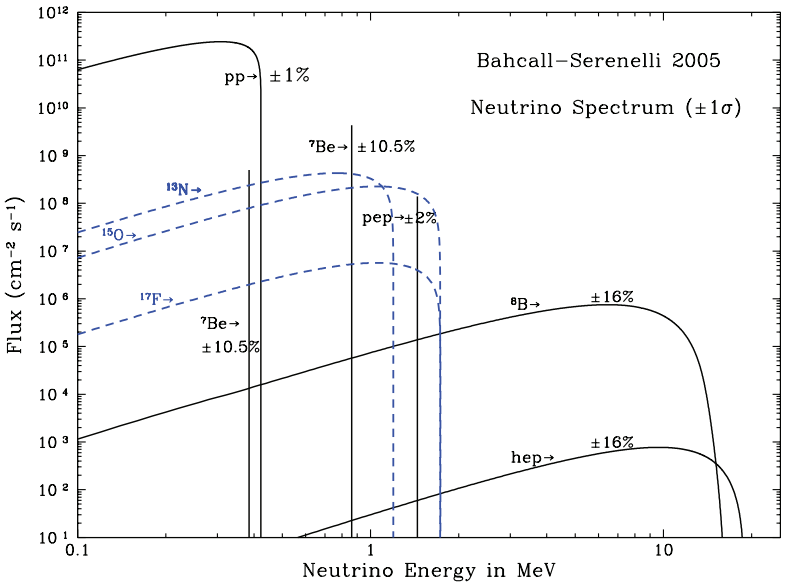

Figure 2.2: **The solar neutrino spectrum** as calculated by Bahcall et. al. Several fusion processes in the sun produce neutrinos with either continuous or discrete energy. Most experiments are sensitive only to the high energetic ^{8}B cycle. The experiment with the currently lowest energy threshold is BOREXINO. It is the first experiment sensitive to the ^{7}Be contribution. The figure is taken from [6].

using artificial neutrino sources. Super-Kamiokande is also in agreement with the SNO result for solar electron neutrinos [10].

Since the Standard Model of particle physics assumes neutrinos to be massless, the detection of flavor oscillations, which are only possible for massive neutrinos, is the first experimental evidence for physics beyond the Standard Model. Because of the importance of this result and the close connection between neutrino oscillations and neutrino masses, the following section will give a brief introduction to the formalism of neutrino mixing, based on [6] and an overview of the experimental results.

2.1.2 Neutrino oscillations

Theoretical framework

There are two prerequisites for neutrino oscillations: The mass eigenstates of the different neutrinos $i = 1, 2, 3$ must not be identical to the flavor eigenstates $\alpha = e, \mu, \tau$, so that different mass eigenstates mix with each other. Additionally, the mass eigenvalues must differ from each other. The mass eigenstates can be obtained from the flavor eigenstates via a unitary transformation U. The matrix representation of U is usually called PMNS matrix[2] and is the analogue of the CKM[3] matrix in the quark sector:

$$|\nu_\alpha\rangle = \sum_{i=1}^{3} U_{\alpha i} |\nu_i\rangle \tag{2.3}$$

[2]after B. Pontecorvo, Z. Maki, M. Nakagawa and S. Sakata
[3]after N. Cabbibo, M. Kobayashi and T. Maskawa

or vice versa:

$$|\nu_i\rangle = \sum_\alpha U^\dagger_{i\alpha}|\nu_\alpha\rangle = \sum_\alpha U^*_{\alpha i}|\nu_\alpha\rangle \tag{2.4}$$

The unitary matrix U is usually parametrized with 3 angles and 1 + 2 phases:

$$\begin{aligned}\begin{pmatrix} U_{e1} & U_{e2} & U_{e3} \\ U_{\mu 1} & U_{\mu 2} & U_{\mu 1} \\ U_{\tau 1} & U_{\tau 2} & U_{\tau 3} \end{pmatrix} = &\begin{pmatrix} 1 & 0 & 0 \\ 0 & c_{23} & s_{23} \\ 0 & -s_{23} & c_{23} \end{pmatrix} \cdot \begin{pmatrix} c_{13} & 0 & s_{13}e^{-i\delta} \\ 0 & 1 & 0 \\ -s_{13}e^{i\delta} & 0 & c_{23} \end{pmatrix} \\ &\cdot \begin{pmatrix} c_{12} & s_{12} & 0 \\ -s_{12} & c_{12} & 0 \\ 0 & 0 & 1 \end{pmatrix} \cdot \begin{pmatrix} e^{i\alpha_1/2} & 0 & 0 \\ 0 & e^{i\alpha_2/2} & 0 \\ 0 & 0 & 1 \end{pmatrix}\end{aligned} \tag{2.5}$$

where c_{ij} and s_{ij} denote the cosine and sine of the mixing angles θ_{ij} and δ is a CP-violating phase. The phases α_1 and α_2 are only meaningful if neutrinos are their own anti-particles (Majorana neutrinos) and play no role in neutrino oscillations.

The typical experimental scenario is the following: A neutrino is produced in a flavor eigenstate $|\nu_\alpha\rangle$ through the weak interaction. Then it propagates to a distance L where it is detected in the flavor state $|\nu_\beta\rangle$. The detector may be sensitive to one or more neutrino flavors. If $\beta = \alpha$, the experiment is usually referred to as 'disappearance experiment', for $\beta \neq \alpha$ the term 'appearance experiment' is used.

In relativistic quantum mechanics, the wave function of a neutrino mass eigenstate $|i\rangle$ at time t will evolve as[4]:

$$|\nu_i(t)\rangle = e^{-i(E_i t - pL)}|\nu_i\rangle \approx e^{-i(m_i^2/2p)L}|\nu_i\rangle \tag{2.6}$$

using

$$E_i = \sqrt{p^2 + m_i^2} \approx p + \frac{m_i^2}{2p} \qquad \text{and} \qquad L \approx t \tag{2.7}$$

This already implies that neutrino mass eigenstates with different eigenvalues build up a phase difference as they propagate and thus can interfere with each other and neutrino oscillations will occur.

To quantify this, one needs to compute the transition probability $P(\alpha \to \beta, t)$ to measure a neutrino produced at time $t = 0$ in a flavor eigenstate α with flavor β at time $t > 0$.

$$P(\alpha \to \beta, t) = \left|\langle \nu_\beta | \nu(t)\rangle\right|^2 . \tag{2.8}$$

Inserting the wave function of a neutrino starting in a flavor eigenstate α at time $t = 0$

$$|\nu_\alpha(t)\rangle = \sum_i U_{\alpha i} e^{-i\frac{m_i^2}{2p}L}|\nu_i\rangle \tag{2.9}$$

[4]unless stated otherwise, natural units are used throughout this thesis: $\hbar = c = 1$

in Eq. (2.8) leads to

$$\begin{aligned} P(\alpha \to \beta, t) &= \left| \sum_j \langle \nu_j | U^*_{j\beta} \sum_i U_{\alpha i} e^{-i m_i^2/2p)L} | \nu_i \rangle \right|^2 \\ &= \left| \sum_i U^*_{i\beta} U_{\alpha i} e^{-i \frac{m_i^2}{2p} L} \right|^2 \\ &= \delta_{\alpha\beta} - 4 \sum_{j>i} Re \left(U^*_{\alpha i} U_{\beta i} U_{\alpha j} U^*_{\beta j} sin^2 \frac{m_j^2 - m_i^2}{4} \frac{L}{E} \right) \\ &\quad + 2 \sum_{j>i} Im \left(U^*_{\alpha i} U_{\beta i} U_{\alpha j} U^*_{\beta j} sin \frac{m_j^2 - m_i^2}{2} \frac{L}{E} \right) \end{aligned} \tag{2.10}$$

The oscillating term $\frac{m_j^2 - m_i^2}{4} \frac{L}{E}$ motivates the definition of the neutrino oscillation length

$$L^\nu_{ij} = \frac{4E}{\Delta m^2_{ij}} \qquad \text{with} \qquad \Delta m^2_{ij} = m_i^2 - m_j^2. \tag{2.11}$$

This length should ideally be of the order of the source-detector distance L, otherwise the oscillations will not have time to develop before neutrinos reach the detector.

MSW effect

The presence of matter can have a significant influence on neutrino oscillations: coherent elastic scattering causes neutrinos to have different effective masses in a medium, which can cause a resonant amplification of the oscillation probability. This is usually called the MSW effect[5], however the details go beyond this thesis. The MSW effect is of interest with respect to neutrino propagation in the center of stars like the sun. In the future, this effect could be used to probe the interior of the earth as well [6].

Two flavor model

As it turns out, the mixing angle θ_{13} is rather small, therefore it is instructive to limit ourselves to 2 neutrino flavors. In this case, there is only one angle and no phase and the mixing matrix simplifies to

$$\begin{pmatrix} \cos\theta & \sin\theta \\ -\sin\theta & \cos\theta \end{pmatrix}, \tag{2.12}$$

and the oscillation probability is (cf. Fig 2.3):

$$P(\alpha \to \beta, t) = \delta_{\alpha\beta} - \frac{1}{2} \sin^2 2\theta \cos \frac{\Delta m^2 L}{2E} = \delta_{\alpha\beta} - \sin^2 2\theta \sin \frac{\Delta m^2 L}{4E} \tag{2.13}$$

Because θ_{13} is small and the two mass differences and thus the oscillation lengths differ by two orders of magnitude, many neutrino experiments can (and do) interpret their results in a two flavor model. In this case, $\theta_\odot = \theta_{12}$ and $\Delta m_\odot = \Delta m_{12}$ are associated with solar neutrino oscillations and $\theta_{atm} = \theta_{23}$ and $\Delta m_{atm} = \Delta m_{23} \approx \Delta m_{13}$

[5] named after L. Wolfenstein, S. Mikheyev and A. Smirnov for pioneering work in this area [17].

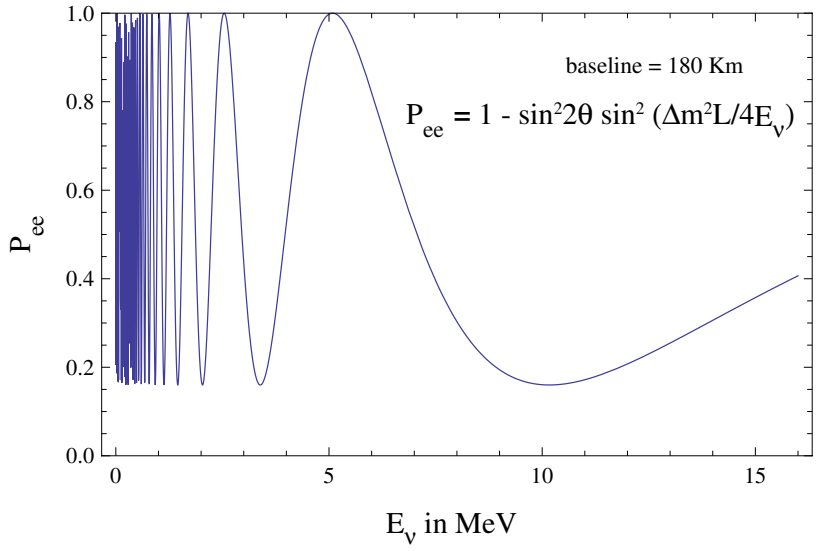

Figure 2.3: ν_e ($\overline{\nu_e}$) **survival probability** as a function of energy for the following exemplary values: $L = 180$ km, $\Delta m^2 = 7 \cdot 10^{-5}$ eV^2 and $\sin^2 2\theta = 0.84$ [6].

with the dominant ν_μ (and $\overline{\nu_\mu}$) oscillations of atmospheric neutrinos. These muon (anti)neutrinos are produced in the atmosphere via cosmic rays and are believed to oscillate into tau (anti)neutrinos, since there is no indication of electron neutrino appearance and the OPERA experiment has successfully detected the first ν_τ from a ν_μ beam [18].

Experimental status

Since the first observation of neutrino oscillations by SNO and Super-Kamiokande using solar and atmospheric neutrinos, other experiments have confirmed these results using artificial neutrino sources. Suitable sources are either nuclear reactors with a neutrino energy of about 1 MeV or particle accelerators with a neutrino energy typically around 1 GeV. From Eq. (2.11) follows, that long baseline experiments (several hundred kilometers) are sensitive to Δm_{12} using reactor neutrinos or to Δm_{23} using accelerator neutrinos. Oscillations involving $\Delta m_{13} \approx \Delta m_{23}$ can also be probed using reactor neutrinos with a baseline of about 1 km, which is particular interesting in the on-going hunt for θ_{13}.

The current values [6] obtained using data from several experiments are summarized in Tbl. 2.1: The KamLAND experiment has confirmed the results obtained

Table 2.1: **Neutrino oscillation parameters** [6].
With the exception of the limit on $\sin^2 2\theta_{13}$ from CHOOZ, errors are 99.73% C.L..

Parameter	value	Parameter	value
$\sin^2 2\theta_{12}$	0.87(3)	Δm^2_{12}	$7.59(20) \cdot 10^{-5}$ eV^2
$\sin^2 2\theta_{13}$	< 0.15(90%C.L.)	$\lvert\Delta m_{23}\rvert^2$	$2.43(13) \cdot 10^{-3}$ eV^2
$\sin^2 2\theta_{23}$	> 0.92		

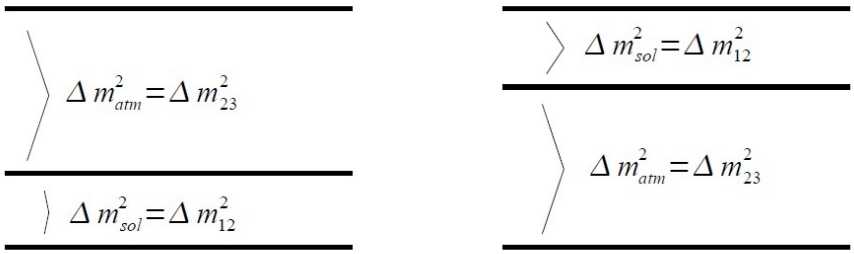

Figure 2.4: **Inverted and normal hierarchy for neutrino masses**. Since the sign of Δm^2_{23} is unknown, is is possible to arrange the neutrino masses in two different orders, either in the normal hierarchy shown left or the inverted hierarchy in the right plot.

from solar neutrino oscillation in Ref. [16] by investigating the flux from about 50 nuclear reactors surrounding the Kamioka mine in Japan, using 1 kt of liquid scintillator as detector material. Similarly, the K2K experiment directed muon neutrinos obtained from the 12 GeV proton beam at KEK to the Kamioka mine where they were detected with Super-Kamiokande. K2K was able to confirm the atmospheric neutrino parameters [14]. Furthermore, the Borexino experiment is currently investigating solar neutrinos oscillations with a lower energy threshold than its predecessors, measuring for the first time the ^{7}Be neutrino flux as well as the ^{8}B flux. Initial results [19, 20] are consistent with predictions by the solar model including the MSW effect mentioned above.

For θ_{13}, presently only an upper bound of $\sin^2 2\theta_{13} < 0.15 - 0.2$ (90% C.L.)[6] is known from the CHOOZ experiment [21]. The main systematic influence at CHOOZ was the knowledge of the neutrino flux from the used reactor. Therefore, the next generation of θ_{13} experiments prepared by the Daya-Bay [22], DoubleCHOOZ [23] and RENO [24] collaborations, consist of a near detector in a distance of about 100 m from the reactor and a far detector with a distance of 1 km. The near detector is located at a position rather close to the reactor. Since the distance is too small for neutrino oscillations to develop significantly, this allows to measure the reactor intensity. The far detector is then typically located where the first maximum of the oscillation is expected. This allows to cancel the dependence on the reactor neutrino flux by building the ratio between the respective rates. Nearly all these experiments are operational and aim to improve the sensitivity by about an order of magnitude. Encouraging indications for a non-zero θ_{13} exist: Combined analysis of results from several neutrino oscillation experiments tends to favor $\theta_{13} > 0$ with about 3 σ significance [6].

Evidence for neutrino oscillations has been found in long baseline experiments with artificial sources as well as with atmospheric and solar neutrinos. The results show neutrinos have a small, but non-zero rest mass. The mass m_3 is separated from the

[6] dependent on Δm_{23}

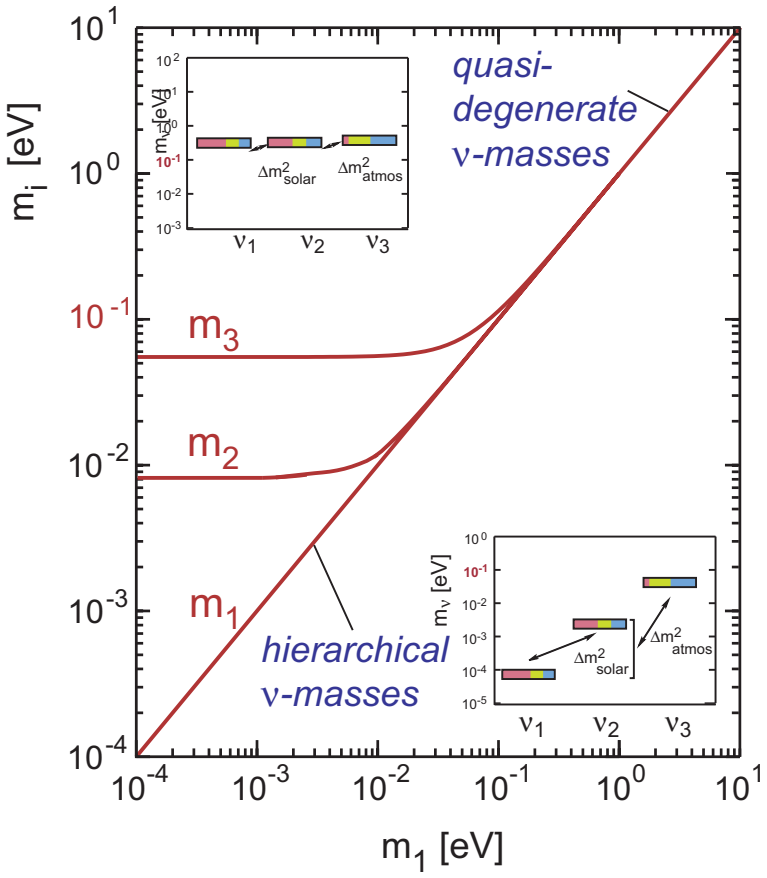

Figure 2.5: **Hierarchical and degenerate mass scale** [25]. In the degenerate case ($m \gg \Delta m$), the lightest neutrino has a mass larger than the mass differences, so that the mass scale for all neutrinos is given by this mass. In the hierarchical scenario ($m \lesssim \Delta m$), the mass of the lightest neutrino is small in comparison to the mass differences, so that the masses differ by orders of magnitude and the mass differences are relevant.

more closely spaced pair m_1 and m_2. However, the mass hierarchy is still unclear, as shown in Fig. 2.4. Both a normal $m_1 < m_2 < m_3$ or an inverted hierarchy $m_3 < m_1 < m_2$ is still allowed. Also, the absolute mass scale remains unknown, which is illustrated in Fig. 2.5.

In addition to the importance of neutrino masses in understanding the fundamental mechanisms which generate masses and govern the weak interaction, neutrino masses also play an important role in the history of the universe. The influence of neutrino masses on these cosmological questions will be discussed in the next section.

2.1.3 Neutrinos in Cosmology and Astroparticle Physics

Cosmology and astroparticle physics provide additional input for neutrino physics and vice versa. Neutrinos are a part of the dark matter density in the universe, although it is clear that light sub-eV neutrinos contribute sub-dominantly to the dark matter energy density. More importantly, cosmology is sensitive to the neutrino

mass scale. Observations of the anisotropies of the Cosmic Microwave Background (CMB) and large scale structure formation can be used to extract information about the neutrino mass scale. Future measurements of the cosmic neutrino background could then be used to gain knowledge about the very early universe.

Dark matter

Today, there is compelling albeit indirect observational evidence for dark matter, i.e. matter which only interacts gravitationally. Mostly, this evidence comes from the measurement of orbital velocities of bound objects. The analysis of the kinematics of these objects (galaxies, clusters) in the form of rotation curves or cluster temperature reveals significant amounts of non-visible matter [11].

Historically, the first evidence comes from the measurement of rotation curves from galaxies: Assuming that most of the matter of a galaxy is contained inside the visible part of a galaxy, one would expect outlying stars on a stable orbit with radius r around a galaxy with mass $M(r)$ inside the orbit of the star, to follow $M(r) \approx M_C = \text{constant}$ for sufficiently large radii r. The velocity profile should thus follow $v(r) \propto \sqrt{\frac{M_C}{r}}$. However, the observed velocity profiles of such stars behave for most galaxies more like $v(r) \propto \text{constant}$ which in turn implies $M(r) \propto r$. The amount of gravitational mass needed to maintain their respective orbit thus does not coincide with the amount of visible matter. However, the observations are consistent with a halo of dark matter surrounding galaxies and galaxy clusters.

Dark matter can be grouped in two categories, depending on whether it was relativistic at the beginning of structure formation (hot dark matter) or not (cold dark matter). While cold dark matter tends to cluster due to gravity and therefore speeds up the gravitational collapse leading to the creation of galaxies and stars, hot dark matter remains diffuse and slows down the structure formation process. Analysis of the CMB discussed below and structure formation (see Sec. 2.2.2) in the universe indicate that most of the dark matter must be cold. Candidates for cold dark matter include WIMPs (weakly interacting massive particles), in particular the lightest stable super-symmetric particle (LSP), primordial black holes and axions. The standard-model neutrinos are classified as hot dark matter due to their production at high temperatures and their small mass.

With the present precision of cosmological data, there is no evidence for a significant influence of hot dark matter on structure formation. However, simulations show that hot dark matter would leave a distinct signature on certain cosmological observables. This effect allows to derive upper limits on hot dark matter and thus the neutrino mass scale, which are of the order of 1 eV, but are model dependent. More details can be found in Sec. 2.2.2.

Cosmic microwave background

The cosmic microwave background radiation is a thermal radiation, which is almost isotropic and believed to fill the universe homogeneously. Its energy spectrum is well described by that of a black body with a temperature of $T = 2.725$ K.

Experimentally, the CMB was discovered accidentally in 1965 by Wilson and Penzias [26]. Today it is one of crucial experimental evidences for the Hot Big Bang

Theory and one of the important information sources about the early universe. The Hot Big Bang theory states that the universe originated in a very hot and dense initial state, from which it expanded and cooled to its present state. It predicts naturally the existence of the CMB: In this scenario, the CMB was generated about 380000 years after the Big Bang. In this period, the temperature of the universe was for the first time low enough that electrons and protons could combine and form stable hydrogen atoms. Thus the state of the universe changed from a proton - electron plasma, which was tightly coupled with photons and in thermal equilibrium, to become decoupled and transparent for photons. As soon as the photons decoupled from the baryons and electrons, they could freely propagate from this so-called 'surface of last scattering' towards us. Since the universe was in thermal equilibrium at that time, the CMB has a black body spectrum. Since the expansion of the universe conserves the shape of a black body spectrum, this is still the case today, however, this expansion has red-shifted the temperature of that black body to $T = 2.725$ K.

Similarly neutrinos decoupled from the rest of the universe and a cosmic neutrino background was created. The decoupling of neutrinos happened long before the creation of the CMB, about 1 s after the Big Bang. It is even stronger red-shifted to a temperature of 1.95 K. Due to this strong redshift, the energy of the neutrinos is too small to be detected with todays neutrino experiments.

The absorption of microwaves in the atmosphere prohibits precision measurements of the CMB on the surface of the earth. Such experiments are either mounted on balloons or satellite missions. After the first satellite mission dedicated to investigate the CMB, the COBE experiment [27], led to many interesting insights, a follow-up mission, the Wilkinson Microwave Anisotropy probe(WMAP) was launched in 2001. It has been taking data up until recently. The third generation mission PLANCK was launched in 2009 and has recently published first results [28].

The CMB data[27, 29] show an almost perfect black body spectrum with fluctuations, which are usually reported using a spherical harmonics expansion:

$$T_(\theta, \phi) = \sum_{lm} a_{lm} Y_{lm}(\theta, \phi) \tag{2.14}$$

The most prominent deviation from a black body is due to a dipole moment of 3.355 ± 0.008 mK. This is caused by the Doppler effect and simply a consequence of the movement of the earth relative to the SMB reference frame, where this dipole moment vanishes. This relative velocity is 369.0 ± 0.9 km s^{-1}. Correcting for the orbital velocity of the sun around the galactic center, this allows to derive the velocity of our local group of galaxies to $v_{LG} = 627 \pm 22$ kms^{-1}.

In addition to the dipole, fluctuations on the level of 10^{-5} are observed and shown in Fig. 2.6. These are understood as primordial density fluctuations reflected in the surface of last scattering. Fluctuations[7] for $l < 100$, corresponding to large angles, are caused by the different gravitational redshifts the CMB photons experience due to intrinsic density fluctuations at the surface of last scattering and afterwards, the so-called Sachs-Wolfe Effect. Of special interest is the intermediate region ($100 < l < 1000$), which reflects acoustic oscillations in the plasma. For very large l, fluctuations

[7] an angle θ corresponds roughly to $\theta \approx \frac{\pi}{l}$

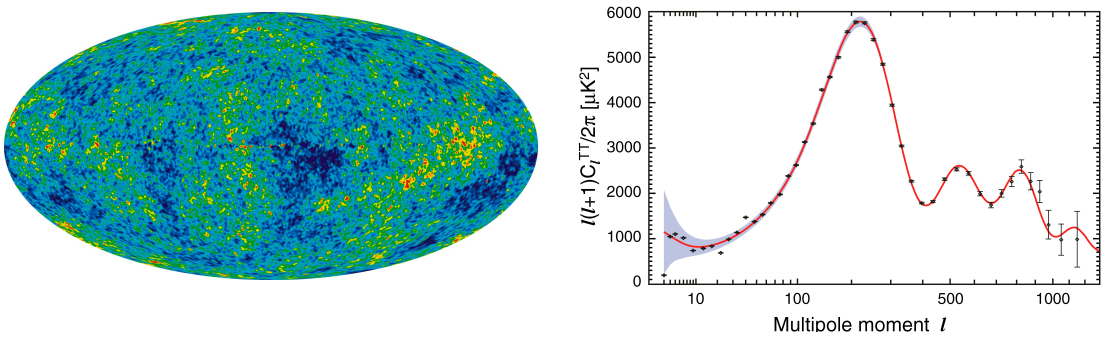

(a) sky map of the CMB (b) power spectrum of the CMB

Figure 2.6: **The cosmic microwave background** as measured by the WMAP mission: The left figure shows the sky map, with the galactic foreground and the dipole moment removed. Visible are fluctuations on the 10^{-5} level which are interpreted as primordial density fluctuations. From such a sky map, the power spectrum shown on the right can be extracted via a multi-pole expansion. The acoustic peaks, which are sensitive to certain parameters of the concordance model of cosmology are clearly visible. For example, the position of the first peak is sensitive to the intrinsic curvature of space-time.

of the CMB are damped out via diffusion processes between the plasma sector and the photons.

These fluctuations allow to gain knowledge about density fluctuations in the early universe and are sensitive to cosmological parameters of the so-called concordance model of Cosmology, which shall be discussed in the following.

Concordance model

The concordance model of Cosmology is based on the Cosmological Principle, which states that the universe is isotropic and homogeneous at large scales. With this assumption, the Einstein equation

$$R_{\mu\nu} - \frac{1}{2} g_{\mu\nu} R = 8\pi G T_{\mu\nu} + \Lambda g_{\mu\nu}, \tag{2.15}$$

which in general relativity relates the energy momentum tensor $T_{\mu\nu}$ to the metric $g_{\mu\nu}$ and curvature $R_{\mu\nu}$ of space time including a contribution from a cosmological constant Λ, leads to the Robertson-Walker metric

$$ds^2 = dt^2 - R(t)^2 \left[\frac{dr^2}{1 - kr^2} + r^2 \left(d\theta^2 + \sin^2 \theta d\phi^2 \right) \right]. \tag{2.16}$$

With the further assumption that the universe is a perfect fluid with pressure p and density ρ

$$T_{\mu\nu} = -p g_{\mu\nu} + (p + \rho)\delta_{00}, \tag{2.17}$$

the cosmological equations of motion (Friedmann - Lemaitre equations) follow as well [6]. From these, one can identify the following contributions to the total energy density Ω_{tot} of the universe

$$\Omega_{tot} - 1 = \Omega_\Lambda + \Omega_{CDM} + \Omega_{BM} + \Omega_\nu + \Omega_{rad} - 1 = \frac{k}{R^2 H^2} \tag{2.18}$$

Table 2.2: Contribution to the energy density of the universe [6]

Parameter	energy content due to	current value
Ω_Λ	Dark energy	0.728 ± 0.015
Ω_{CDM}	cold dark matter	0.227 ± 0.014
Ω_{BM}	baryonic matter	0.0456 ± 0.0016
Ω_ν	neutrinos	$0.001 < \Omega_\nu < 0.13$
Ω_{rad}	radiation	$5 \cdot 10^{-5}$
Ω_k	curvature of space-time	0 (between -0.77% and +0.31%)

However, while their values can be measured (see Tbl. 2.2 for recent results), very little is known about the constituents themselves:

- The nature of the largest contribution, the dark energy Ω_Λ is completely unclear. The most simple model is the presence of a cosmological constant Λ, but more advanced quintessence models have also been proposed.

- While several theoretical ideas for contributions to cold dark matter Ω_{CDM} like axions, WIMPs, right handed neutrinos, etc. have been proposed, none of them has been confirmed experimentally.

- Matter corresponds to the baryonic energy density Ω_{BM}, which contributes only to less than 5% to the total energy density.

- The radiation energy density Ω_{rad} is the only one where a direct model independent measurement can be performed - it is dominated by the CMB photons, therefore a measurement of the CMB temperature and intensity can be used to determine its value. Results from the FIRAS experiment performed as part of the COBE satellite mission lead to a very small contribution of about 10^{-5}.

- The contribution from the intrinsic curvature of space-time $\frac{k}{R^2H^2}$ can be derived from the CMB power spectrum, in particular via the position of the first acoustic peak. However it seems to be vanishing, corresponding to a flat universe.

- For the contribution of neutrinos to the energy density of the universe Ω_ν, a lower and upper bound can be derived. The available parameter space is shown in Fig. 2.7. Assuming degenerate neutrinos with $m_1 \approx m_2 \approx m_3 \approx 2$ eV, corresponding to the current upper limit from laboratory experiments, the upper bound is $\Omega_\nu < 0.13$. The lower bound of $\Omega_\nu \gtrsim 0.001$ can be derived from the mass differences determined with neutrino oscillations by setting $m_1 = 0, m_2 = \Delta M_{12}, M_3 = \Delta M_{13}$. The sensitivity of the KATRIN experiment of 200 meV would improve the upper limit by an order of magnitude. In case KATRIN only finds a new upper limit, the available parameter space would be reduced by a factor of two.

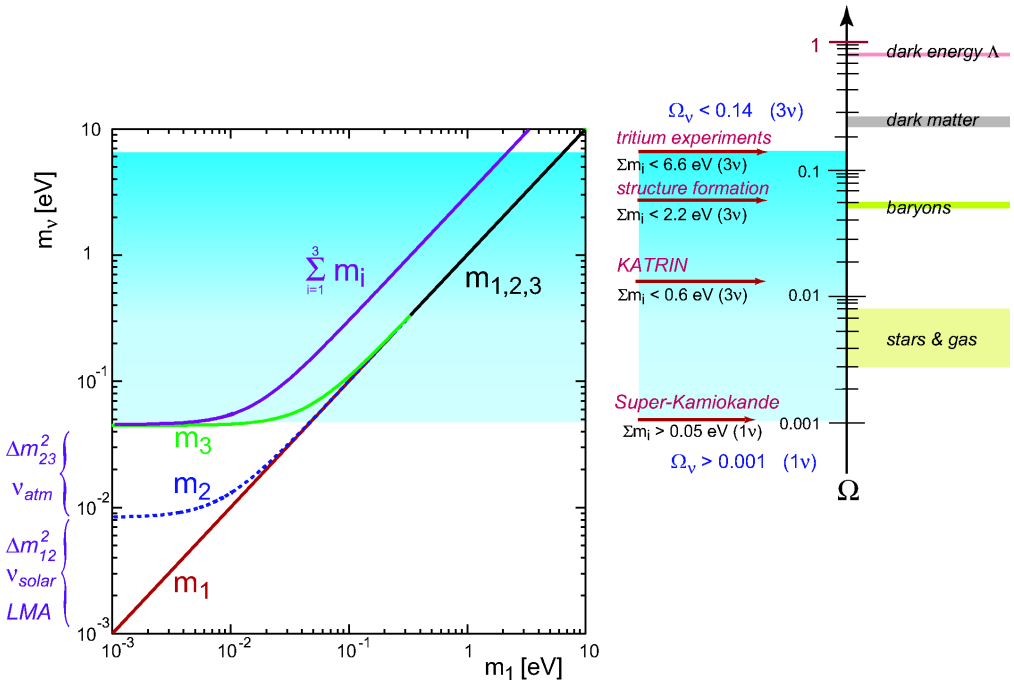

Figure 2.7: **Neutrino masses and their contributions to the energy of the universe** [**25**]. Dependent on the overall scale, neutrino masses can either follow a hierarchical or a degenerate pattern. The allowed range for the total energy density of neutrinos still covers two orders of magnitude. The lower bound comes from neutrino oscillations, several upper bounds obtained with different models are shown as well as the energy densities of baryonic and dark matter and dark energy.

2.2 Neutrino mass and its determination

After the overview over neutrino physics and the role of neutrinos in particle physics and cosmology, this section focuses on the role of neutrino mass in particle physics and cosmology. First, the most promising approach to incorporate neutrino masses in an extended standard model is discussed in Sec. 2.2.1. On the experimental side, there are several complementary approaches to determine the neutrino masses, which are discussed in the remaining part of this section: The first possibility, discussed in Sec. 2.2.2, is to look for the effect of neutrino masses in high precision cosmological data, in particular structure formation. Additionally, if neutrinoless double β-decay would be observed, it would lead to additional insights on neutrino masses and properties as discussed in Sec. 2.2.3. However, all of the above methods are strongly model dependent, therefore Sec. 2.2.4 discusses the extremely important model independent approaches, which use only relativistic kinematics to access m_ν.

2.2.1 The seesaw mechanism

While many extensions to the SM with the aim to accommodate neutrino masses are under theoretical investigation, the most promising one is the seesaw mechanism. Several variations of this mechanism exist: In the type I seesaw, which shall be discussed here, two or more right-handed neutrino and the presence of an additional high energy scale, e.g. the energy scale of a hypothetical Grand Unified Theory E_{GUT}, are needed in addition to the SM. A direct measurement of the neutrino mass in a range predicted by seesaw models could therefore be seen as an indirect hint for the existence of such a Grand Unified Theory (GUT).

The seesaw mechanism exploits the fact that a matrix of the form

$$\mathcal{M}_{ij} = \begin{pmatrix} 0 & m \\ m & M \end{pmatrix}. \tag{2.19}$$

has eigenvalues $\frac{M}{2} \pm \sqrt{\frac{M^2}{4} + m^2}$. For $m \ll M$, the eigenvalues are approximately $M, -\frac{m^2}{M}$.

If the mass M is the mass of the right-handed neutrino, the smaller eigenvalue $-\frac{m^2}{M}$ gives rise to a small neutrino mass for the left handed neutrinos. Identifying M with the GUT scale and m with the electroweak symmetry breaking scale leads to a neutrino mass scale below about 1 eV.

Such a mass matrix can be constructed for neutrinos, which shall be motivated in the following. In addition to the Dirac mass terms

$$\lambda^D_{ij}\overline{\nu^R_i} v \nu^L_j + h.c., \tag{2.20}$$

with the vacuum expectation value of the Higgs field v, one can also introduce Majorana mass terms for the right handed neutrino:

$$-\frac{1}{2} M^M_i \left(\overline{\nu^R_i}\nu^R_i + h.c.\right), \tag{2.21}$$

which leads to the mass matrix of type $\mathcal{M}$. In case $m^D_{ij} = \lambda^D_{ij} v \ll M$, the interplay between Majorana and Dirac terms generates an effective mass term for the left

handed neutrinos $m^D_{jk} \propto m^D_{ji} M_i^{-1} m^D_{ik} \ll 1$ as described above for the matrix $\mathcal{M}_{ij}$. The parameter m^D_{ij} is naturally of $\mathrm{O}(v) = 174$ GeV, the electroweak symmetry breaking scale, while M could arise during the breaking of a hypothetical high energy GUT theory and thus is believed to be of the order of 10^{16} GeV. The light neutrino masses are thus naturally small. Quantitative predictions for the neutrino mass depend on the details of the model, but generally the seesaw mechanism type I described here tends to favor very light and thus hierarchical neutrinos. However, introducing additional fields (seesaw type II, ...) allows for degenerate masses as well. Since the KATRIN experiment with a sensitivity of 200 meV can helpt to distinguish whether hierarchical, inverse hierarchical or degenerate neutrino masses are realized, it can therefore favor certain approaches and even rule out some specific models.

2.2.2 Neutrino masses from Cosmology

As outlined above, several cosmological observables are sensitive to neutrino masses. In first approximation, the observable is the sum over all mass eigenstates, $m_{cosmo} = \sum m_j$. For example, neutrino masses have a small influence on the CMB power spectrum. The effect is rather weak due to the high energies at decoupling and there is a degeneracy with other cosmological parameters, in particular in the dark energy sector. Usually, additional data sets are used to break this degeneracy. These include supernova redshift surveys and large scale structure surveys, which contain information about the later era of structure formation, where neutrino masses leave a distinct fingerprint.

Structure formation

Neutrinos play a crucial role in the formation of large scale structures in the universe. Since neutrinos are light and decouple from the rest of the SM particles at very high energies, they act as hot dark matter during the formation of large scale structures. Thus they leave a pronounced imprint on the large scale structures of the universe and can be distinguished from other dark matter candidates like the LSP, which contribute to cold dark matter. Fig. 2.8 shows results of structure formation simulations for different neutrino masses.

Galaxy surveys such as the Sloan Digital Sky Survey SDSS [31] provide maps of galaxies over a large distance range. Such sky maps are usually characterized with the help of correlations functions. Of particular importance is the two -point correlation function

$$< f(r_0) f(r_0 + r) >= f_{02}(1 + \xi(r)) \tag{2.22}$$

which describes the probability of finding another galaxy at a fixed distance r from a random galaxy. Nowadays, its Fourier transform, the power spectrum, is more widely used and shown in Fig. 2.9.

By comparing these observations with the results of structure formation simulations, the power spectrum is sensitive to the contributions of hot dark matter and thus indirectly neutrino mass. As of today, no evidence of a hot dark matter contribution has been observed, so only upper limits for neutrino masses can be derived. Similar to the CMB measurement, the limits obtained depend on the model and the parameter set in use and range from 0.2 to 1 eV. Therefore, an experiment like KATRIN

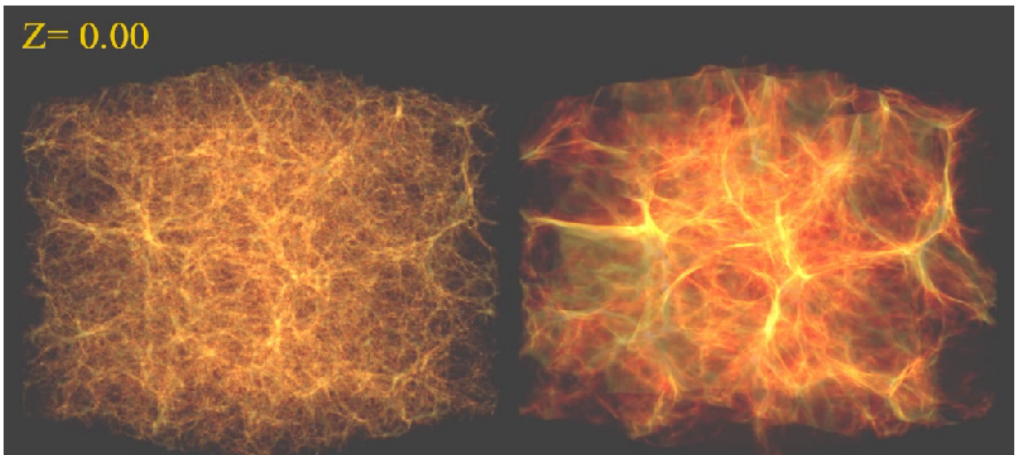

Figure 2.8: **Results of dark matter density simulations for different neutrino masses** [30]. The simulation on the left shows the present dark matter density for a vanishing neutrino mass, the simulation on the right includes a sum of neutrino masses of $M = 6.9$ eV, the upper limit from laboratory experiments. The free streaming of neutrinos smooths out density fluctuations on small scales. Thus it increases the voids between galaxies and makes the filaments more 'fluffy'. By comparing simulation results to observations of the large scale structure of the universe, which follows the dark matter distribution, one can derive limits on neutrino mass.

will provide important feedback to cosmology. The inclusion of Λ_ν as an additional free parameter in the fit leads to degeneracies with other cosmological parameters, so using prior knowledge to constrain neutrino masses would be extremely helpful.

2.2.3 Neutrinoless double β-decay

Double β-decay ($2\nu\beta\beta$ decay) refers to the simultaneous decay of two neutrons in one nucleus into two protons, electrons and neutrinos.

$$2n \longrightarrow 2p + 2e^- + 2\overline{\nu_e} \tag{2.23}$$

This is shown schematically in Fig. 2.10(a). Since this is a second order process of the weak interaction, the corresponding half lives are very long (typically about 10^{20} y). At present, $2\nu\beta\beta$ decay has been observed successfully for only 11 isotopes. In $2\nu\beta\beta$ decay, the electrons exhibit a continuous energy spectrum between $E_{min} = 2m_e$ and $E_{max} = M_i - M_f$, where $M_{i(f)}$ is the mass of the initial (final) nucleus. The two neutrino double-beta-decay obeys lepton number conservation and is a standard model process.

However, several extensions to the SM predict lepton number violation and consequently allow neutrinoless double-beta-decay($0\nu\beta\beta$ decay) - a process forbidden in the SM.

In particular, neutrinoless double β-decay $0\nu\beta\beta$ is possible if neutrinos are their own anti-particle, so called Majorana particles. In this case, one can connect the two outgoing lines of the Feynman diagram of Fig. 2.10(a) and arrives at Fig. 2.10(b).

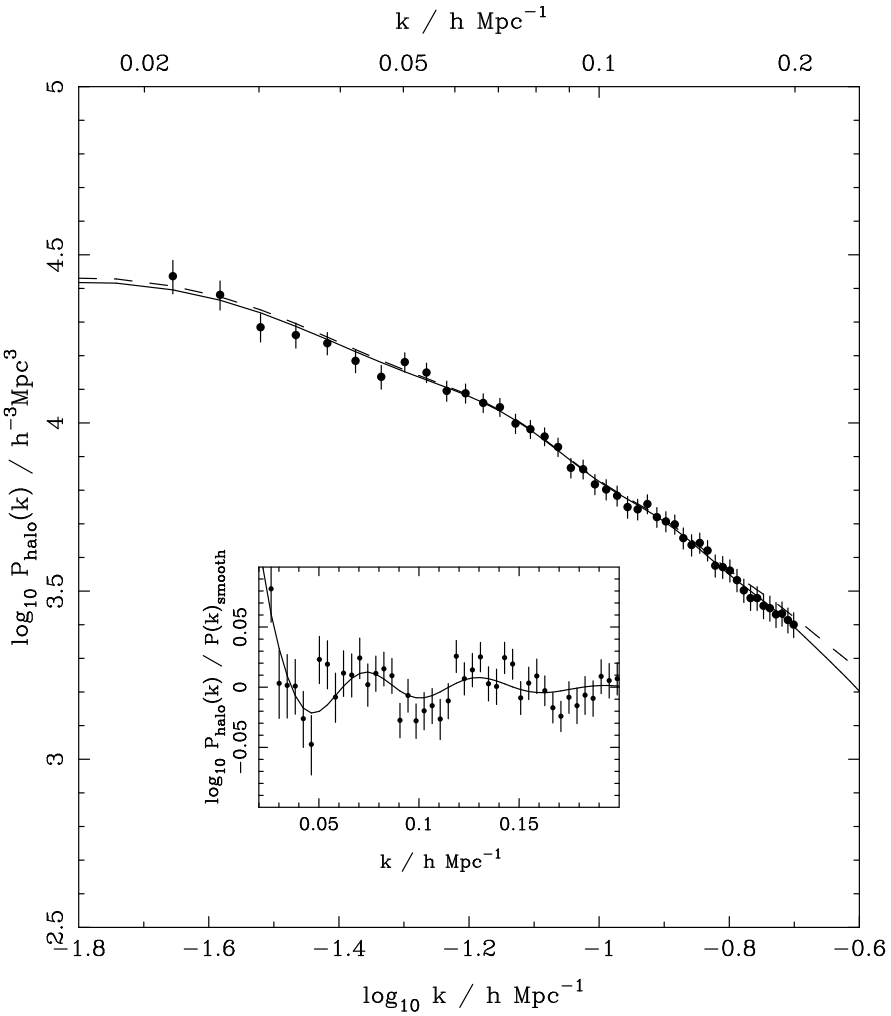

Figure 2.9: **The galaxy power spectrum** from the SDSS Luminous Red Galaxies [32]. The two lines correspond to a simultaneous fit of WMAP5 data and the SDSS LRG Survey to the Λ_{CDM} model with two different sets of nuisance parameters.

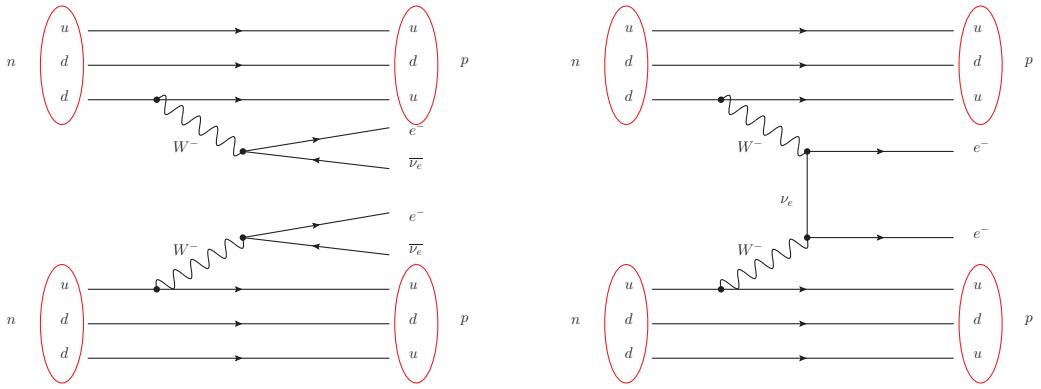

(a) $2\nu\beta\beta$ (b) $0\nu\beta\beta$

Figure 2.10: **Feynman diagrams** for $2\nu\beta\beta$ (2.10(a)) and $0\nu\beta\beta$ decay (2.10(b)). $2\nu\beta\beta$ can be seen as the simultaneous decay of two neutrons in the nucleus. If the neutrino is its own antiparticle, $0\nu\beta\beta$ via the exchange of a virtual neutrino is possible.

While the virtual anti-neutrino is produced right-handed, it is absorbed as right-handed neutrino. This helicity flip is only possible for massive particles and the probability for this helicity flip is proportional to the coherent sum over all neutrino masses

$$\langle m_{\beta\beta} \rangle^2 = \left| \sum_i U_{ei}^2 m_{\nu_i} \right|^2 . \tag{2.24}$$

Hence the half life $T_{1/2}^{0\nu}$ of $0\nu\beta\beta$ decay is sensitive to neutrino mass while the half life of $2\nu\beta\beta$ is not. In particular, $T_{1/2}^{0\nu}$ is given by:

$$T_{1/2}^{0\nu} = \left(G^{0\nu} \left| M^{0\nu} \right|^2 m_{\beta\beta}^2 \right)^{-1} \tag{2.25}$$

While the phase space factor $G^{0\nu}$ can be calculated reliably, the nuclear matrix element $|M^{0\nu}|$ requires complex and extensive nuclear structure calculations. For any given nuclei, the spread of the results found in the literature leads to a systematic uncertainty of $m_{\beta\beta}$ of a factor of $\approx$3. Furthermore, additional complications arise: $m_{\beta\beta}$ contains a coherent sum over the neutrino masses, so cancellations may occur due to the complex elements of the PMNS matrix (see Sec. 2.1.2). Additionally, other lepton number violating extensions of the standard model have been proposed, which also predict $0\nu\beta\beta$ decay, like lepton number violating right handed current interactions. This would make the interpretation of an observed $0\nu\beta\beta$ decay in terms of neutrino mass difficult. In an extreme case, the half life $T_{1/2}^{0\nu}$ could be non-zero, even if $m_{\beta\beta}$ vanishes due to fine-tuned values of the phases in the PMNS - matrix defined in Eq. (2.5).

The current best upper limit on $T_{1/2}^{0\nu}$ was published by the Heidelberg Moscow Collaboration, which has searched for $0\nu\beta\beta$ decay using 5 semiconductor calorimeters made out of the known $2\nu\beta\beta$ emitter ^{76}Ge. A part of the collaboration later claimed

evidence for an observation of $0\nu\beta\beta$ with 4.2σ [33, 34], based on a larger data sample and new analysis techniques.

$$T^{0\nu}_{1/2} = 2.23^{+0.44}_{-0.31}10^{25}y \qquad \text{corresponding to} \qquad m_{\beta\beta} = 0.32^{+0.03}_{-0.03}\ \text{eV}. \tag{2.26}$$

However this conclusion was disputed by the rest of the collaboration [35]. Despite a later increase of the significance to 6σ, the claimed observation failed to convince large parts of the community. This claim will be tested by several next generation experiments searching for $0\nu\beta\beta$, in particular the experiments GERDA [36], EXO [37] and Cuore [38].

2.2.4 Direct kinematic methods

All of the methods discussed so far strongly depend on precise modeling of the underlying physics. Therefore they should to be complemented by methods based only on well established first principles. The two methods discussed in this section, time-of-flight measurements of supernova neutrinos and the neutrino mass determination from β-decay allow the determination of the neutrino mass based solely on relativistic kinematics and the conservation of energy and momentum, although the first method, time of flight measurements of supernovae, requires a detailed understanding of the neutrino emission of a supernova.

Time of flight measurements of supernova neutrinos

During the lifetime of a star, gravitation and radiation pressure balance each other and stabilize the star. The radiation pressure is driven by energy creation via fusion of first hydrogen and, in later stages, of heavier elements. Since fusion stops to generate energy at an atomic number of ≈56, eventually an ^{56}Fe/^{56}Ni core will form. This core can be stabilized by the degeneracy pressure of the electrons via the Pauli principle. However, when the core reaches a critical mass, the Chandrasekhar mass of $M_{ch} \approx 1.4M_{\odot}$, this situation suddenly changes drastically - the core collapses to form a neutron star. During this neutronization and subsequent cooling

$$e^{-} + p \longrightarrow n + \nu_e \tag{2.27}$$

about 10^{58} neutrinos are created and leave the star [11], taking away about 99% of the energy freed by the above reaction. The collapse is eventually stopped by the strong interaction. After the implosion of the iron core, neutrino heating of the stalled shockwave in combination with instabilities from rotational and magnetic effects triggers the propagation of shockwave to outer shells. This manifests itself by an enormous increase in the brightness of the star, the actual supernova explosion. A supernova often outshines its entire host galaxy.

Of special interest here is the neutrino emission of a supernova. The neutrinos are emitted in a pulse of about 10 s length. At first, the core is opaque for neutrinos despite their low cross section due to its high density. This introduces significant uncertainties in the emission characteristics of supernova neutrinos and ultimately limits the sensitivity to the neutrino mass.

The neutrino mass m_ν can be derived from these supernova neutrinos, since it affects the time of flight of the neutrinos:

$$T_\nu = \frac{L_\nu}{\beta} = \frac{L_\nu}{\sqrt{(1 - \frac{m_\nu^2}{E_\nu^2})}} \approx L_\nu \left(\frac{m_\nu}{2E_\nu^2}\right) \qquad \text{for} \qquad \frac{m_\nu^2}{E_\nu^2} \ll 1 \tag{2.28}$$

which yields for the difference between the arrival times of two neutrinos with energies E_1 and E_2:

$$\Delta T = t_2 - t_1 = \Delta t_0 + \frac{L_\nu m_\nu^2}{2}\left(\frac{1}{E_2^2} - \frac{1}{E_1^2}\right) \tag{2.29}$$

The time Δt_0 denotes the time difference between the emission of the two neutrinos. Since Δt_0 cannot be measured, it needs to be estimated with models for the neutrino emission of the supernova. As mentioned ebove, the details of the emission are poorly understood and therefore, this introduces a significant uncertainty in the neutrino mass determination.

There was only one nearby supernova in recent times where the neutrinos could be detected - the supernova 1987A in the Large Magellanic cloud, located about 50 kpc from the earth. The experiments Kamiokande-II and IMB were able to measure the arrival time and energy for 11 and 8 neutrinos, respectively [39, 40]. From these, an upper limit of

$$m_\nu < 5.7 \text{ eV} \tag{2.30}$$

could be derived [41]. If a similar supernova would happen in the near future, the higher sensitivity of current neutrino experiments would detect between several hundred and several thousand neutrinos (Super-Kamiokande), which would allow to increase the sensitivity of this kind of measurement to about 1 eV. However, the results will become sensitive to the detailed modeling of the emission characteristics.

β-decay

The most promising independent way to measure neutrino masses with a laboratory experiment, is the single β-decay. The differential energy spectrum $\frac{\mathrm{d}N}{\mathrm{d}E}$ for the decay electrons can be expressed as

$$\frac{\mathrm{d}N}{\mathrm{d}E} = C{\cdot}F(Z,E){\cdot}K(p,E)\,(E_0 - E)\sqrt{\left((E_0 - E)^2 - m_{\overline{\nu_e}}^2\right)}\Theta\left(E_0 - E - m_{\overline{\nu_e}}\right) \tag{2.31}$$

$K(p,E) = p_e\,(E + m_e)\,(E_0 - E)$ denotes the part of the phase space which is independent of $m_{\overline{\nu_e}}$.

The constant C is given by

$$C = \frac{G_F^2 \cos\theta_C}{2\pi}\left(g_A^2 + g_V^2\right), \tag{2.32}$$

with the Fermi constant G_F, the Cabbibo angle θ_C and the axial and vector coupling strengths g_A and g_V. E_0 denotes the endpoint of the spectrum (the maximum possible energy of the electron for $m_{\overline{\nu_e}} = 0$). The Heaviside function $\Theta\left(E_0 - E - m_{\overline{\nu_e}}\right)$ ensures energy conservation.

The Fermi function $F(Z,E)$ takes into account the interaction of the outgoing β-electron with the daughter nucleus and is given by

$$F(Z,E) = \frac{x}{1 - \exp(-x)}\left(a_0 + a_1\beta\right), \qquad \text{with} \quad x = \frac{2\pi Z\alpha}{\beta} \tag{2.33}$$

α is the fine structure constant, $a_0 = 1.002037$ and $a_1 = -0.001427$ are phenomenological modifications to the non-relativistic Fermi function [42], so that it yields the

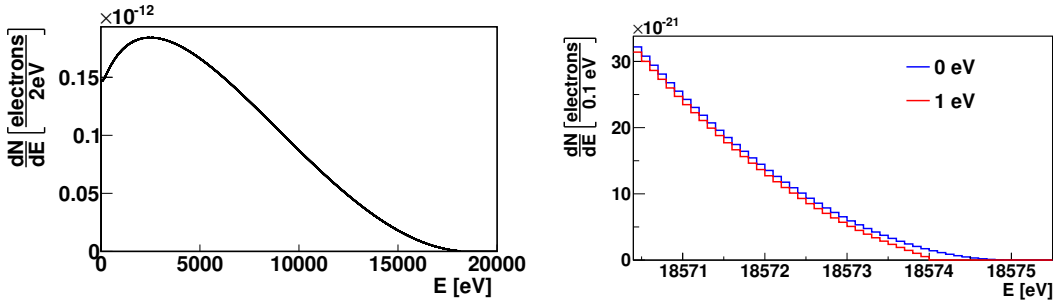

Figure 2.11: **Differential β-decay spectrum of tritium**. The left plot shows the entire differential spectrum. The zoom to the endpoint region illustrates the influence of a non zero neutrino mass near the endpoint. In comparison to the massless case both the endpoint position and the shape of the spectrum close to the endpoint are modified.

same result as the relativistic calculation [43]. In the region of interest for neutrino mass measurements near the endpoint, the Fermi function is approximately constant. In the last 50 eV, the Fermi function only varies by less than 0.03%.

The neutrino mass observed in single β-decay $m_{\overline{\nu}_e}$ is the incoherent sum over the three mass eigenstates

$$m^2_{\overline{\nu}_e} = \sum_j |U_{ej}|^2 \, m_j^2. \tag{2.34}$$

This use of an effective 'electron neutrino mass' $m_{\overline{\nu}_e}$ is valid, as long as the energy resolution of the experiment is significantly larger than the spacing of the mass eigenstates. For the energy resolution of the KATRIN experiment, this is the case for "standard model" neutrinos. However, some theories propose additional right handed sterile neutrinos, which could be of the order of the energy resolution of 1 eV. In this case, the differential spectrum becomes

$$\frac{\mathrm{d}N}{\mathrm{d}E} \propto (E_0 - E) \sqrt{\sum_j |U_{ej}|^2 \sum (E_0 - E)^2 - m_j^2}. \tag{2.35}$$

As can be seen from both Fig. 2.11 and Eq. (2.31), a non-vanishing neutrino mass $m_{\overline{\nu}_e}$ has two consequences:

- The effective endpoint of the spectrum is shifted by $m_{\overline{\nu}_e}$ due to the presence of the Heaviside function $\Theta\left(E_0 - E - m_{\overline{\nu}_e}\right)$
- The spectral shape is modified due to $\sqrt{\left((E_0 - E)^2 - m^2_{\overline{\nu}_e}\right)}$. This is most pronounced for high electron energies $E \approx E_0$, where the first term is small[8]. This can be understood intuitively: Only close to the endpoint is the mass of the neutrino of the same order of magnitude as its (unmeasured) momentum and therefore its influence on the spectrum can be identified only in this extremely narrow region.

[8] note that $\sqrt{\left((E_0 - E)^2 - m^2_{\overline{\nu}_e}\right)}$ is always real if $\Theta\left(E_0 - E - m_{\overline{\nu}_e}\right) = 1$

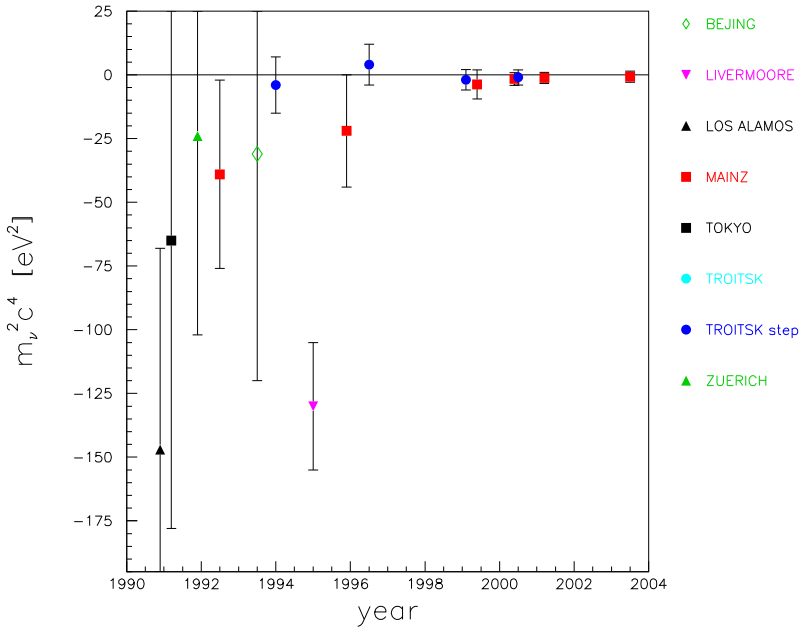

Figure 2.12: **Results from β-decay [25] neutrino mass experiments**. In all cases, tritium was used as source material.

In principle, a measurement of the endpoint and the precise knowledge of the decay energy, the so-called Q-value would be sufficient to determine the neutrino mass. However, the endpoint is always hidden by intrinsic experimental background and the Q-value is not known with sufficient precision. Therefore β-decay experiments use the spectral shape to determine the neutrino mass. This is experimentally challenging, because tiny modifications of the electron energy due experimental influences on the spectrum like inelastic scattering inside the source material have to be avoided whenever possible or carefully controlled otherwise. The latter is also true for contributions of more refined theoretic treatments like excited states of the daughter nucleus.

Out of the large number of possible β emitters, two are especially favorable for neutrino mass measurements, namely the hydrogen isotope Tritium ^{3}H = T and the Rhenium isotope ^{187}Re.

Tritium β-decay

For more than 60 years by now, tritium β-decay experiments have been performed to determine the neutrino mass. As can be seen in Fig. 2.12, despite their increasing precision the results remain compatible with zero. Since the first measurements [44, 45], the experiments followed a common setup: Tritium decays inside a source, the decay electrons are guided along magnetic field lines through an energy filter (spectrometer) and finally counted with a detector. Early experiments typically used solid or embedded tritium sources, the LANL experiment employed for the first time a gaseous tritium source [46] like KATRIN.

There is a multitude of reasons, why tritium is by far the most popular choice for neutrino mass measurements:

- Tritium is a hydrogen isotope, therefore many electromagnetic and chemical properties can be derived from the theoretically well understood and experimentally extensively tested hydrogen, taking into account the higher mass. In particular, the Fermi function is well known. The same is true for the daughter nucleus, the ^{3}He ion.
- Tritium has the second lowest endpoint energy E_0, so a relatively large fraction of all electrons are in the region of interest near E_0, which is proportional to $\frac{1}{E_0^3}$.
- The half life of tritium is only 12.3 y, since the decay is super-allowed. Therefore a comparatively small amount of tritium is sufficient for a competitive measurement. This also reduces energy losses due to inelastic scattering in the source itself.
- Energy losses in the source are further reduced, since the inelastic scattering cross section for T_2 is small (Z=2).
- The decay is super-allowed, hence no energy dependent corrections are needed for the nuclear matrix element.
- The excitations of the daughter nucleus can be calculated reliably as well.

The two immediate predecessors of the KATRIN experiment, the Mainz and Troitsk experiments also used tritium as electron source. Both experiments employed the same method for the energy analysis, an electromagnetic spectrometer based on the principle of magnetic adiabatic collimation in combination with an electrostatic filter (MAC-E Filter) [47]. Since this approach will also be realized in the KATRIN experiment, it is explained in more detail in Sec. 3.1. The most significant difference between the Mainz and Troitsk experiments was the source: The Mainz experiment featured a solid state source while Troitsk employed a gaseous Tritium source. Both experiments achieved similar sensitivity and today provide the best limits obtained by lab experiments. The final result obtained by the Mainz experiment is

$$\begin{aligned} \left(m_{\overline{\nu}}^{\beta}\right)^2 &= (-0.6 \pm 2.2 \pm 2.1)\ \text{eV})^2 \\ m_{\overline{\nu}}^{\beta} &< 2.3\ \text{eV} \qquad (\ 95\%\ \text{C.L}) \end{aligned} \tag{2.36}$$

The results of the Troitsk experiment are more difficult to interpret due to the presence of an additional line in the spectrum close to the endpoint which so far the Troitsk collaboration cannot fully explain. Including additional parameters to describe this line in the analysis leads to [48]

$$\begin{aligned} \left(m_{\overline{\nu}}^{\beta}\right)^2 &= (-2.3 \pm 2.5 \pm 2.0)\ \text{eV}^2, \\ m_{\overline{\nu}}^{\beta} &< 2.05\ \text{eV} \qquad (95\%\ \text{C.L}). \end{aligned} \tag{2.37}$$

Rhenium β-decay

While almost all previous neutrino mass experiments have been based on tritium, a bolometric measurement which measures the temperature rise due to a single

β-decay making use of ^{187}Re also seems. It has the lowest endpoint of all known β-emitters with a Q-value of only 2.47 keV. However, the half life of Rhenium is $4.32 \cdot 10^{10}$y, which implies that a large amount of Rhenium is needed to perform a sensitive measurement. The best upper limits from Rhenium experiments are still an order of magnitude less stringent than the Tritium limits: The MANU experiment in Genova was able to achieve an upper limit of 19 eV, simultaneously the MIBETA experiment in Mailand arrived at a limit of $m_{\overline{\nu_e}} < 15$ eV. Although this is still an order of magnitude away from the Mainz/Troitsk limit, the big advantage of this approach is that it can be easily scaled - the detector can in principle be enlarged simply by adding more microcalorimeters. This fact triggered the construction of the MARE experiment, which aims in its first phase to arrive at a sensitivity compatible to the Mainz and Troitsk experiments, while simultaneously improving the understanding of the systematics involved in the bolometric approach. In a second phase, MARE-II will then be sensitive to the same neutrino mass range as KATRIN and thus would provide a complementary measurement of $m_{\overline{\nu_e}}$ with different systematics.

3. KATRIN

Since both the Mainz and Troitsk experiments discussed in the previous chapter have reached their systematic limits, a next generation neutrino mass experiment is needed to further improve the upper limit on the neutrino mass. This next generation experiment is the KATRIN experiment [25] shown in Fig. 3.1. KATRIN uses the same principle as the Mainz and Troitsk experiments, the MAC-E filter introduced in Sec. 3.1. Of major interest for this thesis is the tritium source described in detail in Sec. 3.2, followed by a brief overview of the other components: the transport section in Sec. 3.3, the tandem spectrometer section in Sec. 3.4 and the detector in Sec. 3.5. This section concludes with the tasks of the control and monitoring section in Sec. 3.6.

The aim of the KATRIN experiment is to improve the experimental sensitivity (90% C.L.) on the neutrino mass to 200 meV, corresponding to an improvement by an order of magnitude in comparison with the results obtained by Mainz and Troitsk. This implies that precision and accuracy for the experimental observable $m^2_{\overline{\nu}_e}$ (cf. Eq. (2.31)) have to improve by a factor of 100. This in turn leads to the following basic requirements for the KATRIN setup:

- A factor 100 larger sample of β-electrons is required in comparison to the Mainz and Troitsk experiments, therefore the source strength must be increased by a factor of about 100.
- Correspondingly, the systematic errors need to be reduced by more than one order of magnitude.
- The energy resolution of the spectrometer should be about 1 eV which is a factor $3 - 4$ better than Mainz and Troitsk.
- The background rate should not exceed 10 mHz.

The KATRIN experiment is under construction at the Campus North of the Karlsruhe Institute of Technology (KIT). The location was chosen as the Tritium Laboratory Karlsruhe located there has both the certification and the necessary institutional experience in handling the huge amounts of tritium necessary to operate the KATRIN tritium source.

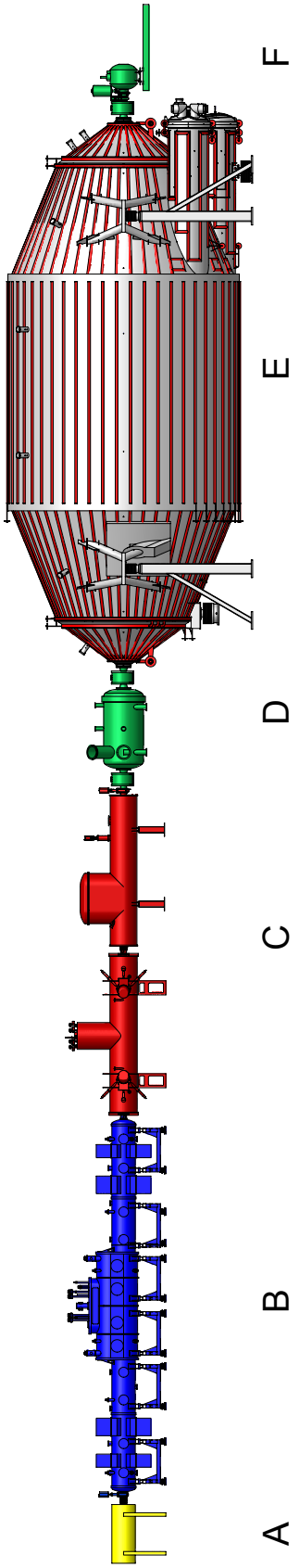

Figure 3.1: **Schematic view of the KATRIN experiment**. The 70 m long experimental setup consists of the calibration and monitoring system CMS (A), the tritium source (B), the transport section (C), the pre-spectrometer (D), the main spectrometer (E) and the detector (F).

3.1 MAC-E Filter

The KATRIN experiment makes use of the principle of Magnetic Adiabatic Collimation with an Electrostatic Filter (MAC-E Filter), originally proposed in [47] and successfully employed in the Mainz and Troitsk experiments. As schematically shown in Fig. 3.2, a MAC-E Filter consists of two guiding magnets in combination with an retarding electric field. The electrons created in the source propagate towards the detector on a cyclotron motion due to the magnetic guidance field. Since the magnetic field $\vec{B}$ in the analysis plane is several orders of magnitude smaller than the magnetic field in the entry region, the magnetic gradient force $\vec{F_\nabla} = \vec{\nabla}\left(\vec{\mu}\cdot\vec{B}\right)$ converts energy stored in cyclotron motion, $E_\perp$, into longitudinal energy $E_\parallel$. For this conversion to work, the magnetic field $\vec{B}$ needs to vary slowly enough, so that the magnetic moment $\vec{\mu}$ given by

$$\mu = \frac{E_\perp}{B} \tag{3.1}$$

remains constant[1]. Only if the longitudinal energy is sufficiently large to overcome the retarding potential, an electron can eventually reach the detector. A MAC-E filter thus acts as an high pass filter. The energy resolution of such a MAC-E filter can be obtained with Eq. (3.1) − it is associated with the maximal possible energy ΔE which remains in the cyclotron motion after the adiabatic collimation and therefore cannot be analyzed with the retarding potential. This immediately leads to

$$\frac{\Delta E}{E} = \frac{B_A}{B_{max}}. \tag{3.2}$$

The maximal magnetic field B_{max} is not in the source itself, but somewhere between source and spectrometer. With such a configuration, one can make use of the magnetic mirror effect to remove electrons with a large starting angle. These have a longer path length in the source and thus suffer from a higher probability to loose energy by inelastic scattering.. The maximal accepted starting angle in such a setup is given by

$$\sin\theta_{max} = \sqrt{\frac{B_S}{B_{max}}} \tag{3.3}$$

An important quantity of a MAC-E filter is the transmission function. It gives the probability for a particle with charge q and kinetic energy E to be transmitted through an MAC-E filter set on retarding potential qU, energy resolution ΔE and magnetic fields B_S and B_A as defined in Fig.3.2. While it needs to be experimentally verified for a real experimental setup, for an ideal MAC-E filter and an isotropic source, the transmission function $T(E, qU)$ is given by [25]:

$$T(E,qU) = \begin{cases} 0 & E - qU < 0 \\ \dfrac{1-\sqrt{1-\frac{E-qU}{E}\frac{B_S}{B_A}}}{1-\sqrt{1-\frac{\Delta E}{E}\frac{B_S}{B_A}}} & 0 \le E - qU \le \Delta E \\ 1 & E - qU > \Delta E \end{cases} \tag{3.4}$$

[1]For relativistic particles $(1+\gamma)\cdot\frac{E_\perp}{B}$ is the adiabatic invariant of the electron motion. Due to the low endpoint of tritium, the maximum γ value is $\gamma_{\max} \approx 1.0006$, so the non relativistic approximation can be used.

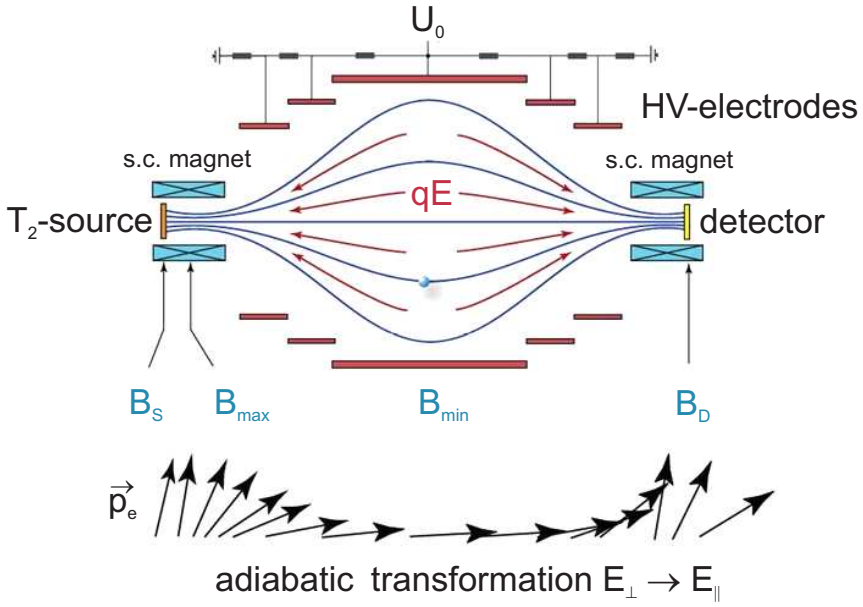

Figure 3.2: **Schematic view of a MAC-E Filter**. Electrons from the tritium source are guided along magnetic field lines towards the detector. On their way to the analysis plane in the middle of the spectrometer, most of their transversal momentum is converted to longitudinal momentum via adiabatic collimation: The magnetic field in the analysis plane is several orders of magnitude smaller than in the entry region. This leads to an adiabatic transformation of the energy stored in the cyclotron motion into longitudinal energy and thus to a parallelization of the electron momentum as shown schematically in the lower part of this figure. Only electrons with an longitudinal momentum large enough to overcome the retarding voltage U_0 can pass the analysis plane and reach the detector.

The transmission function features the typical characteristics of a high pass filter as shown in Fig. 3.3.

Additionally, the energy loss E_{loss} of the electrons between the source and the detector needs to be known. Since the electron is transported adiabatically through vacuum for the most part of its trajectory, energy losses are predominantly localized in the source. The only exception is synchrotron radiation, which is most pronounced in the region with strongest magnetic fields. Therefore energy losses depend strongly on the type of source used and the source itself. Experience from the Mainz experiment led to the conclusion that large systematic errors due to surface effects are unavoidable for solid state sources,. For this reason , the KATRIN experiment uses a windowless gaseous tritium source. In such a source the energy loss is mostly due to inelastic scattering with the gaseous tritium molecules. The energy loss is usually characterized with the so-called energy loss function $E_{loss}(E, \epsilon)$, which parametrizes the probability for an electron with energy E, to loose the energy ϵ in the source. The energy loss function of the KATRIN experiment will be discussed in detail in Sec. 5.1.2. It can be measured with the same experimental setup by means of an additional electron gun located at the rear end of the source.

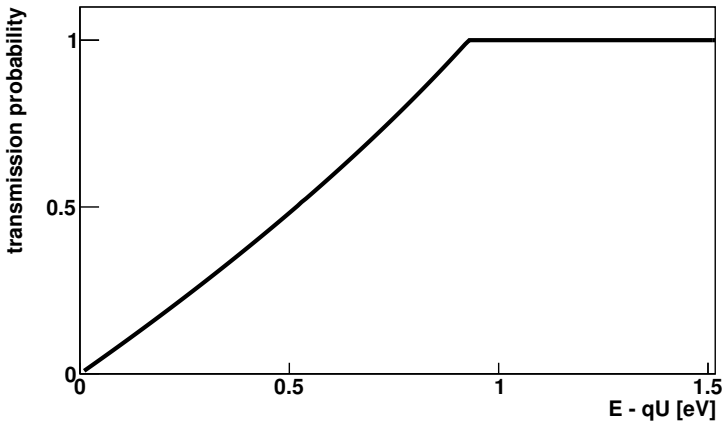

Figure 3.3: **Transmission function of a MAC-E filter**. A MAC-E filter acts as high pass filter, transmission is only possible if the electrons have sufficient energy to overcome the retarding potential. If this is fulfilled, there is an intermediate region, where the transmission probability increases until full transmission is reached. The width of the intermediate range is determined by the energy resolution ΔE and therefore by the ratio of the magnetic field in the analysis plane to the maximal magnetic field along the trajectory.

The convolution of $E_{loss}(\epsilon)$ with the transmission function defined in Eq. (3.4) defines the experimental response function R:

$$R(E, qU) = \int_0^{E/2} T(E - \epsilon, qU) E_{loss}(\epsilon) d\epsilon \tag{3.5}$$

The response function completely encompasses the properties of the experimental setup up to the detector. It is the probability for an electron emitted with energy E to be transmitted through the complete setup and reach the detector. Together with the differential spectrum defined in Eq. (2.31), the measured quantity of a MAC-E filter is therefore an integrated spectrum:

$$N(qU, E_0, m^2_{\overline{\nu}_e}) \propto \int_0^{E_0} \frac{\mathrm{d}N}{\mathrm{d}E}(E, E_0, m^2_{\overline{\nu}_e}) R(E, qU) dE. \tag{3.6}$$

3.2 The windowless gaseous tritium source

The source of the KATRIN experiment has to provide the tritium β-decay electrons with a high count rate in combination with small systematic errors. Experience from past tritium experiments has shown that this is best achieved with a windowless gaseous tritium source (WGTS). The WGTS of the KATRIN experiment is schematically shown in Fig. 3.4. It is operated at a base temperature of about 30 K. This operating temperature was chosen, since tritium begins to form clusters at temperatures below 25 K. Since the differential spectrum of such a cluster is different from that of tritium molecules due to different excitations of the respective remnant, this would lead to systematic errors in the neutrino mass determination.

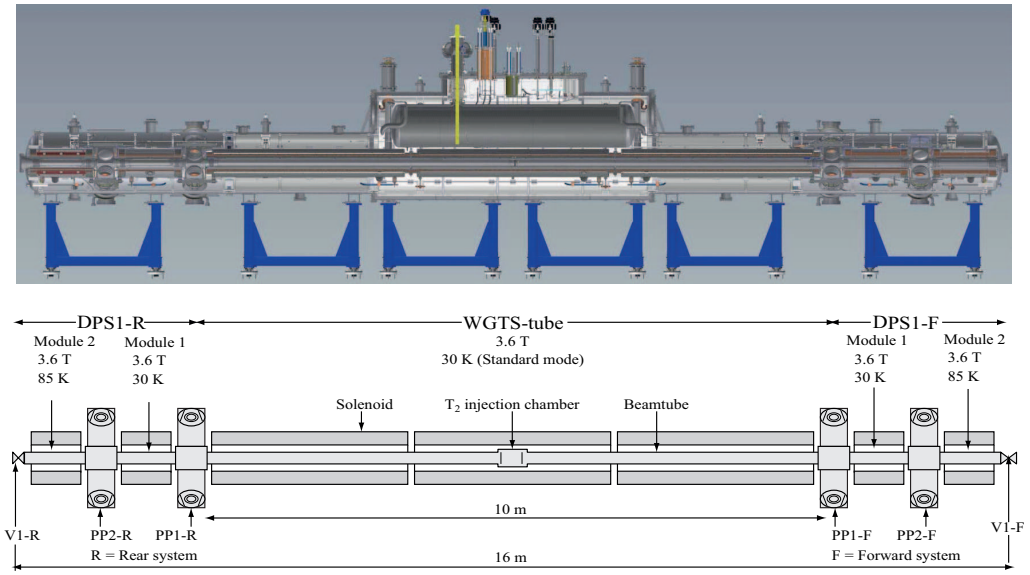

Figure 3.4: **Schematic view of the WGTS**. The WGTS cryostat consists of three major parts: the differential pumping section DPS1-R, the 10 m long inner WGTS beam tube and another differential pumping section, the DPS1-F (from left to right). Tritium is injected in the middle of the inner beam tube with an injection rate of about 1.8 mbar l/s ($p_{in} = 3.4{\cdot}10^{-3}$ mbar) via a specially designed injection chamber. It consists of 5 rings with altogether 415 holes with a diameter of 2 mm each. This is necessary to avoid turbulences in the injection region. The tritium streams from the injection towards both ends where it is pumped with the differential pumping sections. The DPS1-R connects via the rear wall to the control and monitoring section, while the DPS1-F connects to another pumping section, the DPS2-F.

On the other hand, the tritium gas should be rather cold to reduce systematic effects due to Doppler broadening of the electron energies.

The WGTS provides about $10^{11}\,\frac{\text{electrons}}{s}$. A homogeneous magnetic field of 3.6 T is used to guide these β-decay electrons to both ends of the WGTS. This rate and consequently the column density

$$\rho d = \int \rho(z)\mathrm{d}z \tag{3.7}$$

has to be stable within 0.1% to avoid unacceptably large systematic errors. This implies a similar stability requirements for basic experimental parameters like inlet rate, temperature and gas composition. These challenges make the WGTS one of the most complex magnetic cryostats ever built.

Of particular importance is the stability of the injection pressure, which has to be stable within 10^{-3}. This is ensured by a pressure controlled buffer vessel in the inner tritium loop mentioned below. This inner loop system itself is operational and test measurements [49] with a WGTS dummy have reached a stability of 10^{-4}, which more than fulfills the requirements for KATRIN.

The other most important experimental parameter is the beam tube temperature, which also has to be stable within 1‰. To overcome this tremendous technical challenge, a novel two-phase cooling system was designed. This cooling system has been tested using original components with the so-called WGTS demonstrator. Again, the KATRIN requirements for the stability are more than fulfilled, with a stability of 10^{-4} over a time period of 5 h [50]. However, the temperature profile along the tube turned out to be inhomogeneous. While several design changes are being investigated to remedy this, the impact of this unexpected fact on the KATRIN sensitivity has been investigated as part of this thesis and will be discussed in Sec. 6.2.3.

The continuous supply with high purity (>95%) tritium is realized with a closed tritium loop system. The inner loop retrieves the tritium pumped by the first pumping sections, removes impurities with a permeator which is only permeable for hydrogen isotopes and collects the tritium in a storage vessel. This storage vessel is connected to the TLK purification system CAPER [51], which constantly cleans a fraction of this tritium. Furthermore, it used to supply the WGTS via a pressure controlled buffer vessel. Additionally, a Laser Raman spectroscopy unit is used as a continuously operating high precision monitor of the tritium purity [52]. An outer tritium loop collects the tritium retrieved from the transport section DPS2-F and is directly connected to CAPER.

3.2.1 The beam tube cooling system

In order to reach a stable column density, the beam tube temperature is stabilized with a novel two phase cooling system which is shown in Fig. 3.5. In the standard operating mode, the WGTS beam tube will be cooled with two two-phase tubes filled with boiling Ne attached on both sides on the beam tube. The two phase system can be operated with either Neon or Argon as cryogenic agent. For the standard operating temperature of 30 K Ne will be used. For certain calibration measurements with Krypton, the WGTS needs to be operated at a temperature of

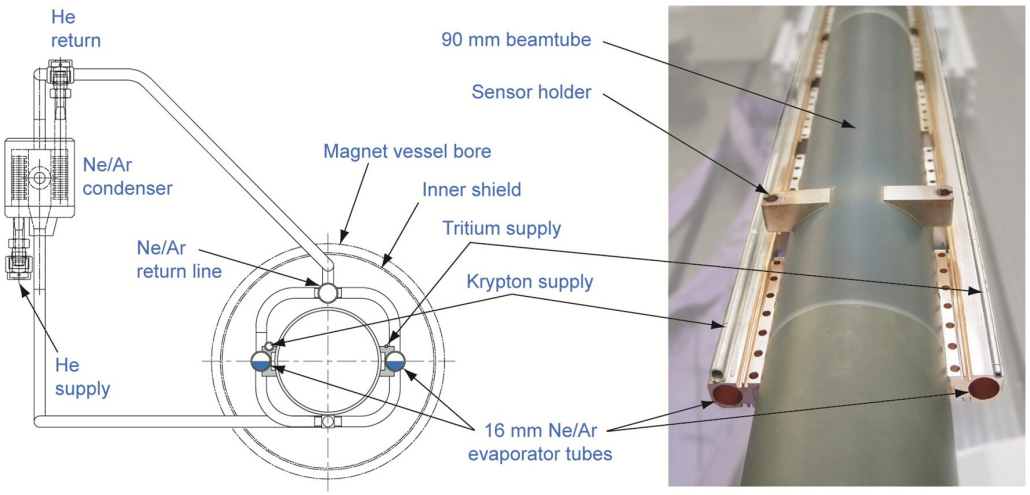

Figure 3.5: **Beam tube cooling circuit and tritium injection**. The WGTS beam tube will be cooled with two two-phase tubes filled with a boiling liquid, either Neon or Argon. From the two phase tubes, the gas phase is transported to a condenser via the Ne(Ar) return line and liquefied there. The condenser is specifically designed to shield the Ne/Ar circuit from temperature fluctuations of the Helium circuit. To achieve this, the condenser contains a lead core, which provides a large heat capacity. The condensed Ne(Ar) is then used to resupply the liquid phase of the two phase tube. In order to keep the two phase system boiling, heaters are active in the tubes. The whole beam tube is surrounded by the inner radiation shield, which protects it thermally from the much colder surrounding magnet system operated with a temperature of 4.5 K. Also shown are the Tritium and the Krypton supply tubes. Both are in thermal contact with one of the two phase tubes, so that the gas is already in thermal equilibrium when injected. Several mounting points for temperature sensors are also visible.

120 K, since Krypton freezes at lower temperatures. In this case, Argon will be used instead as cryogenic agent. The respective cryogenic agents were chosen, because their boiling points at $T \approx 30$ K(120 K) occur at pressures in the order of 1 bar, which can be easily handled.

The beam tube temperature is monitored with the help of several temperature sensors, which measure the temperature at different longitudinal and azimuthal positions as shown in Fig. 3.6:

- 24 pairs of PT500 temperature sensors[2] and vapor pressure sensors are distributed along the beam tube.
- Additionally, the vapor pressure in the cooling circuit can be measured directly and converted in a temperature with the help of the saturation pressure curve.

[2]A PT500 is a resistance thermometer, measuring temperature by monitoring the (temperature dependent) electric resistance of platinum

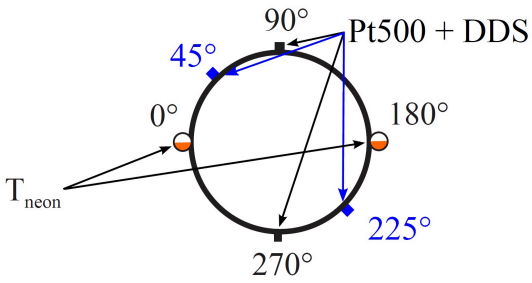

Figure 3.6: **Radial positions of the temperature sensors**. The vapor pressure in the two two phase tubes can be converted to a temperature. PT500 sensors at 10 different longitudinal positions allow to determine the temperature at the top and bottom of the beam tube. Four additional PT500 sensors are located at 45° and 225° close to the pump ports. The PT500 sensors operate continuously, however they have to be calibrated in situ, since they are strongly influenced by magnetic fields. Therefore each of these PT500 sensors is paired with a vapor pressure sensor (DDS), which can be used for calibration, as the vapor pressure sensors are not in continuous operation.

Since the beam tube itself is shielded from its surroundings by an inner radiation shield, there are in principle only two heat sources which could cause temperature fluctuations and inhomogeneities and therefore unstable column densities:

- radiation from the inner radiation shield: The inner radiation shield is on almost the same temperature as the beam tube, although at a less stringent stability level and thus can be neglected at first order.
- heat transfer via the pump ports. Despite the fact that the pump ports are also shielded from the surrounding temperature regimes, their corresponding heat input via radiation is unavoidable and significant.

Fig. 3.7 shows the expected temperature profile along the beam tube. However, due to the complex pump port geometry, a quantitative prediction of the temperature profile and stability based on simulations is impossible. Therefore, a test experiment, the WGTS demonstrator, discussed in the next section, is currently ongoing.

3.2.2 The WGTS demonstrator test setup

In order to test the performance of the cooling system, a test experiment, the so called WGTS demonstrator, is currently performed at TLK. This test is crucial to show that the stringent stability requirements for temperature stability of the WGTS can be fulfilled. Therefore, the demonstrator uses original components from the WGTS with a few exceptions:

- The magnets are not needed for the cryogenic tests, therefore they are replaced with a dummy cold mass in the demonstrator setup. This cold mass consists of hollow aluminum cylinders, located at the same position as the magnet coils to simulate the thermal influence of the 4.5 K cold magnets.

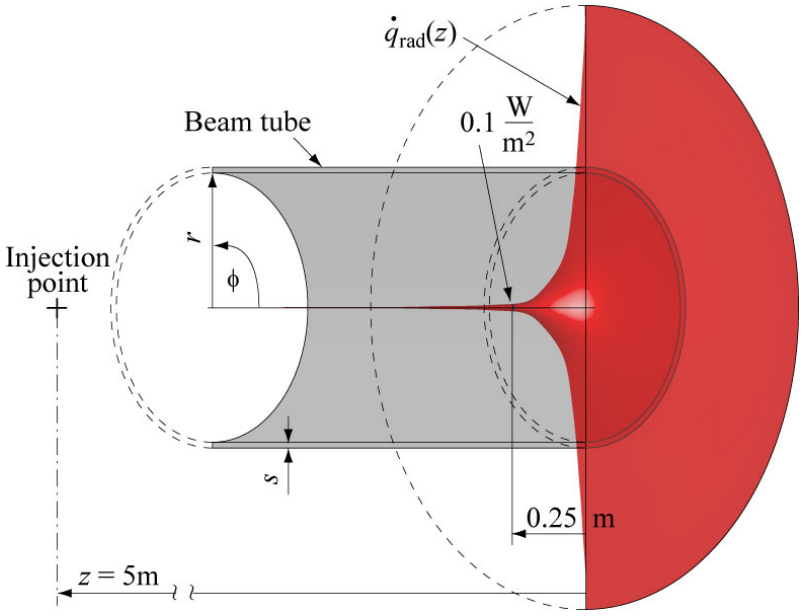

Figure 3.7: **Simulated heat load on a part of the WGTS beam tube**. The radiation from the pump ports causes a temperature rise close to the beam tube end. [53]

- Correspondingly, the center section (the turret and main central lid), which contains the cryogenic supply lines for the superconducting magnets is missing as well.
- The demonstrator has only one pumping chamber at each end while the WGTS will have two.

The above changes reduce the length of the setup from 16 m down to 12 m, while the radial layout remains the same, with the exception of the replacement of the magnets with the dummy cold mass.

3.3 The transport section

Adjacent of the WGTS, the two-component transport section is located. It consists of a differential pumping section (DPS2-F) shown in Fig. 3.8, followed by a cryogenic pumping section (CPS). The main tasks for the pumping sections are:

- Preventing tritium from the source from entering the spectrometer section. A reduction of the tritium flow by 12 orders of magnitude is necessary[3].
- Guiding the electrons along magnetic field lines from the source to the spectrometer with the help of guiding magnets.
- Preventing ions from the WGTS to reach the spectrometers, while additionally monitoring the ion flow. The ions are removed from the flux tube using electric

[3]not including a previous reduction by two orders of magnitude by the DPS1-F

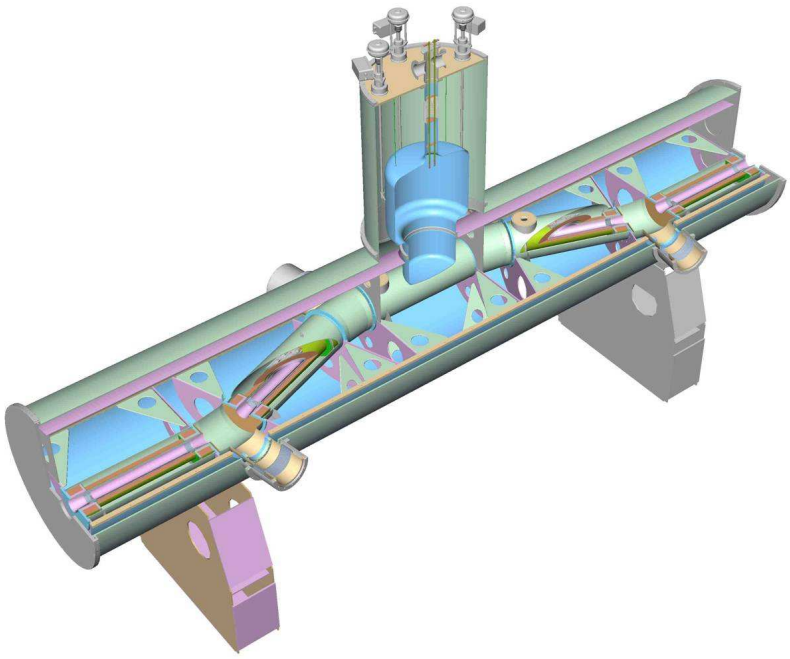

Figure 3.8: **Isometric view of differential pumping section DPS2-F**. The two bends ensure that there is no direct line of sight between the WGTS and the KATRIN main detector. This ensures that tritium molecules hit the wall at least once, which increases the pumping efficiency. The same principle is used in the beam line of the CPS.

dipoles located in the DPS2-F. Additionally, two FT-ICR[4] mass spectrometers are located in the beginning and the end of the DPS2-F.

- Monitoring the WGTS with the help of a forward beam monitor detector in the CPS. This detector is movable and can scan the complete flux tube. During normal data taking, it is located at the outer rim of the flux tube.

The injection rate of about 1.8 mbar l/s is already reduced by the DPS1-F by a factor of 10^2. The DPS2-F also uses turbo molecular pumps (TMPs) to reduce the tritium flow by an additional factor of 10^5. Since TMPs are unable to reduce the tritium flow further down to the allowed flow in the pre-spectrometer of 10^{-14} mbar l/s, the technique of gas adsorption has to be used for the remaining reduction factor of 10^7. This is realized in the cryogenic pumping section, which uses argon snow to capture the remaining tritium. In order to prevent molecules from traveling directly from the source to the detector both the DPS2-F and the CPS each have two bends. These chicanes ensure that the gas molecules hit the beam tube wall of the DPS2-F and CPS at least once, while the signal electrons are guided through these bends by the guiding magnets.

3.4 Spectrometers

The next component which the electrons have to pass to reach the detector is the two stage spectrometer section. The task of the spectrometers is to perform the

[4]Fourier transform ion cyclotron resonance

actual energy analysis. This is achieved with the MAC-E filter principle described in Sec. 3.1, so the spectrometers act as high pass filters. The spectrometers are operated under ultra high vacuum conditions (UHV) with $p < 10^{-11}$ mbar to minimize energy losses due to interactions of the β-electrons with the rest gas molecules. The 3.38 m long pre-spectrometer performs a pre-selection of the signal electrons, whereby these electrons have to pass a retarding potential of 18300 V, slightly below the tritium endpoint. This reduces the electron flow from about 10^{11} s^{-1} down to 10^4 s^{-1} and therefore further reduces background caused by the interaction of signal electrons with the rest gas in the main spectrometer. The precise energy selection is then performed by the 24 m long main spectrometer, which is typically on high voltage just a few Volts below the tritium endpoint (relative to the tritium source). By varying this high voltage difference, an integrated spectrum as given in Eq.(3.6) is measured.

The pre-spectrometer was the first KATRIN component to arrive at KIT and served as an important test setup for the larger main spectrometer. Since 2006, the main spectrometer is also on site. Currently, a wire electrode system is being installed inside the main spectrometer. These wire electrodes will be put on a slightly more negative potential than the main spectrometer vessel itself. This shields the inner part of the tank from electrons which are emitted from the inner surface of the main spectrometer vessel due to interactions by cosmic muons. In order to compensate the earth magnetic field and to fine tune the magnetic guiding field, an air-coil system has been installed surrounding the main spectrometer vessel.

3.5 Detector

Electrons which pass the analyzing plane are accelerated back to their original energy and finally reach the detector. While in principle a simple electron counter which determines the number of electrons having passed the spectrometer section would suffice, the actual focal plane detector features both a good energy and spacial resolution. This is necessary to fully monitor and understand the complex KATRIN setup and the different sources of background. For example, background from radioactive decays or cosmic rays can be discriminated using the energy information, and the spatial resolution is essential to account for spatial inhomogeneities of magnetic fields and electric potentials. The detector consists of a monolithic Si PIN diode array, segmented in 148 pixels as shown in Fig. 3.9. These pixels provide the spatial resolution. The energy resolution of each pixel is about 1 keV.

The detector has to be able to process rates between a few mHz close to the tritium endpoint up to 1 MHz during calibration measurements, with an intrinsic background below 1 mHz and a detection efficiency >90%. The detector is located in its own UHV module, which can be separated from the main spectrometer with a valve for maintenance purposes. To suppress background, the detector is surrounded by lead and copper shields and an active muon veto. As a further option, a ”post acceleration” of up to 30 keV can be applied to electrons coming from the spectrometer. This allows to shift the region of interest to an energy interval with lower natural background, devoid of fluorescence lines.

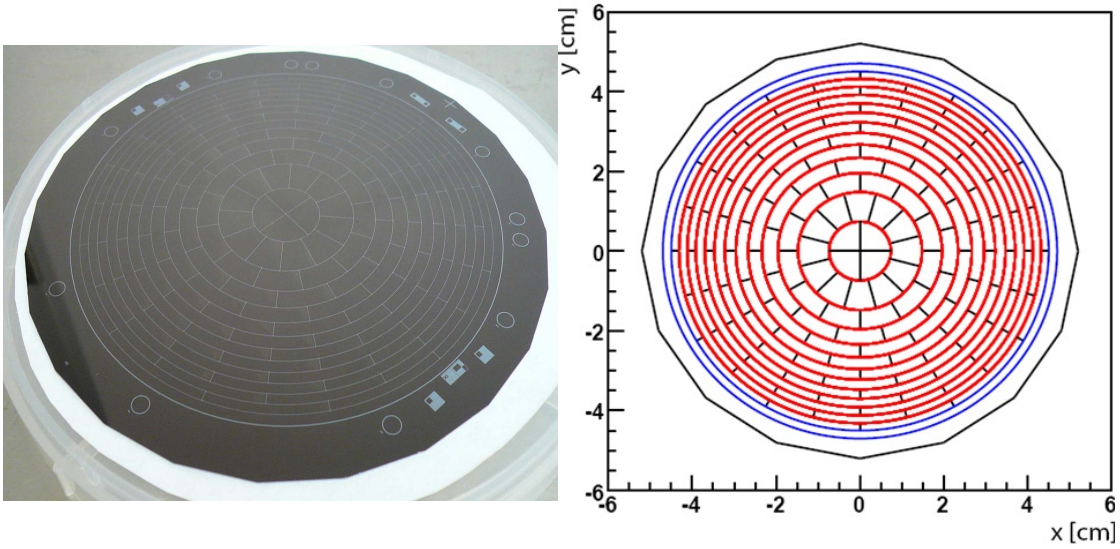

Figure 3.9: **Silicon wafer of the KATRIN main detector**. The detector consists of 148 pixels to provide a good spatial resolution. The pattern shows the layout of these pixels more clearly: All pixels are identical in area and therefore should see an equal amount of β-electrons.

3.6 The calibration and monitoring system

In the rear part of the WGTS, the calibration and monitoring system (CMS) depicted schematically in Fig. 3.10 contains dedicated calibration and monitoring devices: The so-called rear plate located at the end of the WGTS defines the WGTS potential. The actual column density can be continuously monitored with an X-ray detector in the rear section. Additionally, an angular resolved mono energetic electron gun can be used to measure important WGTS properties, in particular the column density and possible plasma effects as well as the transmission function of the main spectrometer. A conceptual design of the rear section exists [54] and the technical design is currently being worked out.

In addition to monitoring devices like the CMS, a complex experimental setup like the KATRIN experiment requires a detailed simulation software to predict and understand its properties. This software, which will be discussed in the following chapter 4, has for example to be able to compute the trajectories along the more than 70 m long KATRIN setup fast and accurately both to optimize the electromagnetic design and to understand complex background processes. Due to the high activity of the source, this approach is of limited use in the source and transport section. Here, another approach, the ability to compute the β-spectrum using a detailed experimental model to investigate systematic effects is mandatory.

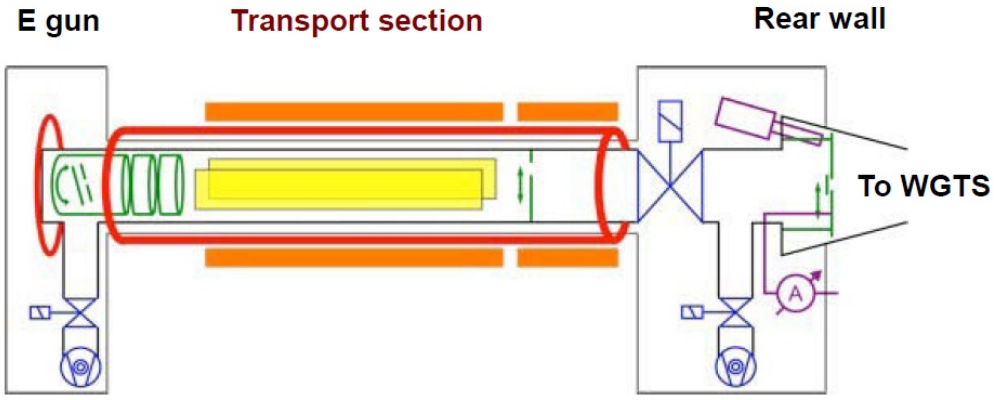

Figure 3.10: **Conceptual design of the CMS** [54]. The Control and monitoring system consists of an electron gun for calibration measurements. These electrons are guided via the transport section through a hole in the rear wall into the WGTS. The rear wall defines the WGTS potential and serves as monitoring device. It also allows to measure the bremsstrahlung emitted by the β decay electrons as they hit the rear plate.

4. The Kassiopeia Framework

In order to fully understand a complex setup like the KATRIN experiment, a dedicated simulation and analysis framework is mandatory. Such a framework needs to provide easy to use software tools to enhance the understanding of the experiment. For the KATRIN experiment, this primary simulation and analysis framework is called Kassiopeia. It has been developed specifically for KATRIN and can be used to investigate design questions and to prepare and fully understand test, calibration and finally neutrino mass measurements. It also includes a tool to estimate systematic uncertainties and the overall significance of the KATRIN experiment. Kassiopeia is written in C++ and combines both existing and newly developed tools in a common unified framework. These tools are organized into different categories, called modules. The central framework of Kassiopeia, called Core, has been written mostly by N. Oblath[1], D. Furse[1] [55], S. Mertens[2] [56] and myself, in large parts during a three month exchange visit at MIT of both S. Mertens and myself. This chapter gives an overview of Kassiopeia[3] as a whole, based mostly on its manual [57]. It is followed by a more detailed description of the components relevant to this thesis in the next chapter. Kassiopeia is divided into several major parts shown in Fig. 4.1: The simulation backbone (the core) provides the management structure of the simulation and is discussed in Sec. 4.1. The remaining part of this chapter, Sec. 4.2, is dedicated to a brief overview over different physics modules residing in Kassiopeia. A significant part of this thesis was dedicated to the development of some of these modules. These are discussed in more detail in chapter 5.

4.1 Kassiopeia Core

In addition to the code which simulates the underlying physics of KATRIN, a program of such a large scope such as Kassiopeia needs a lot of additional functionality, independent of the physics itself. This common functionality includes for example a common initialization and management structure, I/O operations and mathematical

[1] Massachusetts Institute of Technology in Cambridge, MA

[2] KIT

[3] as of version 1.5

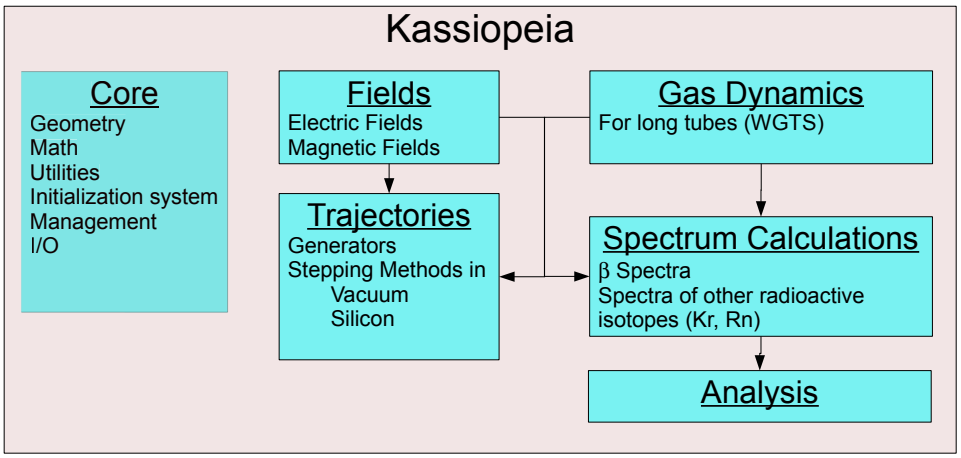

Figure 4.1: **Functional overview over Kassiopeia**. The Core contains the part of the simulation which does not deal with the simulation of physics processes. The different physics processes can be grouped in the following categories. The arrows indicate the logical dependencies between the modules, for example the trajectory calculation needs to know the electromagnetic fields in order to propagate charged particles and the density in order to calculate the likelihood for scattering. In fact, the Core already provides all the necessary interfaces between modules, so that every module only depends on the Core.

routines like numerical integration, random number generation and so on. In Kassiopeia, all this functionality is provided by the Kassiopeia Core. In addition, the Core provides the simulation's geometry. The mathematical component contains for example various solvers for differential equations, routines for numerical integration, an interface to a random number generator and a set of physical and numerical constants to ensure that they are used consistently throughout the simulation.

Since the physics modules can be applied to a large variety of different questions, ranging from the computation of electromagnetic fields over the simulation of particle trajectories to analysis methods, Kassiopeia is distributed with a series of executables which enable the user to perform the most common tasks. Each of the provided applications has an execution manager associated with it (a so-called `CoreManager`). This allows them to follow a common setup. The source code of all Kassiopeia executable therefore looks alike and provides a brief high-level overview over an arbitrary Kassiopeia executable, depicted schematically in Fig. 4.2.

4.1.1 Initialization

Kassiopeia is controlled with a set of configuration files with optional additional command line arguments. This is true for all applications, which use the Kassiopeia management structure, although not all applications need all configuration files. Default versions of these files are installed within Kassiopeias `etc/` directory. Each configuration file is responsible to configure one aspect of the application:

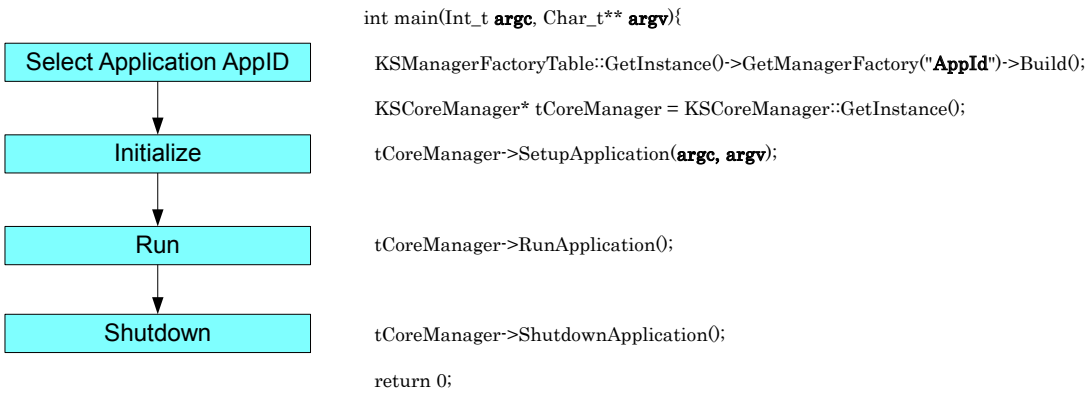

Figure 4.2: **Schematic layout of an Kassiopeia executable**. The first line of the program specifies the task Kassiopeia has to fulfill with the aid of the argument `AppId`. The second line simply defines a shortcut for the pointer to the top level manager of the simulation. Then, any executable has three stages: initialization, execution and shutdown. The initialization is performed by calling the method `SetupApplication(Int_t argc, Char_t** argv)` of the `KSCoreManager`. As discussed in more detail in Sec. 4.1.1, this method triggers the setup of the management structure and the processing of the simulation configuration provided by the user. The function governing the execution phase is the method `RunApplication()`. This is explained in more detail in the next section, Sec. 4.1.2 for the most important examples, the trajectory calculation (called `Kassiopeia`, like the package itself) and the sensitivity investigation tool (`KSCFitter`). `ShutdownApplication()` simply causes the executable to clean up after itself. This is only a technical detail and will not be discussed further.

- The User Configuration (default name: `UserConfiguration.txt`) contains mostly technical details, for example the verbosity level of the program, which governs the amount of information written to the screen (or more precisely, `stdout` and `stderr`) when Kassiopeia is executed.

- Geometric information relevant for the simulation is contained in another file, its default name is `GeometryConfiguration.txt`.

- Different electric and magnetic field calculation methods can be used throughout the simulation. These are specified in `FieldConfiguration.txt`

- The configuration of the spectrum calculation software described in detail in the next chapter is contained in `SSCConfiguration.txt`

- Event Generators are configured in `GeneratorConfiguration.txt`

- Methods for trajectory calculations in particular step size controls, solving methods and exit conditions are provided in a file with the default name `StepStrategyConfiguration.txt`

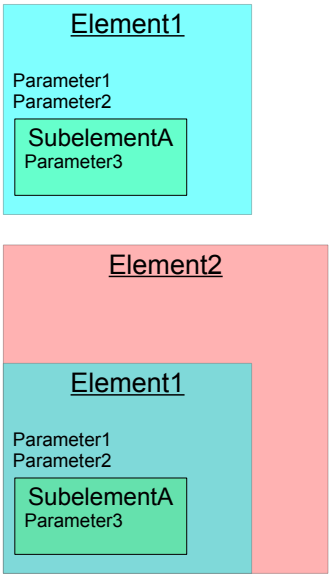


```
# this is a comment
<Element1> # the Kassiopeia type being configured
  <<Name=Element1Instance>> # most objects need a name
  # so that they can be referred to later
  <<Parameter1=Value1>> # Parameter1 of element 1 is set to
Value1
  <<Parameter2=Value2>> # and another one set to Value2
  <SubElementA> # a nested subelement
    <<Parameter3=Value3>>
  </SubElementA>
</Element1> # the end of the element

# alternatively, a nested structure can be specified
# by refering to the name of the nested object:
<Element2>
 <<Name=Element2Instance>>
 # this class needs an instance of element 1 to perform its task.
 # the name tells it which one to use, since there could be more
than one
 <<Element1=Element1Instance>>
</Element2>
```

Figure 4.3: **Kassiopeia configuration file syntax**. As in XML, single angle brackets `<ELEMENT> ...</ELEMENT>` are used to refer to objects. In contrast to XML, where attributes are listed within the simple brackets themselves, here double angle-brackets are used for parameter settings. Since in general, Kassiopeia class instances are named, relationships between classes can be specified by referring to their instance name. Several example configuration files can be found in Appendix A.2.

Moreover, there is typically one additional configuration file which is specific to the application in use. For the trajectory calculation, this is called by default `KassiopeiaConfiguration.txt`. Its main task is the combination of geometrical information with the different solution strategies defined in the other configuration files to so-called regions. For the sensitivity executable `KSCFitter`, the file `FitConfiguration.txt` contains the relevant additional instructions like which minimizing strategy to use.

The syntax of these configuration files is either standard XML [58] or a modified more human readable XML-like syntax shown in Fig. 4.3.

Of special interest is the possibility to set any instruction for Kassiopeia from the command line by inserting placeholders in the configuration file:

```
....
#<<Seed=12345>>
<<Seed=${RANDOMSEED}
<<Outputlevel=${LEVEL}
....
<<filename=results-seed-${RANDOMSEED}-level-${LEVEL}.root>>
```

In this case, the value of `Seed` can be set from the command line with `./Kassiopeia -r RANDOMSEED=12345`. Is is also possible to specify a default value for each replace-

ment in the UserConfiguration file. One can even combine replacements as shown above.

Internally, the instructions are processed following the builder pattern[4]. The instructions in a configuration file are processed by the `KSTokenizer`, who searches for a builder for the respective class and tells it to perform the appropriate configuration actions. Each fully configured instance of any Kassiopeia class is stored in a toolbox class[5] until it is needed. After the module configuration files have been read, these toolboxes contain all the classes which can be used during the program execution, but the relationship of these classes to each other is not necessarily specified at that point. The toolbox is only filled with tools during the processing of the module configuration files and the instruction, how these tools should be used, are contained in the additional executable specific configuration file. For example, for a trajectory simulation through the main spectrometer, using two different step size controls A and B in the upper and lower half of the spectrometer, both step size controls would be defined in the trajectory calculation methods configuration file. However, the instruction 'use A in the upper half and B in the lower half', which associates geometric information with trajectory calculation strategies, is specific to the trajectory executable and consequently contained in that executables configuration file.

4.1.2 Execution

The initialization infrastructure described above is common to all standard executables. Firstly, the simulation tools have to be defined and in the second step, information on how to use these tools has to be provided. If this has been performed successfully, the program enters its execution stage. By way of example, only the two most important applications are discussed here.

Particle Trajectory calculation

The trajectory calculation uses all the available modules in Kassiopeia. It is organized into four hierarchical levels. This hierarchy is also reflected throughout the code and in the output of the trajectory simulation:

- Runs: This is the highest level of organization and corresponds to one execution of Kassiopeia. Simulated experimental parameters are generally not allowed to be changed during one run[6]. A run serves mainly as container for the collection of events, the next lower level of organization.
- Event: The event level represents a physical process which generates one or more primary particles, and everything that happens as a consequence, e.g. secondary particles. On the event level, the event generator is called to create the initial state of the event and then asks the track manager to compute the tracks for one particle after another. Secondary particles can be added during the computation as well. The event level output contains a very brief summary

[4] `http://en.wikipedia.org/wiki/Builder_pattern`

[5] Toolboxes are a special type of managers, which store configured Kassiopeia objects. There are five toolboxes in Kassiopeia, corresponding to the five main configuration files apart from the user configuration.

[6] although they may be intrinsically time dependent

of the event, listing the number of particles in the event, timing information and an identification number.

- Track: The track level represents the information of one particle. Here, one particle moves step by step through the setup. After each step, a navigational check ensures that the stepping strategy and the step size control are still valid for the new position and performs the necessary reconfiguration if a new region is entered. This is done until an exit condition has been reached, which terminates the track computation. A high level summary for each track can be written to the output, which contains integral information like the track length and time of flight as well as an identification number and a reference to the parent particle if applicable.

- Step: A Step is the finest level of detail in Kassiopeia. It consists of an incremental discrete change to a particle state and typically consists of two phases: the solution of the equation of motion and the simulation of additional physical processes, in particular scattering and synchrotron radiation. Adding step level to the output file is possible, one can even customize the step level output. However, the files immediately grow very large if every step is written to the output, therefore it is also possible and more common to write only specific steps, e.g. when scattering occurred.

During the execution, the management structure traverses this structure recursively, until all events are processed. This is shown and explained in more detail in Fig. 4.4.

Sensitivity analysis

In this case, not all of the modules in Kassiopeia are used. Apart from the user configuration, only the field and spectrum calculation configuration files and modules are needed. Additional routines described in detail in Sec. 5.4 are used to simulate a KATRIN measurement. Statistical errors of this measurement are assigned based on a measuring scheme, consisting of a set of measurement points (voltages) and the time spent at that voltage. The ”measured” values are smeared accordingly to take into account statistical fluctuations. This simulated measurement therefore consists of an ntuple of high voltages and corresponding count rates, which can then be minimized with predefined fit functions. These fit functions also use the spectrum calculation module and either ROOTs Minuit implementation TMinuit [59] or routines from the GSL [60] as minimizer. As will be discussed in more detail in Sec. 5.4, statistical errors on the neutrino mass are determined by the repetition rate of fit results. As usual for Kassiopeia, the results are stored in a ROOT file.

4.2 The Kassiopeia modules

Kassiopeia has to be able to simulate the wide range of physics phenomena relevant to KATRIN, ranging from processes described by atomic and nuclear physics over electromagnetic properties to gas dynamical simulations. In Kassiopeia, these issues are organized in different categories, called modules. This section gives a brief overview over all the modules, the next chapter contains a more detailed description of several modules developed as part of this thesis.

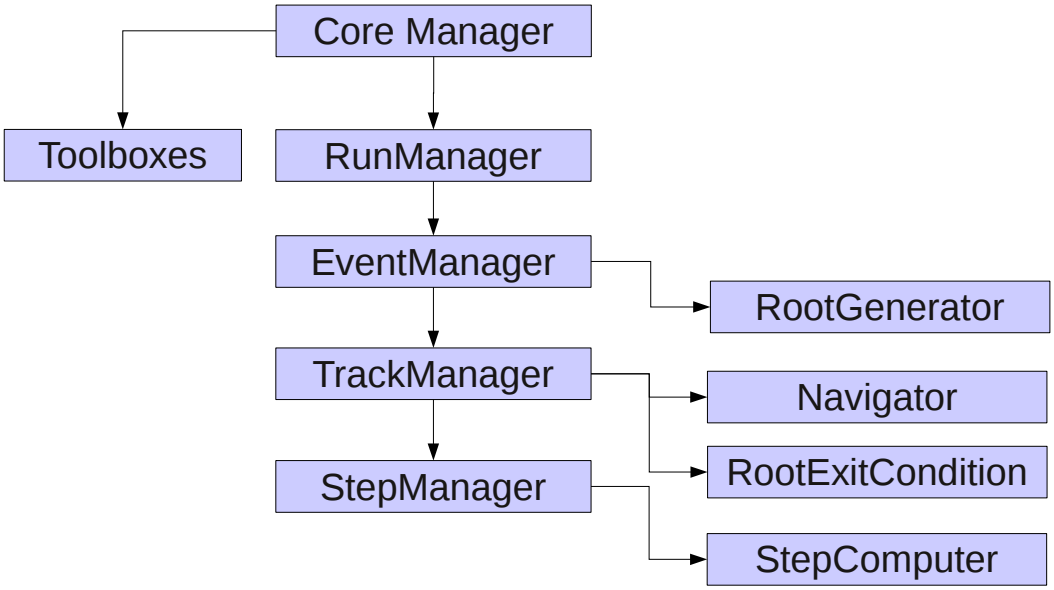

Figure 4.4: **Schematic of Kassiopeias execution phase**. The program traverses recursively through the event, track and step level. On the event level, the root generator selects an generator from its list and uses it to create the initial conditions of this event. Then the track manager is asked to compute the tracks which belong to this event. While it does so, using the step manager to move the particle along, the navigator keeps track of the current position of the particle and makes sure that the correct configuration is used. The RootExitCondition checks all active exit conditions, whether the trajectory calculation should continue and terminates the track computation if one of them returns the instruction to stop. Then the computation of this track stops and the computation of the next track starts. This continues until all tracks in an event are processed. With the simulation of the next event, this process repeats itself. After all events have been processed, simulation of one run is complete and the program shuts down.

4.2.1 Field calculation

The field calculation module contains various methods to compute electric and magnetic fields fast and in a reliable manner.

Magnetic fields

The magnetic field of an infinitesimal conductor segment with length $\mathrm{d}\vec{l}$ and current I generates a magnetic field at point $\vec{r}$ according to Biot-Savarts law:

$$\mathrm{d}\vec{B} = \frac{\mu_0}{4\pi}\frac{I\mathrm{d}\vec{l}\times\vec{r}}{r^2} \tag{4.1}$$

The most general computation method for magnetic fields for arbitrary conductors is therefore to discretize the conductor and use the superposition principle to compute the magnetic field. While this is possible with Kassiopeia, the main sources generating magnetic fields in KATRIN are circular coils and superconducting solenoids. In that case, one can make use of the axial symmetry of the KATRIN setup to implify the problem [61, 62]. This leads to so-called elliptic integrals, which can be solved numerically with reasonable efficiency.

Typically, one is primarily interested in the magnetic fields outside the coil windings themselves. In this case, a Legendre polynomial expansion (LPE) around a point on the symmetry axis of the coil, a so called source point, can be used instead [61]. This method is significantly faster in most cases. Dependent on the convergence of the LPE, a speed increase by a factor of 100 or more can be achieved. As shown in Fig. 4.5, such a Legendre polynomial expansion is valid in two regions: if the distance of the field point to the source point ρ is smaller than the minimal distance of the source point to the closest coil ρ_{cen}, the central expansion given by

$$\begin{aligned} B_r &= -s\sum_{n=1}^{\infty}\frac{B_n^{cen}}{n+1}\left(\frac{\rho}{\rho_{cen}}\right)^n P_n'(u) \\ B_\varphi &= 0 \\ B_z &= \sum_{n=0}^{\infty} B_n^{cen}\left(\frac{\rho}{\rho_{cen}}\right)^n P_n(u) \\ &\text{with} \quad u=\cos\theta \quad \text{and} \quad s=\sin\theta \end{aligned} \tag{4.2}$$

can be used. Alternatively, if ρ is larger than the maximal distance of the source point to a coil ρ_{rem}, the remote expansion

$$\begin{aligned} B_r &= s\sum_{n=2}^{\infty}\frac{B_n^{rem}}{n}\left(\frac{\rho_{rem}}{\rho}\right)^{n+1} P_n'(u) \\ B_\varphi &= 0 \\ B_z &= \sum_{n=2}^{\infty} B_n^{rem}\left(\frac{\rho_{rem}}{\rho}\right)^{n+1} P_n(u) \end{aligned} \tag{4.3}$$

is applicable. $P_n(u)$ denotes the n^{th} Legendre polynomial. The coefficients B_n^{cen} and B_n^{rem} need to be computed at every source point in advance. Having more source points increases the validity range, since the convergence radii are determined

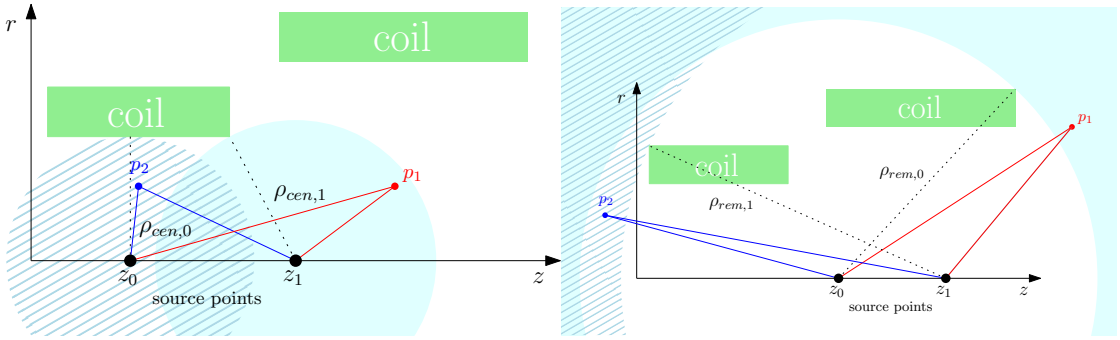

Figure 4.5: **Legendre polynomial expansion** [57]. The magnetic field in point p_1 and p_2 can be computed using the central expansion. Note that without the second source point z_1, only the field at p_2 could be computed, but not the field at p_1. A similar situation is shown in the right figure, where only the field point at p_1 could be computed with the remote expansion without the additional source point z_1.

by the closest, respectively the most remote coil (cf. Fig. 4.5). Additionally, the convergence also increases, since the expansion converges faster if the fractions $\frac{\rho}{\rho_{cen}}$ and $\frac{\rho_{rem}}{\rho}$ are small. Therefore it is advantageous to choose the source point with the smallest fraction. This allows a fast computation of the magnetic field nearly everywhere: Only close to and inside the coils, elliptic integrals have to be solved.

Magnetic fields of coils which do not have a common symmetry axis can be computed with the help of a grouping scheme and coordinate transformations: In the first step, coils with a common symmetry axis are grouped together. Then the source points are computed for every group. The magnetic field is then transformed back into a common reference coordinate system.

An additional KATRIN-specific challenge is the influence of the magnetic materials used in the construction of the experimental hall on the magnetic field in the main spectrometer, in particular in the analysis plane. Since this magnetic field influences the transmission properties of the setup (cf. Eq. (3.4)), stray fields play an important influence. The magnetic field was measured throughout the spectrometer hall in [63]. This measurement can now be used to model the magnetic field with the help of several hundred magnetic dipoles. The position and orientation of these dipoles is determined from the data.

Electric fields

The computation of electric fields turns out to be more challenging than the computation of magnetic fields. The reason for this is that magnetic fields are caused by an electric current, a directly measurable and easily controllable quantity. In contrast, electric fields and potentials are caused by a charge distribution which is generally not known. While one can set the voltage of an electrode, the resulting electric field is strongly influenced by the shape and conductivity of this electrode. An additional KATRIN specific difficulty is due to the fact, that the task at hand is to compute the electric fields inside a large volume enclosed by electrodes. This rules out most common algorithms, for example finite element methods, where the volume itself is divided into a fine meshed grid. For the large geometries in KATRIN,

such a fine-meshed grid would require too much computer memory to be handled efficiently.

The most common solution strategy is the so-called boundary element method, where instead of the entire volume, only the surfaces of the electrodes are discretized. The method relates the unknown charge densities σ_j to the known voltages of the sub elements U_i with a system of linear equations:

$$U_i = \sum_{j=1}^{N} C_{ij}(\vec{r})\sigma_j. \tag{4.4}$$

The Coulomb matrix elements $C_{ij} = C_j(\vec{r_i})$ depend on the geometry and are given by:

$$C_j(\vec{r_i} = \frac{1}{4\pi\epsilon_0}\int_{S_j} \frac{1}{|\vec{r_i} - \vec{r}_S|}\mathrm{d}^2\vec{r}_S \tag{4.5}$$

This system of linear equations can be solved using traditional strategies like the Gauss-Jordan method. There is one noteworthy iterative solution strategy specially adapted to electrostatic problems, the Robin Hood[7] method [64], which has been implemented in Kassiopeia as well. Once the charge densities are known, a zonal harmonic expansion can be used to compute electric fields, analogously to magnetic fields [62].

For both magnetic and electric fields an interpolation method based on three dimensional Hermite polynomials is also available. This is the preferred method for large grids, since its accuracy scales with the 4th power of the grid distance not with the second, which would be the case for a linear interpolation. To achieve this, the partial derivative at the grid points have to be computed in addition to the values itself, which increases the precomputation time (for the same grid size). Interpolation means a dramatic decrease of computation time, in particular for non-axially symmetric setups.

4.2.2 Particle Simulations

Event generation

As stated previously in Sec. 4.1.2, an event represents a physical process which generates one or more primary particles and all its consequences. An event generator simulates this original physical process. While the routines for the trajectory calculations implemented in Kassiopeia and described below are based on extensively tested routines, a common framework for an event generation was completely missing. The task of an event generation framework is relatively straight-forward: Creation of a defined number of physical processes like radioactive decays in a standardized format (an event). The consequences of such a physical process are then simulated by calculating the trajectories of some of the particles involved in this process, together with their interaction with matter. The creation and simulation of secondary particles is generally possible as well.

The event generation framework is discussed in depth in the next Chapter, in particular Sec. 5.3.

[7] The name is due to the fact that the underlying algorithm takes away charge from the rich, i.e. the boundary elements which have too much charge, and gives it to the poor

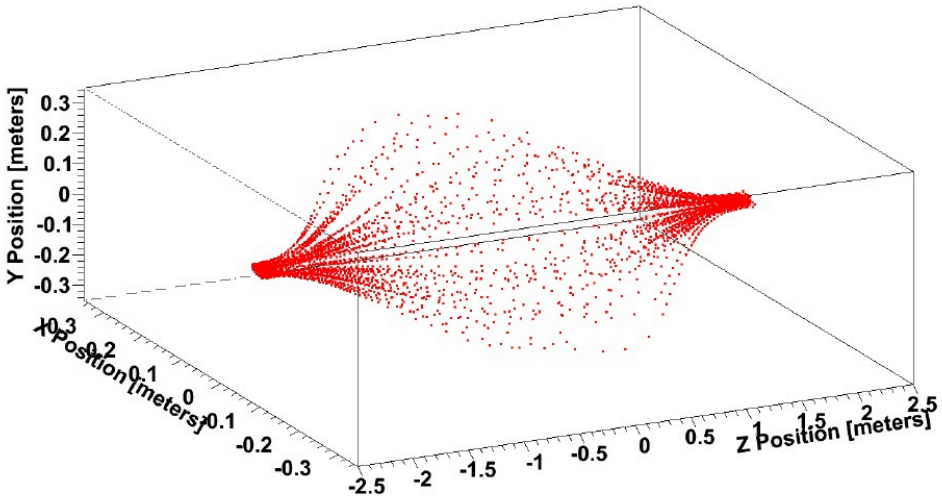

Figure 4.6: **Trajectory of a particle** flying through the KATRIN pre-spectrometer

Trajectory calculation

After the simulation of a physical process like a β-decay with the event generation framework, the consequences of this process are simulated by calculating the trajectories of the involved particles through the experimental setup. The trajectory calculation routines are specialized for two regimes relevant for KATRIN: Most of the experimental setup is under vacuum[8] usually with strong magnetic and electric fields. Two implemented stepping methods can be applied here, both rely on the numerical solution of the underlying equation of motion. The first is the exact solution of the Lorentz equation

$$\ddot{\vec{x}} = q\left(\vec{E} + \vec{v} \times \vec{B}\right) \tag{4.6}$$

which is valid everywhere. An alternative which can be widely used in KATRIN is an approximation for slowly changing magnetic fields. In this case, the cyclotron radius of the particle remains almost constant over one step and the motion can be separated into the guiding center motion and the cyclotron motion. When applicable, this method allows much larger steps and therefore is about a factor 100 faster than the solution of the full Lorentz equation.

Additional processes modifying the electron trajectory like the emission of synchrotron radiation and scattering on gas molecules are also implemented. The latter can also cause the production of secondary electrons, which contribute significantly to the background.

In addition to the physics processes themselves, two more types of strategies have to be configured: Step size controls determine the size of a single step and thus the precision of the simulation. Exit conditions tell the program when to stop the trajectory calculation. In both cases, selection between several different strategies is possible.

The second major trajectory calculation module deals with the detailed simulation of the interaction of electrons inside silicon, the material of the KATRIN main detector.

[8] the maximum pressure in the system, at the injection in the WGTS, is only of the order of a few μbar

It allows to simulate the interaction of a single low-energy electron inside silicon, reproducing precisely the most suitable cross sections available in the literature for an electron energy between 0 and 50 keV. It includes dead layer effects and backscattering, which provides an important tool in understanding the detector response. More details about the KATRIN electron scattering in silicon (KESS) module can be found in [65].

Both sets of trajectory calculation routines have been an invaluable tool in understanding the test experiments at the KATRIN pre-spectrometer, where they have been successfully used to understand for example the background due to radioactive particles [56] or the influence of backscattered electrons [65].

4.2.3 Spectrum Calculation and Analysis Modules

As complementary approach to the calculation of trajectories, Kassiopeia also includes routines to compute the energy spectra at various places in the setup based on a detailed model of the KATRIN experiment. The development of this model and a corresponding analysis tool constitutes a major part of this thesis and is therefore described in more detail in the next Chapter. Both approaches have their specific advantages: The understanding of background sources in the spectrometer section is not possible without a detailed and precise particle simulation, see e.g. [56]. However, the simulation of 10^{11} electrons per second coming from the WGTS in a reasonable time period is impossible. On the other hand, both approaches can easily be combined, e.g. by using the spectrum calculation to compute the high energy tail of the differential spectrum entering the spectrometer section and simulate only these electrons in detail which have a chance to be transmitted. Alternatively, one can directly compute the integrated spectrum and only switch to a particle-by-particle simulation of the detector and DAQ response. Since the changeover from the spectrum approach to the particle approach can be done at various steps and therefore has to be flexible, both approaches have been combined within one framework, Kassiopeia.

In combination with the analysis routines described at the end of the next chapter, these spectrum calculation routines can be used to investigate the statistical sensitivity and the systematic influences of the experimental setup in great detail.

5. Simulation and Analysis of the KATRIN tritium source

After the overview of the simulation package as a whole, this chapter focuses on specific parts of the simulation and analysis routines which constitute the major part of this thesis. The first section 5.1 discusses the various corrections to the integrated spectrum measured in KATRIN. It is followed by a detailed overview of the simulation and modeling modules in Kassiopeia developed as part of this thesis in Sec. 5.2 and 5.3, while concluding with a description of the corresponding analysis routines in Sec. 5.4.

5.1 Modifications to the spectrum

The influence of a non-vanishing neutrino mass on the energy spectrum β-decay electrons is most pronounced in a narrow interval close to the endpoint of the spectrum (cf. Eq. (2.31)). Any experimental or theoretical modification of this spectral shape leads to systematic errors in the neutrino mass determination. Therefore, a dedicated simulation is needed which incorporates both experimental effects and theoretical modifications in a coherent and unified way. The first two sections of this chapter discuss the underlying physical phenomena. They can be subdivided into influences on the decay process itself - discussed in Sec. 5.1.1 - and in modifications to the electron energy on its way to the detector, cf. Sec. 5.1.2. The remaining part of this section is dedicated to discuss how the measured spectrum is influenced by the experimental conditions foreseen in KATRIN due to these effects.

5.1.1 The electron emission

A variety of processes can modify the electron energy directly during the emission process and thus lead to a modification of the differential spectrum as given in its simplest form in Eq. (2.31). First, radiative corrections due to photon emission take away energy from the electron and thus slightly reduce the observed rate at higher energies. Second, the recoil energy transferred to the nucleus is finite and has to be

included. Third and most notably, however, is the fact that the daughter nucleus remains in an excited state, and thus the electron energy is further reduced. The two last points depend on the different tritiated isotopologues of molecular hydrogen, T_2, DT, and HT. Finally, the finite temperature of the gaseous tritium source causes a smearing of the electron energy due to the Doppler effect.

Radiative corrections

Contributions of virtual and real photons during the emission of the decay electron modify the energy of the β-electron. These radiative corrections lead to an additional multiplicative factor $f_{rad}(E)$ in the differential spectrum Eq. 2.31:

$$\frac{\mathrm{d}N}{\mathrm{d}E} = C{\cdot}F(Z,E){\cdot}K(p,E){\cdot}\mathbf{f_{rad}}(\mathbf{E}){\cdot}(E_0-E)\sqrt{\left((E_0-E)^2-m_{\overline{\nu_e}}^2\right)}\Theta\left(E_0-E-m_{\overline{\nu_e}}\right) \tag{5.1}$$

Implemented in the spectrum calculation software (SSC) is the result obtained in [66]:

$$\begin{aligned} f_{rad}(E) =& (W-\epsilon)^{(2\alpha/\pi)t(\beta)}\left[1+\frac{2\alpha}{\pi}\left\{t(\beta)\left[\ln 2-\frac{3}{2}+\frac{(W-\epsilon)}{\epsilon}\right]\right.\right. \\ &+\frac{1}{4}[t(\beta)+1]\left[2(1+\beta^2)+2\ln(1-\beta)+\frac{(W-\epsilon)^2}{6\epsilon^2}\right] \\ &\left.\left.-2+\frac{1}{2}\beta-\frac{17}{36}\beta^2+\frac{5}{6}\beta^3\right\}\right] \end{aligned} \tag{5.2}$$

$$\text{with:}\quad W = \frac{E_0+m_e}{m_e} \tag{5.3}$$

$$\epsilon = \frac{E+m_e}{m_e} \tag{5.4}$$

$$\beta = \frac{p}{E+m_e} \tag{5.5}$$

$$t(\beta) = \frac{1}{2\beta}\ln\frac{(1+\beta)}{(1-\beta)} \tag{5.6}$$

As can be seen in Fig. 5.1, this correction leads to a small reduction f_{rad} in the decay rate, which is most pronounced near the endpoint of the spectrum. Far away from this point the radioactive corrections remain very close to unitiy.

Nuclear recoil

During the β decay, the nucleus experiences a recoil due to energy and momentum conservation and therefore its momentum and energy are modified. The remaining nucleus HeX (X=H, D, T) takes away the recoil energy E_{rec}, which is no longer available to the lepton pair:

$$\begin{aligned} E_{rec} = \frac{p_{rec}^2}{2M_{HeX}} &= \frac{p_e^2}{2M_{HeX}} \approx E\frac{m_e}{M_{XT}} \\ \text{using } p_e^2 &= E_{tot}^2 - m_e^2 = (E_{kin}+m_e)^2 - m_e^2 \\ &= E_{kin}^2 + 2m_eE_{kin} \approx 2m_eE_{kin}. \end{aligned} \tag{5.7}$$

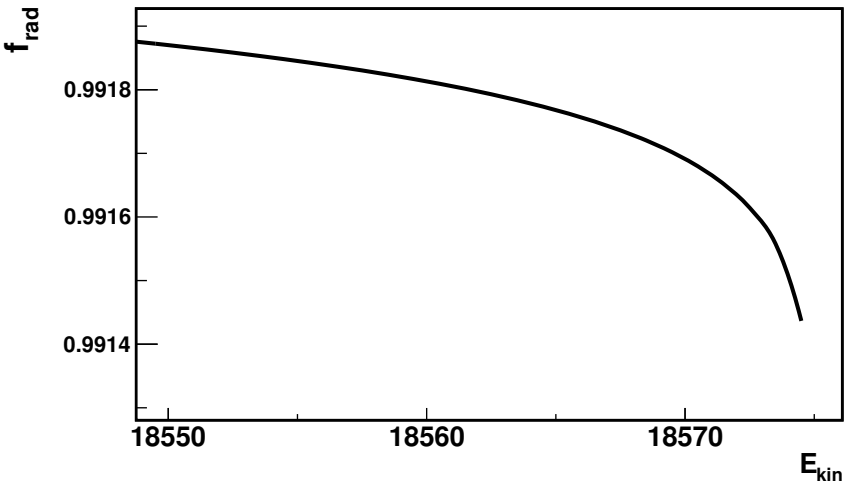

Figure 5.1: **Radiative corrections near the endpoint**, calculated with Eq. (5.2). The radiative corrections reduce the rate by less than 1% and are most pronounced near the endpoint of the β spectrum.

For Tritium gas of 100% purity, this would manifest itself in a shifted endpoint E_0 and would have no effect on the neutrino mass measurement; only the spectral shape is used to determine $m^2_{\overline{\nu}_e}$. However, the molecular tritium gas in the WGTS consists mainly of T_2 with a small fraction of other hydrogen isotopologues, mainly the tritiated molecules, DT and HT. In this regard, it is important to note that the recoil energy depends on the mass of the nucleus: For HeT, the recoil energy is approximately 1.7 eV, for HeD 2.0 eV and for HeH 2.5 eV. Therefore, KATRIN measures a superposition of three β spectra with different endpoints. Knowledge of the gas composition becomes mandatory and has to be monitored continuously by Laser Raman spectroscopy, as mentioned in Sec. 3.2. The linear dependence of the nuclear recoil on the electron energy can usually be neglected, as these numbers change only by about 10^{-3} in the region of interest 50 eV below the endpoint.

Final State Distribution (FSD)

In case of a tritium β decay, a non negligible fraction of the decay energy remains in the daughter molecule causing internal excitations. The possible excitations can be categorized as follows:

- rotational and vibrational energies: The rotational and vibrational excitations of Tritium are only a few eV. Hence, their influence on the neutrino pronounced. The total probability for the molecule to end up in an excited rovib state is about 57%, with an average excitation energy of 1.7 eV.
- electronic excitations: Most of the remaining possible excitation energies of 43% is located in electronically excited states, which start at about 20 eV.
- electronic continuum: above the dissociation threshold of the respective isotopologue of about 35 eV, the final state distribution becomes continuous.

Consequently, Eq. (5.1) has to be modified to include a sum over all possible final states f of the daughter molecule, weighted with the probability P_f to excite the respective state of the daughter molecule, while subtracting the energy of the corresponding final state, E_f:

$$\frac{\mathrm{d}N}{dE} = C \cdot F(Z,E) \cdot K(p,E) f_{rad}(E) \sum_f P_f \left(E_0 - E_f - E\right) \sqrt{\left(\left(E_0 - E_f - E\right)^2 - m_{\overline{\nu_e}}^2\right)} \Theta\left(E_0 - E_f - E - m_{\overline{\nu_e}}\right) \quad (5.8)$$

Since the final state distribution depends on the isotopologue, this is another reason where the gas composition influences the differential spectrum.

The spectrum calculation software includes the most recent calculations of excited state distributions of T_2 and for the first time DT. The exited states have been calculated in 10 meV bins in [67, 68] by solving the effective Schroedinger equation

$$-\frac{1}{2\mu}\frac{\mathrm{d}^2 f_{n\nu J}(R)}{\mathrm{d}R^2} + U_{nJ}^{eff}(R) = E_{n\nu J} f_{n\nu J}(R) \quad (5.9)$$

in the Born - Oppenheimer approximation. This approximation separates the dynamics of the nucleus from the dynamics of the electronic hull, since the time scales differ strongly due to the heavier mass of the nucleus. The parameter μ is the reduced mass of the hydrogen molecule, $E_{n\nu J}$ the energy of the rovibrational state and $U_{nJ}^{eff} = \frac{J(J+1)}{2\mu R^2} + U_{BO}(R) + ...$ the effective one-dimensional potential, which contains U_{BO}, the electronic potential in the Born Oppenheimer approximation. This procedure is well established and has been used in previous calculations, e.g. [69]. In this latest publication, the final states for initial rotational states up to J=3 have been calculated for the first time. The dependence on the angular momentum of the initial state is shown in Fig. 5.2. At 30 K, only about 43% of the tritium molecules are in the rotational ground state (J=0), while 56% are in the first excited state (J=1). The remaining 1% fall almost completely in the J=2 state with a small fraction (0.0001%) in the J=3 state. The final state distributions of T_2 and DT are shown in Fig. 5.3.

The excited states of normal hydrogen are taken from an older work [69], where a coarser binning of 0.1- 4 eV was used while only J=0 being included. In both cases, the final state distributions of all the isotopologues are already shifted by their respective recoil energies. The final state distribution of HT are of less importance, since the fraction of HT will be small. It will at most be important in the early phases of the KATRIN experiment, when hydrogen is expected to emanate from the beam tube walls. In the long term, the walls will be saturated with Tritium so that the HT content will drop.

Doppler effect

Since the KATRIN experiment employs a gaseous source, the energy of the electron is modified by the thermal Doppler effect. In the non-relativistic limit, the energy for an electron in the lab system E' differs from the energy in the tritium rest frame E by:

$$\Delta E = E_f - E_i = \frac{1}{2} m_e \left(\vec{v}_e^2 + \vec{v}_{T_2}^2\right) - \frac{1}{2} m_e \vec{v}_e^2 \quad (5.10)$$

$$\approx m_e \left|\vec{v}_e\right| \cdot \left|\vec{v}_{T_2}\right| \cdot \cos\theta \qquad \text{since } \left|\vec{v}_e\right| \gg \left|\vec{v}_{T_2}\right| \quad (5.11)$$

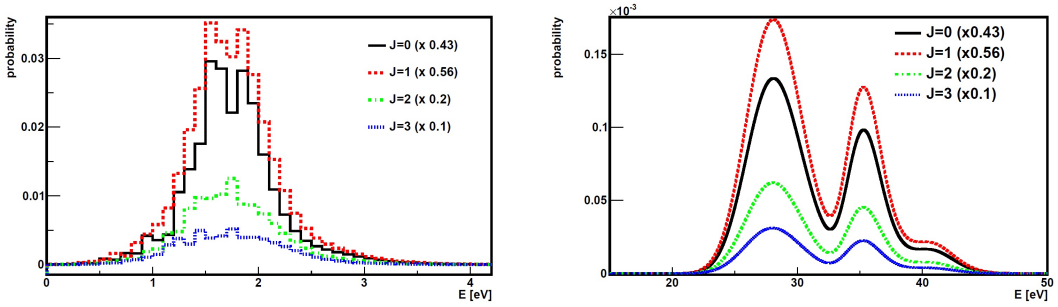

Figure 5.2: **Final state distribution of HeT** for different rotational excited states of the initial state, T_2. The left figure shows the rotational and vibrational final states with an excitation energy of a few eV, while the right plot shows the electronic excitations. The different lines correspond to different rotational excitations of the mother molecule. The continuous black line corresponds to the 43% contribution of initial ground states (J=0), the dashed red line to the dominant 56% of J=1 states. While for these two their correct weight has been applied, the J=2 green dashed-dotted line (J=3 blue dotted line) has been scaled by a factor of 0.2 (0.1), instead of their actual contributions of 0.01(0.000001). The rotational and vibrational states are grouped in 0.1 eV bins here, see Fig. 5.3 for the full 0.01 eV wide binning.

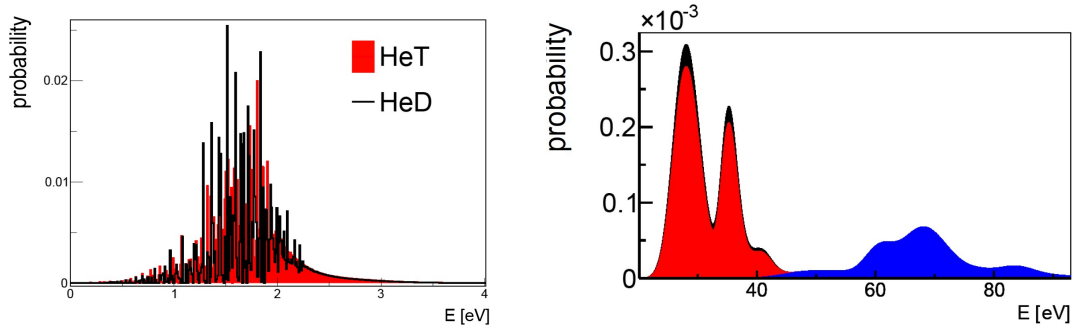

Figure 5.3: **Rotational and vibrational excited states of HeT and HeD** with a binning of 0.01 eV. In the left figure, the red histogram contains the rotational and vibrational final states of HeT, the corresponding states of HeD are shown in black. The right plot shows the superposition of the electronic excitations: the electronically bound states of HeT are shown again in red, the additional contribution of the bound states of HeD in black. At about 35 eV, the electronic continuum shown in blue starts.

Here, $\vec{v_e}$ and $\vec{v_{T_2}}$ denote the velocities of the electron and the tritium molecule in the lab frame and θ the angle between the two velocities. By inserting typical values in Eq. (5.11) to estimate the order of magnitude of the effect, one can compute that for the most probable speed at a temperature of 30 K, $|\vec{v}_{T_2}| = 288\frac{\mathrm{m}}{\mathrm{s}}$, the energy of an endpoint electron with an energy of 18575 eV is shifted by $\cos\theta \cdot 0.13$ eV. However, due to the random orientation of θ, the Doppler effect causes a convolution of the differential spectrum with the Doppler convolution function $g(\Delta E)$, not simply an energy shift. The Doppler convolution function is determined from the velocity distribution function of the tritium molecules. Assuming this to be a Boltzmann distribution:

$$g(v_{T_2}^{||}) = \frac{1}{\sqrt{2\pi}\sigma_v} \exp\left[-\frac{1}{2}\left(\frac{v_{T_2}^{||}}{\sigma_v}\right)^2\right] \tag{5.12}$$

where $v_{T_2}^{||} = v_{T_2}\cos\theta$ is the velocity component of the T_2 molecule parallel to the electron emission and $\sigma_v = \sqrt{\frac{k_B T}{M_{T_2}}}$. Substituting Eq. (5.11) in Eq. (5.12) leads to the energy convolution function

$$g(\Delta E) = \frac{1}{\sqrt{2\pi}\sigma_E} \exp\left(-\frac{1}{2}\left(\frac{\Delta E}{\sigma_E}\right)^2\right) \tag{5.13}$$

which is again a Gaussian, with width $\sigma_E = \sqrt{2E_i k_B T \frac{m_e}{m_{T_2}}}$. In order to save computing time, it is more efficient to convolute the final state distribution discussed previously instead of the differential spectrum itself - the latter would require a numerical integration each time a differential rate is computed. Both methods are implemented and the results are identical for all practical purposes. The resulting final state distribution after the convolution with the Gaussian energy distribution is shown in Fig. 5.4. The strong bin to bin variations of the original final state spectrum are completely smeared out due to the Doppler effect.

As will be discussed in more detail in Sec. 5.1.3, the tritium molecules follow a slightly modified Maxwell Boltzmann distribution, since in addition to the random thermodynamical gas flow, there is a net flow of tritium molecules from the injection to both exits. Nevertheless the velocity is largely dominated by the thermal component.

5.1.2 The Electron transport

While the previous section discussed modifications to the electron spectrum associated with the emission process, this section describes additional spectral variations from effects of the electron transport to the detector. In particular, such changes modify the probability for an electron to reach the main detector. This probability is expressed by the KATRIN response function defined in Sec. (3.5). It consists of a convolution of the energy loss function of the source and the transmission probability of the main spectrometer.

Energy losses

The main physical process which causes an energy loss of an electron on its way to the detector is inelastic scattering. Other effects, in particular elastic scattering and synchrotron radiation are only of secondary relevance and will be briefly discussed afterwards.

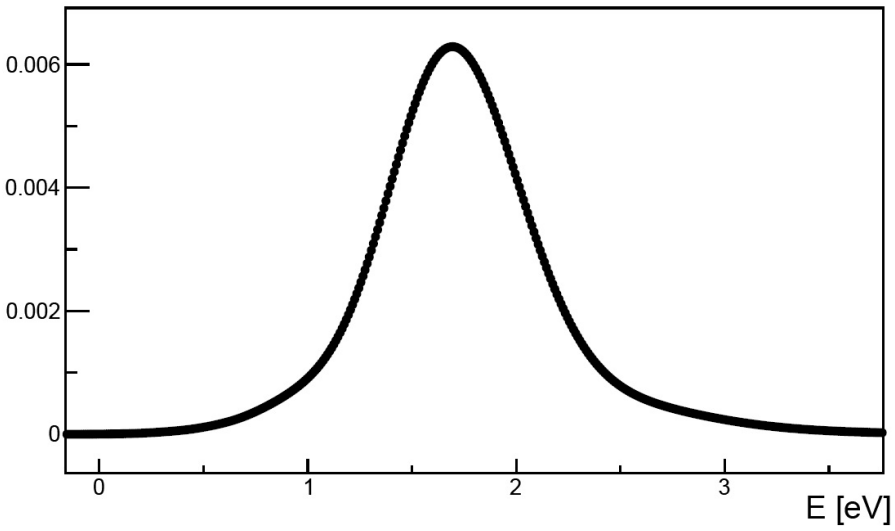

Figure 5.4: **Rotational and vibrational final states including energy smearing due to the Doppler effect** for a temperature of 30 K, in 0.01 eV binning. In comparison to Fig. 5.3, the small structures have disappeared completely.

Inelastic scattering

The most important influence on the electron spectrum results from the energy losses due to inelastic scattering. This energy loss happens predominantly in the WGTS, in particular the central part, where the gas density is highest. It can be parametrized by the energy loss function $E_{loss}^{WGTS}(\epsilon)$, which describes the likelihood for an electron to loose the energy ϵ due to inelastic scattering. Since the electrons can scatter multiple times, $E_{loss}^{WGTS}(\epsilon)$ is the sum over the likelihoods P_i for an electron to scatter i times, multiplied with the energy loss function for i scatterings. This in turn is given by the i^{th} convolution of the energy loss function $f(\epsilon)$ for scattering once:

$$E_{loss}^{WGTS} = P_0\delta(\epsilon) + P_1 f(\epsilon) + P_2 f(\epsilon) \otimes f(\epsilon) + \dots \,. \tag{5.14}$$

As can be seen in Fig. 5.5, the minimum energy loss for one inelastic scattering is about 10 eV, therefore the sum can usually be terminated after 5 summands, because for nearly all measurements, in particular the standard neutrino mass analysis, only the spectrum about 50 eV below the endpoint is of relevance.

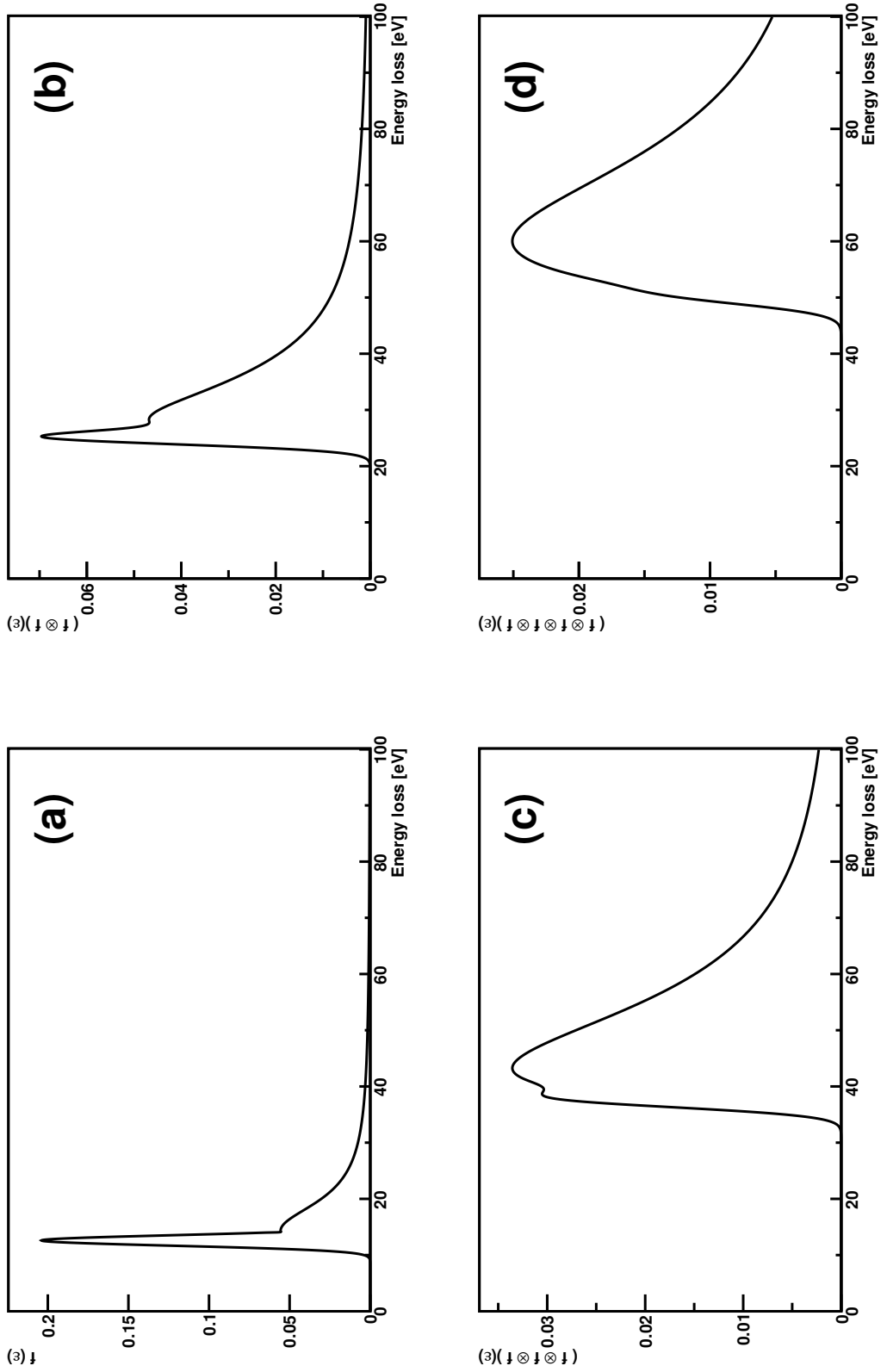

Figure 5.5: **The first four contributions to the energy loss function**. Since the energy loss for a single scattering is about 10 eV (top left), an electron that scatters n times looses at least n times 10 eV. The energy loss for n=2 (3, 4) is shown in the top right(bottom left, bottom right) figure.

The energy loss function of tritium has been determined by the predecessor experiments MAINZ and TROITSK in Ref. [70]. It can be parametrized with the following function:

$$f(\epsilon) = \begin{cases} A_1 \exp\left(-\frac{2(\epsilon-\epsilon_1)^2}{\omega_1}\right) & \epsilon < \epsilon_c \\ A_2 \frac{\omega_2^2}{\omega_2^2+4(\epsilon-\epsilon_e)^2} & \epsilon \geq \epsilon_c \end{cases} \tag{5.15}$$

with $A_1 = 0.204(1), \omega_1 = 1.85(2), A_2 = 0.0556(3), \omega_2 = 12.5(1)$ and $\epsilon_2 = 14.30(2)$. $\epsilon_1 = 12.6$ and $\epsilon_c = 14.09$ were chosen such that $f(\epsilon)$ is continuous. The energy loss function of tritium will be measured with the KATRIN experiment more precisely with the help of an electron gun located in the rear section. Measuring the fraction of scattered electrons for different column densities allows to extract the energy loss function with a deconvolution method [25].

The probabilities P_i in Eq. (5.14) for an electron to be emitted at position z under angle θ to the z axis to scatter i times while traversing the WGTS follow a Poissonian distribution:

$$P_i(z,\theta) = \exp\left(-\lambda(z,\theta)\sigma_{tot}\right) \frac{\left(\lambda(z,\theta)\sigma_{tot}\right)^i}{i!} \tag{5.16}$$

While the cross section for inelastic scattering σ_{inel} is to good approximation constant in the region of interest, with a value of $\sigma_{tot}(18600eV) = 3.4 \cdot 10^{-18}$ cm^{-2} , the effective column density along the path of the electron $\lambda(z,\theta)$

$$\lambda(z,\theta) = \frac{1}{\cos\theta} \int_z^L \rho(z')dz' \tag{5.17}$$

depends on the position along the axis of the decay and the starting angle. The upper limit of the integral L denotes the z position at the end of the source, which is assumed to be radially and azimuthally homogeneous. Otherwise, an additional averaging over the radial and azimuthal coordinates would have to be performed as well.

Integrating over this dependency allows to calculate average scattering probabilities for either the complete WGTS ($z_1 = 0, z_2 = L$) or a part of the source:

$$P_i(z_1,z_2) = \frac{1}{\rho d(z_1,z_2)\left(1-\cos\theta_{max}(z)\right)} \int_{z_1}^{z_2} \int_0^{\theta_{max}(z')} \rho(z') P_i(z',\theta) \sin\theta \mathrm{d}\theta \mathrm{d}z' \tag{5.18}$$

where $\rho d(z_1,z_2)$ is the column density

$$\rho d(z_1,z_2) = \int_{z_1}^{z_2} \rho(z')dz'. \tag{5.19}$$

The angular integral runs from 0 to the maximal accepted angle θ_{max}, which depends on the maximal magnetic field B_{max} along the trajectory and the magnetic field strength at the decay point

$$\theta_{max}(z) = \arcsin\left(\sqrt{\frac{B_S(z)}{B_{max}}}\right). \tag{5.20}$$

For the nominal values of $B_{max} = 6.0$ T and $B_S = 3.6$ T, the maximum accepted angle θ_{max} is about 50.7°, however B_S is slightly position dependent (cf. Sec 5.1.3).

Table 5.1: **Scattering probabilities**.

Number of inelastic interactions	Probability	Number of inelastic interactions	Probability
0	0.412	5	$11.2 \cdot 10^{-3}$
1	0.292	6	$3.50 \cdot 10^{-3}$
2	0.168	7	$9.60 \cdot 10^{-4}$
3	0.0797	8	$2.44 \cdot 10^{-4}$
4	0.0321	9	$5.65 \cdot 10^{-5}$

The first 10 scattering probabilities are listed in Tbl. 5.1. For each interaction, the electron looses at least 10 eV, so for an energy interval of 50 eV, only the left column is relevant. In case a larger energy interval is of interest, a larger number of interactions needs to be taken into account, as well as the fact that the approximation of an energy-independent cross section is no longer valid. The probabilities in Tbl. 5.1 add up to 99.998%, so 10 or more interactions can probably be ignored also in this case. The values depend slightly on the thermodynamical boundary conditions, in this case an temperature of 30 K, an injection pressure p_{in} of $3.368 \cdot 10^{-3}$ mbar and an exit pressure of 5% $\cdot p_{in}$ was used.

From this one can compute the energy loss function Eq. (5.14) and with the transmission function Eq. (3.4), ultimately the response function Eq. (3.5). This response function of the KATRIN experiment is shown in Fig. 5.6.

Elastic scattering

In addition to inelastic scattering, the β-decay electron can also undergo elastic scattering. However, the elastic cross section of 18.6 keV electrons with tritium molecules is 12 times smaller than the inelastic scattering. Additionally, the average energy loss in elastic scattering on tritium is only a few meV. Elastic scattering is forward peaked and the average angular change is only about 3°. Nevertheless, elastic scattering causes a slight modification of the response function, which causes a systematic error of $\sigma^{syst}_{m^2_\nu} = 2.5 \cdot 10^{-3}$ eV^2 if not taken into account in the analysis.

Synchrotron radiation

Since the electrons are guided to the detector along magnetic field lines, they are subject to energy losses due to synchrotron radiation. In the non-relativistic limit, the energy loss per unit time interval is given by:

$$\frac{\partial E}{\partial t} = 0.4 E_\perp B^2 \tag{5.21}$$

The energy loss is most pronounced for electrons with a large starting angle θ with respect to the magnetic field ($\theta_{max} = 50.7°$). For such an electron, the energy loss between source and detector is 130 meV, concentrated in the regions of strong magnetic field in the transport section. The energy loss in the WGTS itself, which also depends on the position of the β-decay, is at most 12 meV, for an electron traversing the entire WGTS with the maximal accepted angle θ_{max}. Since the energy loss due to synchrotron radiation depends on the starting angle θ, it modifies the transmission function. The magnetic fields are known, therefore the effect on the transmission function can be computed accurately [25].

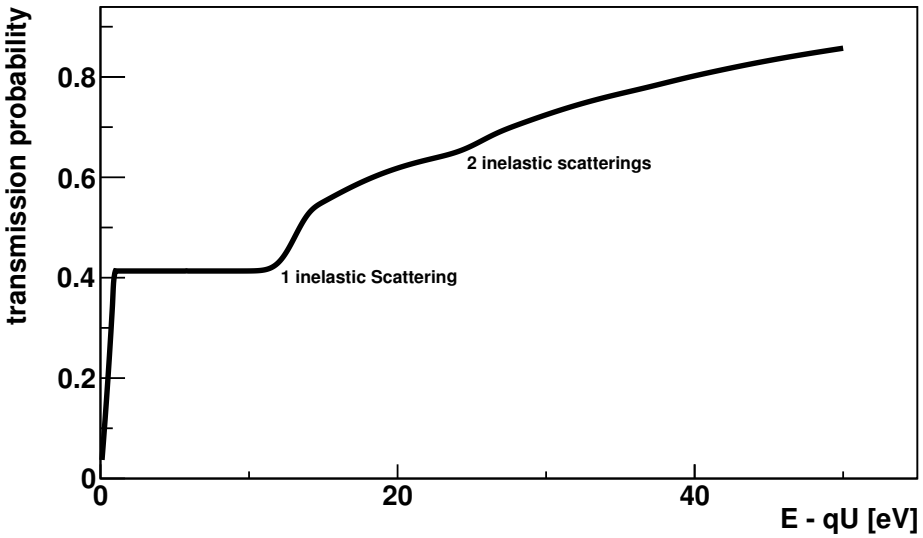

Figure 5.6: **Response function of the KATRIN experiment**. The almost linear steep rise at the beginning is due to the transmission function of the main spectrometer. Then, there is a plateau between 1 and 12 eV, where the spectrometer operates at full transmission, but only electrons with no inelastic energy losses can reach the detector. At about 12 eV, electrons may undergo one inelastic scattering in the source and still retain enough surplus energy to be transmitted. At 24 eV, the surplus energy can be sufficient even after two interactions. Further increases due to three and more interactions at 36, 48, ... eV are too small to be visible.

Transmission probability

The transmission function Eq. (3.4) depends on the magnetic configuration of the experiment. The ratio between the magnetic field in the source and the magnetic field in the analysis plane determines the effectiveness, with which the electron momentum is parallelized by magnetic adiabatic collimation for the energy analysis in the MAC-E filter, cf. Sec. 3.1. Small imperfections in the electromagnetic design discussed in more detail in Sec 5.1.3 therefore influence the transmission probability.

5.1.3 Experimental influences on the spectrum

Source magnetic field

The WGTS features an axial magnetic field of 3.6 T to guide the β-electrons out of the WGTS. The magnetic field is therefore oriented along the WGTS axis, so $\vec{B} = (0, 0, B)$. For technical reasons, the WGTS does not feature a single 10 m long magnet, but three shorter ones. Despite additional correction coils in between these magnets, the magnetic field drops from 3.6 T to about 3.55 T at the two changeovers, which decreases the accepted angle from 50.7° to 50.3° in two regions of about 0.5 m length in about 2 m distance from the center of the WGTS (cf. Fig. 5.7). This slightly modifies the transmission probabilities for electrons decaying in these regions and thus has a systematic impact on the spectrum. Additionally,

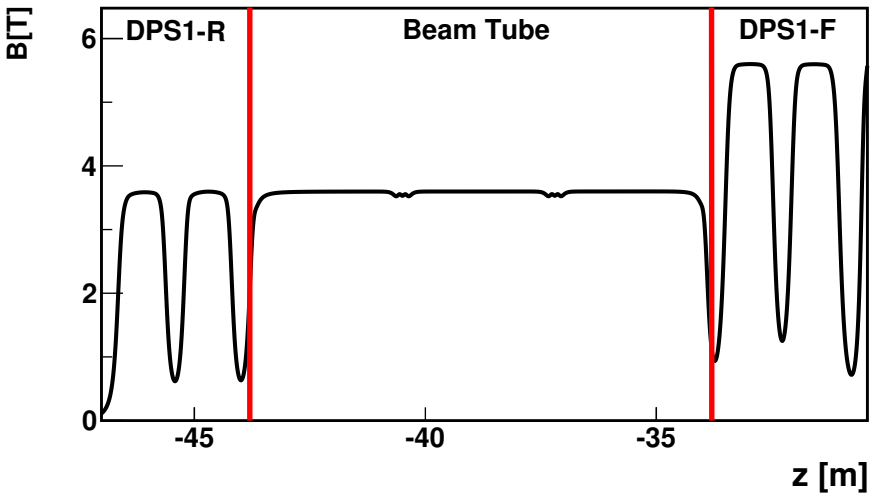

Figure 5.7: **The magnetic field along the WGTS** including the pump port sections. The magnetic field is perfectly homogeneous along most of the WGTS beam tube, but in two regions at $z \approx -40.5$ m and $z \approx -37.5$ m small inhomogeneities are present. See text for details.

the magnetic field in the pump ports drops below 1 T, however due to the low gas density there, this also has only a small influence on the measured spectrum.

Magnetic field in the analyzing plane

A MAC-E filter like the KATRIN spectrometer uses magnetic collimation to convert the electron momentum transverse to the electric field into longitudinal momentum. When these electrons are maximally collimated, their energy is analyzed by the retarding potential. This is called the analyzing plane. Since the magnetic field in the analyzing plane drops to $3 \cdot 10^{-4}$ T, the influence by stray fields like the earth magnetic field becomes non-negligible. Although dedicated compensation coils surround the main spectrometer, the compensation is not perfect. Moreover, small effects of the imperfect compensation of external magnetic fields by the air coil system and imperfections in the air coil system itself have to be considered. This causes azimuthal variations of the magnetic field in the analysis plane [71]. These effect the transmission function of the main spectrometer. Dedicated measurements of the magnetic fields in the main spectrometer hall have been carried out in [63] and the magnetic field in the spectrometer hall will be extensively monitored during the operation of the KATRIN experiment [72].

Electric potential fluctuations

The WGTS activity of 10^{11} Bq implies that about 10^{11} electrons follow the magnetic field lines and leave the source every second, while the positive ions remain behind. This can cause space charging in the WGTS. This would in turn lead to variations in the source potential and thus to a dependence of the retarding potential on the starting point of the electron. On their way through the source, one β-electron

produces on average about 15 electron-ion-pairs through ionization processes [25]. These electron-ion-pairs form a quasi-neutral plasma with a density of about 10^6 electron-ion-pairs per cm^3. Previous MC studies summarized in [25] showed that the electrons cool down to the gas temperature of 30 K almost immediately (within a few ms). This implies that most of the electrons inside the WGTS should have an energy of a few meV. The diffusion length scale along magnetic field lines is of about 1 m, therefore the longitudinal conductivity along the magnetic field is still large. This implies that any potential fluctuations in the source would be immediately compensated and the potential fluctuations in the WGTS should be of the order of a few times the electron characteristic energy of a few meV. Nevertheless, the WGTS features a special operational mode to investigate fluctuations of the potential, the Krypton mode. By inserting a small ($\approx 10^{-8}$) fraction of ^{83}Kr to the tritium gas, the shape of the narrow Krypton lines at 17 and 32 keV can be precisely measured and analyzed to search for any potential fluctuations.

Temperature profile

The temperature profile along the beam tube influences the measured spectrum three-fold: First, it is an important boundary condition for the density calculation as discussed below. Second, it directly influences the electron energy via the Doppler effect according to Eq. (5.11). The third influence is due to the different population of initial rotational states for different temperatures, which slightly changes the final state distribution. The main reason for an inhomogeneous temperature profile is the radiation coming from the pump ports. Since the heat arriving at a z position along the beam tube is determined by the solid angle of the beam tube opening at the end, the temperature increase is most pronounced close to the pump ports. The temperature at both sides of the beam tube is determined by the two phase cooling tubes, therefore this radiative heat load causes an azimuthal temperature increase, where the maximal deviation from the beam tube temperature $\Delta T(z)$ is determined by this heat load and therefore depends on the longitudinal position.

The demonstrator test experiment described in Sec. 3.2.2 was designed to verify the stability of the cooling system of the WGTS. A brief selection of results is shown in Fig. 5.8, more details about the measurements can be found in [73, 74]. For the stability of the two phase system, the Demonstrator was a complete success: As shown in Fig. 5.8(a), the temperature varies only by less than $1\frac{\mathrm{mK}}{\mathrm{hour}}$, which exceeds the KATRIN requirement of $\frac{\Delta T}{T\Delta t} < \frac{10^{-3}}{\mathrm{hour}}$ (corresponding to $\frac{\Delta T}{\Delta t} = 30\frac{\mathrm{mK}}{\mathrm{hour}}$) by an order of magnitude.

The demonstrator also allowed to determine the temperature profile. While the rear side shows the expected behavior, the beam tube temperature on the front side rises by several K towards the DPS1-F pump port. Such a large increase can only be explained by conductive heating. The most likely explanation is additional conductive heat via the vapor pressure pipes to the outside. During the reassembly of the demonstrator to the WGTS, additional thermal contacts of these vapor pressure pipes to cooling reservoirs will be installed to prevent this effect. Nevertheless, the effect of such a temperature profile on the KATRIN sensitivity is investigated in Sec. 6.2.3.

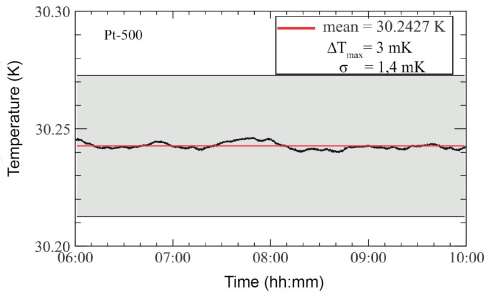

(a) Stability of the beam tube temperature [73]

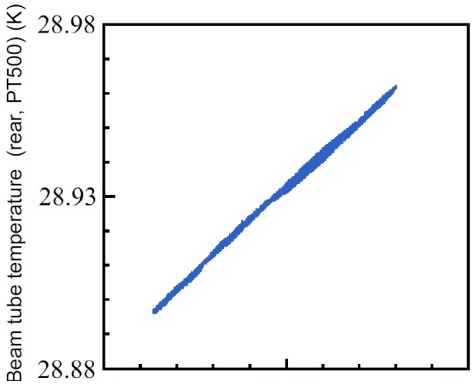

(b) Correlation between the temperature obtained from the vapor pressure in the Neon tube and a PT500 temperature sensor directly on the beam tube [74]

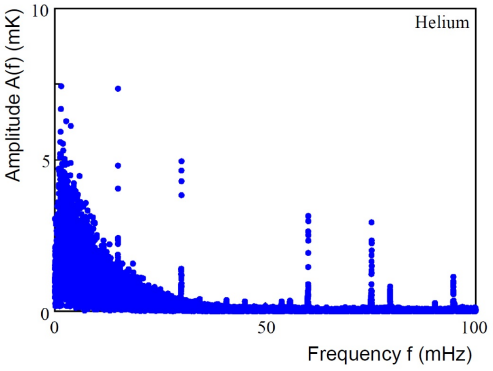

(c) Fourier Transformation of the Helium temperature at the inlet of the condenser [74]

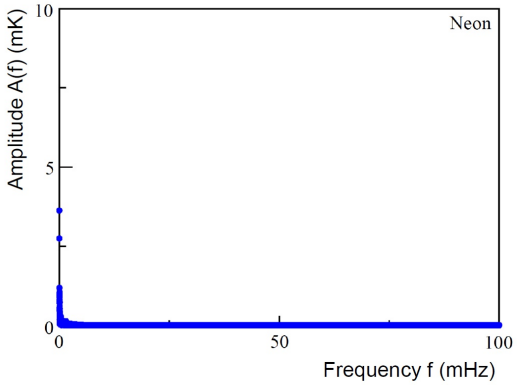

(d) Fourier Transform of the beam tube temperature [74]

Figure 5.8: **Results of the demonstrator test setup**. Fig 5.8(a) shows the temperature measured by a single PT500 sensor along the beam tube. The temperature variation is an order of magnitude smaller than the specified range shown as grey band [73]. The correlation between the two independent temperature measurements - the vapor pressure in the Neon tube and a PT500 temperature sensor on the beam tube is shown in Fig.5.8(b). The PT500 sensors themselves are almost perfectly correlated, with correlation coefficients > 0.99 [74]. Finally, the two bottom figures show the Fourier transformations of the Helium inlet (Fig. 5.8(c)) and the temperature obtained from the Neon vapor pressure (Fig. 5.8(d)). As can be seen, the custom designed condenser, which couples the Helium and Neon circuits (cf. Fig. 3.5) damps frequencies $f > 0.3$ Hz by at least two orders of magnitude and ensures the excellent stability of the system.

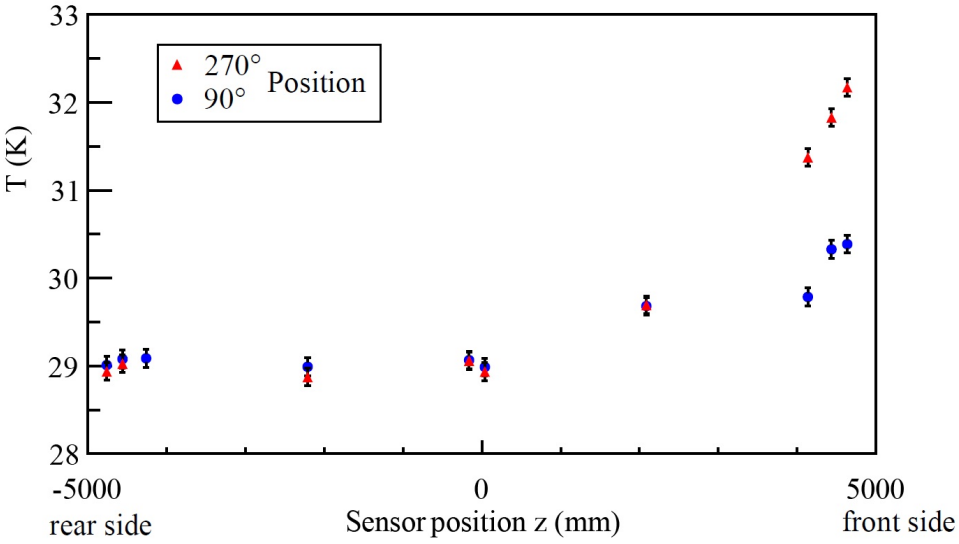

Figure 5.9: **Temperature profile measured along the beam tube of the WGTS demonstrator [74]**. The error bars display the systematic errors due to the still missing calibration of the PT500 temperature sensors. Statistical errors would be invisible. While the temperature on the rear side remains stable, there is an increase by about 3 K on the front side.

Velocity profile

The velocity distribution of the tritium gas is influenced by two effects: First of all, the tritium molecules display a thermal velocity. In a closed system, this would be given by a Maxwell Boltzmann distribution:

$$f(\vec{r},\vec{v}) = \frac{n(z)}{\left(\sqrt{\pi}v_0\right)^3}\exp - \left[\frac{v_x^2+v_y^2+v_z^2}{v_0^2}\right] \tag{5.22}$$

However, the WGTS is not a closed system since the tritium molecules are pumped out at the end. Therefore, the tritium molecules have an additional velocity component, which takes into account their streaming from the injection to the pump ports. The average value of this velocity component is the bulk velocity $U_z(z,r,\delta)$.

With the gas dynamical simulations discussed below, the velocity distribution has been simulated numerically in [75]. The results showed that the velocity distribution is well described by a shifted Maxwellian:

$$f(\vec{r},\vec{v}) = \frac{n(z)}{\left(\sqrt{\pi}v_0\right)^3}\exp - \left[\frac{v_x^2+v_y^2+(v_z-U_z)^2}{v_0^2}\right]. \tag{5.23}$$

The agreement in the inner part of the tube is excellent, the deviation near the pump ports can be a few %. However, in this region, the gas dynamical code is not valid anymore in any case, since it uses a simplified geometry, which does not correctly treat end effects.

The bulk velocity $U(z,r,\delta)$ obeys the following equation:

$$U_z(z,r,\delta) = v_0\frac{R}{P(z)}\frac{\mathrm{d}P}{\mathrm{d}z}\left[a(\delta) - c(\delta)\cdot\left(\frac{r}{R}\right)^2\right], \tag{5.24}$$

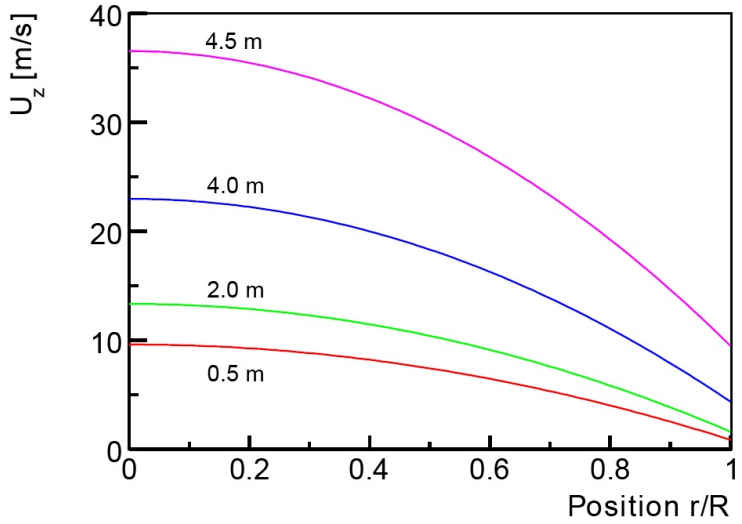

Figure 5.10: **Bulk velocities at different positions**. Velocity profile of several cross sections of the beam tube at different z positions. The bulk velocity increases towards the beam tube ends, but remains smaller than the average thermal velocity of about $300\frac{\mathrm{m}}{\mathrm{s}}$.

where the rarefaction parameter δ is given by

$$\delta = \frac{Rp}{\eta\ v_0}, \tag{5.25}$$

Here, $R = 8.31J \cdot (mol\ K)^{-1}$ is the gaseous constant, p the pressure, η the viscosity and $v_0 = \sqrt{\frac{2RT}{m}}$ the most probable velocity of a molecule with Temperature T and molecular mass m.

The coefficients $a(\delta)$ and $c(\delta)$ can be obtained from the following phenomenological expressions [75]

$$a(\delta) = 0.894 - 0.1048\delta((1 - 0.25\ln\delta)\left[\frac{1+\delta}{1+1.963\delta} + \frac{\delta(\delta+2.036}{2.593+4\delta}\right] \tag{5.26}$$

$$c(\delta) = 0.295 - 0.0536\delta((1 - 0.25\ln\delta)\left[\frac{1+\delta}{1+0.7599\delta} + \frac{\delta^2}{0.07788+4\delta}\right]. \tag{5.27}$$

Density profile

The distribution of the tritium molecules is another important ingredient for the neutrino mass analysis. While it has been shown in Ref. [76] that for a perfectly homogeneous source, the scattering probabilities are independent of the shape of the density distribution, this is no longer true if this homogeneity is not perfectly fulfilled. Therefore, since key experimental parameters like the magnetic and electric fields and the temperature are not perfectly homogeneous, the scattering probabilities need

to be calculated in a position dependent way as well. In this case, knowledge of the number density $n(\vec{r})$ becomes mandatory. Therefore, the KATRIN collaboration in collaboration with the group of Prof. Sharipov[1] who specializes in such calculations, started the development of a gas dynamical model for the source [77, 78, 79, 75]. The solution strategy is briefly discussed here, details can be found in the above references.

Methodology

In general, the calculation strategy depends on the flow regime, which can be characterized either by the Knudsen number Kn, or more commonly by the rarefaction parameter δ introduced in Eq. (5.25) which is inversely proportional to the Knudsen number. One can distinguish two special cases, the hydrodynamical regime with $\delta \gg 1$, where the equations of continuum mechanics (in particular the Navier-Stokes equation) can be applied, and the free molecular flow ($\delta \ll 1$), where intermolecular collisions can be neglected and the molecules move independently of each other. The transitional regime of $\delta \approx 1$, is the most difficult. The intermolecular collisions cannot be neglected, however the equations from continuum mechanics are not valid as well. In this case, the Boltzmann equation

$$\frac{\mathrm{d}f(\vec{r},\vec{v},t)}{\mathrm{d}t} = J^+ - J^-, \tag{5.28}$$

which is a differential equation governing the behavior of the distribution function $f(\vec{r},\vec{v},t)$, needs to be solved. The distribution function describes the number of molecules which can be found in the phase space volume $[\vec{r},\vec{r}+\mathrm{d}^3\vec{r}],[\vec{v},\vec{v}+\mathrm{d}^3\vec{v}]$ at time t. The terms J^+ and J^- describe the gain and loss rate of this phase space volume due to intermolecular collisions. The right hand side of 5.28 is often expressed with the collision integral

$$J(f,f^*) = \int\int\int (f(\vec{v}')f(\vec{v}'_*) - f(\vec{v})f(\vec{v}_*)\omega(\vec{v}_*,\vec{v}'_*,\vec{v},\vec{v}')\mathrm{d}\vec{v}'\mathrm{d}\vec{v}'_*\mathrm{d}\vec{v}_* \tag{5.29}$$

$\omega(\vec{v}_*,\vec{v}'_*,\vec{v},\vec{v}')$ denotes the probability for two molecules with initial velocities $\vec{v}'$ and $\vec{v}'_*$, to end up with the final velocities $\vec{v}$ and $\vec{v}_*$ after a scattering interaction. Since the flow regime in the WGTS ranges from $\delta \approx 20$ near the injection, where the flow is hydrodynamical, to $\delta \approx 10^{-2}$ in the pump ports, which is in the free molecular flow regime. Therefore, the flow regime covers the transition regime and solving the Boltzmann equation (5.28) is required to compute the density profile.

The collision integral depends on the details of the molecular interactions. Its exact solution requires a very large computational effort, so typically simplified expressions are used. For the conditions in the KATRIN source, the S-model [80] is the best choice, since it treats non-isothermal flows correctly. In this model, the collision integral is expressed as

$$J(ff_*) = \frac{p}{n}\left[f_M\left(1+\frac{2}{15}\cdot\frac{m\vec{q}\cdot\vec{V}}{nk^2T^2}\left(\frac{mV^2}{2k_BT}-\frac{5}{2}\right)\right)-f\right] \tag{5.30}$$

where $f_M(\vec{v} = n\left(\frac{m}{2\pi k_BT}\right)^{\frac{3}{2}}\exp\left(-\frac{m}{2\pi k_BT}(\vec{v}-\vec{u})^2\right)$ denotes a local Maxwell Boltzmann distribution, centered around the bulk velocity $\vec{u}(x)$.

[1] Universidade Federal do Paraná, Brazil

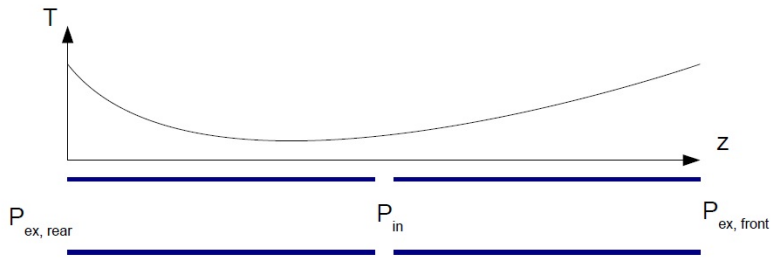

Figure 5.11: **Boundary conditions of the gas dynamics calculation**. The injection and exit pressures in combination with the specification of a temperature profile along the beam tube constitute the necessary input for hte gas dynamics simulation.

Application to the WGTS

In the case of the WGTS, the length of the beam tube L is much larger than its radius r. Therefore, it is advantageous to neglect the radial dimensions and only consider the z dependence of the distribution function, which reduces the problem to only one dimension.

The gas flow along the tube is driven by small gradients of the pressure p or temperature T. However, the mass flow

$$\dot{m} = \pi r^3 \vec{v}_0 \cdot \frac{273.15\ \mathrm{K}}{\sqrt{TT_0}} \left[-G_P(\delta) \frac{\mathrm{d}p}{\mathrm{d}z} + G_T(\delta) \frac{p(z)}{T(z)} \frac{\mathrm{d}T}{\mathrm{d}z} \right] \tag{5.31}$$

has to remain constant along the tube.

The Poiseuille coefficient G_P and the thermal grip coefficient G_T, which depend only on the rarefaction parameter δ, are available in [81]. The coefficients were obtained by linearizing the Boltzmann equation around a Maxwell-Boltzmann distribution, using the small pressure and temperature gradients as perturbation parameters. Solving Eq. (5.31) with these coefficients and the boundary conditions p_{in}, p_{out} and $T(z)$ allows to determine the relationship $z = z(\delta)$, and consequently determines the pressure and density profiles along the tube:

$$p(z) = \frac{T(z)}{T_0} \frac{\eta v_0 \delta(z)}{r} \qquad \text{and} \qquad n(z) = \frac{p(z)}{k_B T(z)} \tag{5.32}$$

While the one-dimensional treatment is in principle sufficient along most of the tube, it cannot correctly treat end effects. Therefore, the injection and the pump port regions require special care. Additionally, the influence of azimuthal temperature variations has been studied in [75]. These fluctuations arise from the fact that most of the heat income of the beam tube is due to radiation, which is isotropic, while the tube is cooled on both sides. The corresponding reports [77, 78, 79, 75] usually treat the WGTS as point symmetric to the injection. However, the routines which have been integrated in Kassiopeia have been modified to allow the computation of the

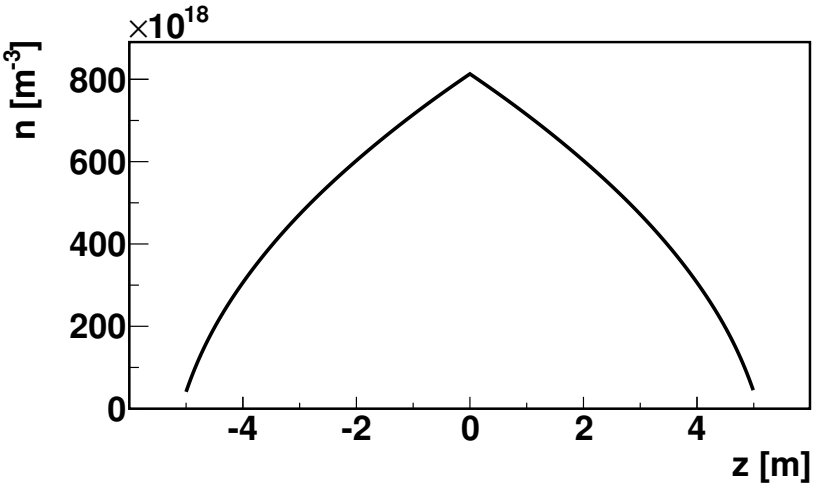

Figure 5.12: **Density profile** inside the WGTS up to the first pump port for an injection pressure of $p_{in} = 3.368 \cdot 10^{-3}$ mbar and an exit pressure of 5% p_{in}.

one dimensional density profile without this assumption. In that case, the injection pressure, the rear and front exit pressure and temperature profile along the complete beam tube have to be specified as boundary conditions as shown in Fig. 5.11. The density profile obtained for typical values of these boundary conditions is then shown in Fig. 5.12.

Additionally, it is possible to obtain an estimation of the three dimensional temperature profile. Based on the study of the influence of azimuthal temperature variations in [75], a series of azimuthal density profiles is available for cross sections of the WGTS for different values of δ. An interpolation method has been implemented which allows to combine these cross sections with the one dimensional profile, giving an estimation of the three dimensional profile. The development of a full three dimensional model focusing on the pump port and injection region has been started recently [82].

Gas composition

The gas composition influences the differential spectrum via the different recoil energies and final state distributions of the tritiated hydrogen isotopologues. As mentioned in Sec. 3.2, the expected gas composition of the tritium provided by the Tritium Laboratory Karlsruhe is at least 90% T_2,with an addition of about 10% DT and fractions of HT. This implies a tritium purity $\epsilon = \frac{N_T}{N_{total}}$ of at least 95%. The gas composition will be continuously monitored with a Laser Raman system (LARA) in the inner tritium loop mentioned previously in Sec. 3.2. The determination of the non-β-active constituents of the gas with LARA also allows to monitor the total number of molecules in the source, an important ingredient to calculate the scattering probabilities. This is of special importance since all other continuously operating devices only monitor the source activity and are therefore sensitive only to the β-active gas content.

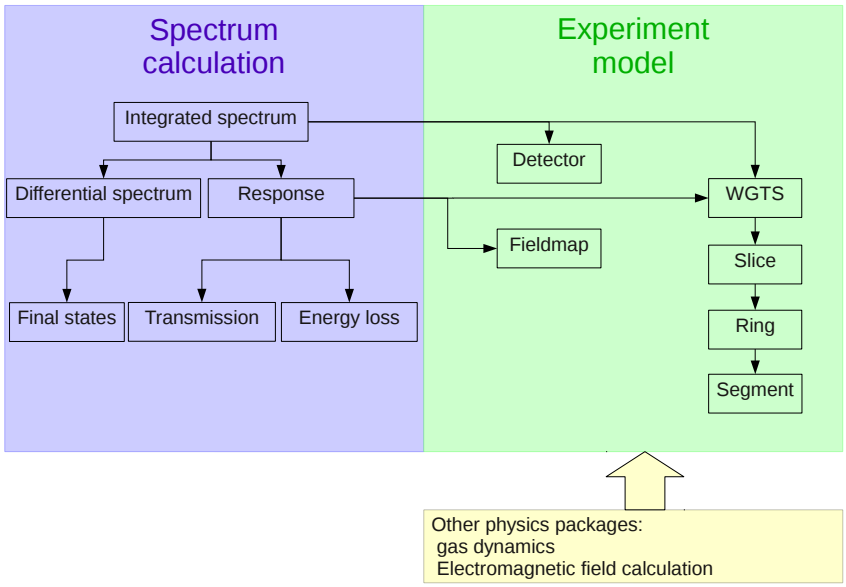

Figure 5.13: **Schematic view of the spectrum calculation software**. The program has two main components, the spectrum calculation itself and the experimental model. All parts of the program allow a large flexibility for the user in the configuring the physics and in choosing the level of detail in which the experiment is modeled.

5.2 The source simulation

The task of the source simulation framework is to unify the different effects described above in a coherent way. Originally developed in [83], it has been extended by implementing additional modifications to the spectrum and completely redesigned as part of this thesis. The redesign focused on increasing the flexibility of the program. The source simulation contains the gas dynamical code discussed above, but its major part is the spectrum calculation module. The layout is shown in Fig. 5.13. As can be seen in this scheme, the program has two main components: The spectrum calculation itself, and a model of the underlying experimental settings which influence the spectrum, including a detailed model of the WGTS, key electromagnetic parameters of the MAC-E filter and detector characteristics such as background and resolution.

5.2.1 The model

The experimental model (the right block of Fig. 5.13) allows to compute the spectra based on localized experimental properties - one of the main features of the spectrum calculation software. This is achieved by dividing the source into a large number of voxels[2]. If the voxels are small enough, one can assume that experimental conditions are constant over one voxel, so each voxel can store the values of the relevant experimental parameters summarized in Tbl. 5.2.

[2] a voxel is a three dimensional analog to a pixel, shortened for 'volumetric pixel'

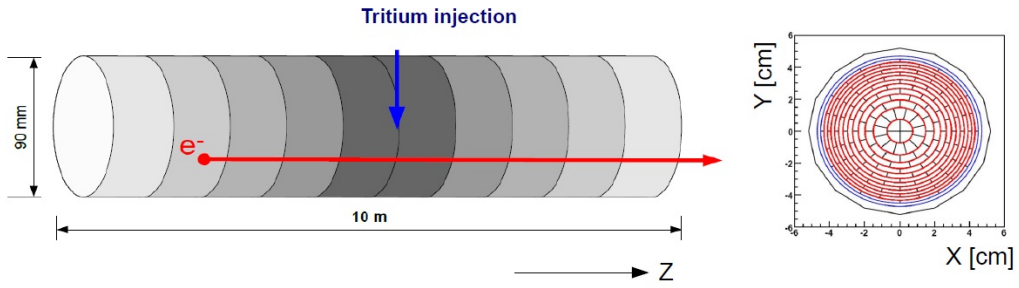

Figure 5.14: **Schematic view of the WGTS voxelization**. The WGTS can be divided into longitudinal segments, a further division in radial and azimuthal direction based on the detector geometry is possible as well. The grey scale symbolizes the tritium content of each slice. Each voxel contains the local conditions influencing the β spectrum. This allows to include the influence of inhomogeneities in the calculation of integrated spectra.

Typically, 1000 slices along the z direction are used to divide the WGTS longitudinally. As shown schematically in Fig. 5.14, each slice can then be further divided into 148 pixels based on the detector geometry. In order to reduce the computing time, the number of slices is usually reduced by combining several voxels into one, after the most critical parameters, the scattering probabilities, have been calculated. The combination procedure therefore takes into account the most critical position dependent influences with higher discretization, while simultaneously reducing the CPU time tremendously.

The rest of the setup has also been discretized: A pixelized version of the magnetic fields in the analysis and B_{max} plane, characterizing the transmission characteristics of the MAC-E filter setup, can also be specified as well as a 2 dimensional specification of the background and efficiencies of the detector. Nevertheless, the model can be configured to be zero-, one- or three dimensional, therefore it offers a large flexibility in terms of the computation time.

Calculating an integrated spectrum consists, as usual, of two phases, the initialization, where preparing calculations are performed, and the actual calculation of a

Table 5.2: Properties of a WGTS voxel (some are redundant and computed from others)

property	property	property
density	temperature	bulk velocity
magnetic field	electric potential	number of tritium molecules
center	upper left corner	upper right corner
area	lower left corner	lower right corner
z position (center)	width	scattering probabilities

spectrum. In the initialization phase, the experimental model is constructed, based on parameters provided by the user: A (voxelized) WGTS, (pixelized) magnetic field strengths in the analysis plane and in the plane with the maximal magnetic field are constructed as well as the detector model, which specifies the efficiency and background (for each detector pixel). After the parameters from Tbl. 5.2 are computed and assigned, where applicable with the help of field/gas dynamics routines, finally the scattering probabilities for every segment are computed according to Eq. (5.18). After this step, the number of voxels can be significantly reduced by averaging over several neighboring voxels. During this averaging voxels are weighted with their respective number of tritium molecules.

5.2.2 Spectrum calculation

The second major part of the software is the spectrum calculation itself, shown in the left part of Fig. 5.13. The organization reflects the fact that the integrated spectrum is a convolution of the differential spectrum $\frac{\mathrm{d}N}{dE}$ and the experimental response $R(E, qU)$ introduced in Sec. 3.1. The defining equations (5.8), (3.4), (3.5) and (3.6) are collected here due to their major importance:

$$\begin{aligned}\frac{\mathrm{d}N}{\mathrm{d}E} &= C \cdot F(Z,E) \cdot K(p,E) f_{rad}(E) \\ &\quad \sum_i P_i \left(E_0 - E_i - E\right) \sqrt{\left(\left(E_0 - E_i - E\right)^2 - m_{\overline{\nu_e}}^2\right)} \\ &\quad \Theta\left(E_0 - E_i - E - m_{\overline{\nu_e}}\right)\end{aligned}$$

$$T(E,qU) = \begin{cases} 0 & E - qU < 0 \\ \frac{1-\sqrt{1-\frac{E-qU}{E}\frac{B_S}{B_A}}}{1+\sqrt{\frac{\Delta E}{E}\frac{B_S}{B_A}}} & 0 \leq E - qU \leq \Delta E \\ 1 & E - qU > \Delta E \end{cases} \tag{5.33}$$

$$R(E,qU) = \int_0^{E/2} T(E-\epsilon, qU) E_{loss}(E,\epsilon) d\epsilon$$

$$N(qU, E_0, m_{\overline{\nu_e}}^2) \propto \int_0^{E_0} \frac{\mathrm{d}N}{dE}(E, E_0, m_{\overline{\nu_e}}^2) R(E,qU) dE.$$

During the computation of an integrated spectrum the experimental model serves as a lookup table for the experimental parameters. By computing an integrated spectrum for each WGTS voxel, the detailed investigation of the influence of these parameters on the spectrum becomes possible. As demonstration of this principle, Fig. 5.15 shows the response function for 10 longitudinal bins. The total integrated spectrum shown in Fig 5.16 for different neutrino masses is then obtained by a sum over all WGTS voxels.

In most cases, several descriptions of the respective quantity are available, e.g.:

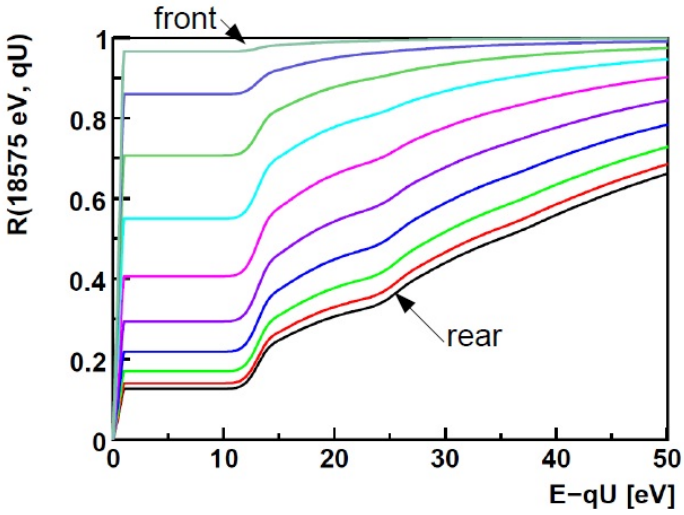

Figure 5.15: **Response function for 10 longitudinal bins of the WGTS**. This figure shows the response function for the 10 longitudinal bins shown in Fig. 5.14. Each bin has a length of 1 m. The topmost teal line corresponds to the bin closest to the detector, while the downmost black curve corresponds to the rearmost bin. Almost all electrons emitted at the detector side with a small excess energy reach the detector, while only about 10% of the electrons emitted at the rear side leave the source unscattered.

- Final states: The most recent and most reliable final state calculation [67, 68] for HeT and HeD is implemented as default. For comparison, also a previous publication [69] is available. The final state distribution in this earlier publication has been computed in 0.1 eV bins only and also does not include rotational excitations of the initial state.

- Differential spectrum: In addition to the standard differential spectrum as given in Eq. (5.8), several versions of differential spectra exist. The first group of these are modified versions of the standard β-spectrum, for example by the inclusion of the Doppler effect or by modifications due to new physics such as sterile neutrinos. Another type of differential spectrum deals with conversion electron spectra, which consist of different mono-energetic lines. It is possible to add several differential spectra together. This is in particular motivated by the Krypton mode of the WGTS, where a small fraction of ^{83m}Kr is added to the T_2 carrier gas, so the differential spectrum is given by a weighted sum of the β spectrum for tritium and a conversion electron spectrum of Krypton.

- Integrated spectrum: In addition to the normal integrated spectrum, it is possible to compute an effective spectrum which only includes the energy loss in the source, but not the transmission function of the main spectrometer. This is defined later in Eq.(5.34) and has two purposes: It allows to start β decay electrons at any point between the source and the pre-spectrometer entrance, since the electron energy remains unchanged on its way to the transport section. This reduces the computation time needed for trajectory calculations. It has also been applied in the investigation of an envisioned improved KATRIN setup, which is discussed in detail in Sec. 6.3.

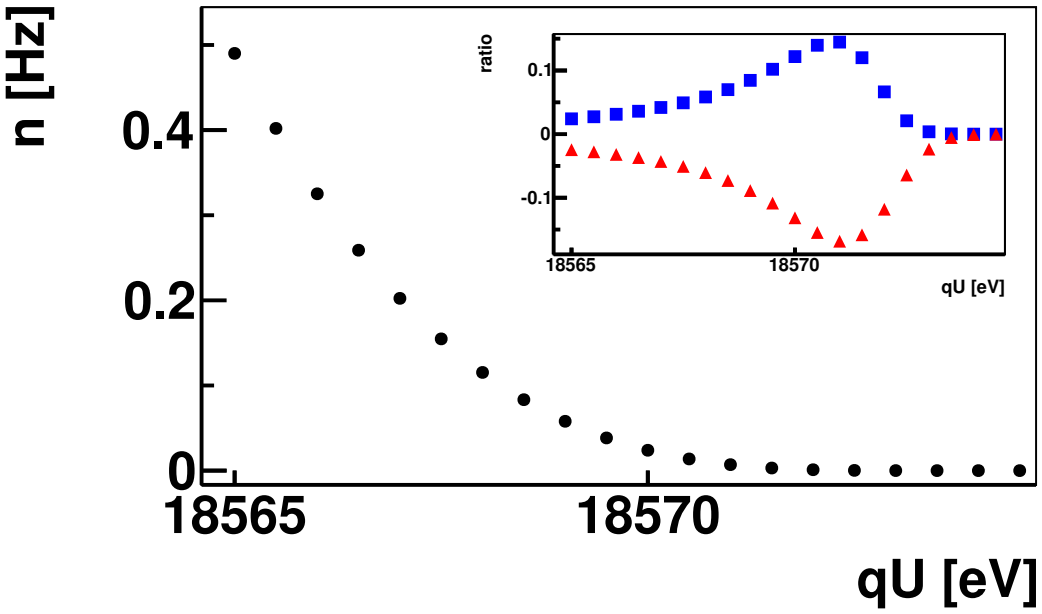

Figure 5.16: **Integrated spectrum**. The large figure shows the rate n of the integrated spectrum for $m^2_{\nu_e} = 0\ \mathrm{eV}^2$ and $E_0 = 18575\ \mathrm{eV}$ without background in dependence of the retarding potential qU. The inlet shows the ratios $\frac{n(m^2_{\nu_e}=0\ \mathrm{eV}^2)-n(m^2_{\nu_e}=1\ \mathrm{eV}^2)}{n(m^2_{\nu_e}=0\ \mathrm{eV}^2)+n_{bg}}$ (red squares) and the unphysical $\frac{n(m^2_{\nu_e}=0\ \mathrm{eV}^2)-n(m^2_{\nu_e}=-1\ \mathrm{eV}^2)}{n(m_{\overline{\nu_e}2}=0\ \mathrm{eV})+n_{bg}}$ (blue triangles), both for $n_{bg} = 10\ \mathrm{mHz}$. As can be seen, the influence of $m^2_{\nu_e}$ is most pronounced a few eV below the endpoint. Although $m^2_{\nu_e} < 0\ \mathrm{eV}^2$ is unphysical, it must be allowed in during the parameter estimation of an analysis, therefore a continuous continuation to negative $m^2_{\nu_e}$ is included in the spectrum calculation software.

5.3 Event Generation

As stated previously, the event generation framework encompasses the simulation of fundamental physical processes like an weak β-decay which can ultimately lead to detector signals. This physical process itself is initiated by an event generator and implies the creation of one or more free particles. In addition to the particles which occur in the process and serve as initial states for tracks, an event is characterized by the position where the process occurred, its time, and an identification number to be able to reconstruct which of several possible processes occurred. This is schematically shown in Fig. 5.17. A typical example for such a process would be the radioactive decay of a specific molecule, e.g. Tritium. Based on the physical motivation for the simulation, the level of detail might be adjusted. For example, a β-decay event will contain only the decay electron but not the daughter ion.

The event generators are therefore a combination of instructions and thus determine the position and time of the event as well as the start parameters of the particles themselves. The start parameters consist of the particle type, specifying properties like mass, charge, spin, etc, and the initial momentum. Instead of the momentum, the kinetic energy and two starting angles can be used to specify the initial state of the particle. The following methods to set these initial properties can be arbitrarily combined:

Position

The event position is independent of the physical process and only based on the simulation geometry. Given a geometry provided, one can select equally distributed events on the surface of that geometry, or inside of the entire volume. For the WGTS, a more complex procedure is implemented, using the density distribution computed with the gas dynamics simulation. In this case, most often only the electrons generated inside the flux tube are of interest, in which case a virtual volume based in the magnetic field configuration is used accordingly.

Time

Timing information is only of interest for DAQ simulations and time of flight simulations. The starting time can also be easily manipulated after a simulation run, simply by adding an offset. Therefore it is typically just set to zero or another constant value. Alternatively, setting the initial time based on a radioactive decay probability and other basic distributions is also possible.

Energy and direction

After both position and time of the event are determined, the actual physical process is simulated. This process determines the type and starting energy of the involved particles and it may or may not determine the starting direction. For example, the β decay of a radioactive molecule always determines the energy of the decay electron, but the direction is isotropic if the decay occurs in a volume, but more complicated in case the decay occurs on a surface. Therefore, the determination o the initial conditions for each particle is split up in three steps: First, the kinetic energy of the particle is determined, based on the underlying physical process alone. Then the direction is determined using two angles. In an optional third step, corrections

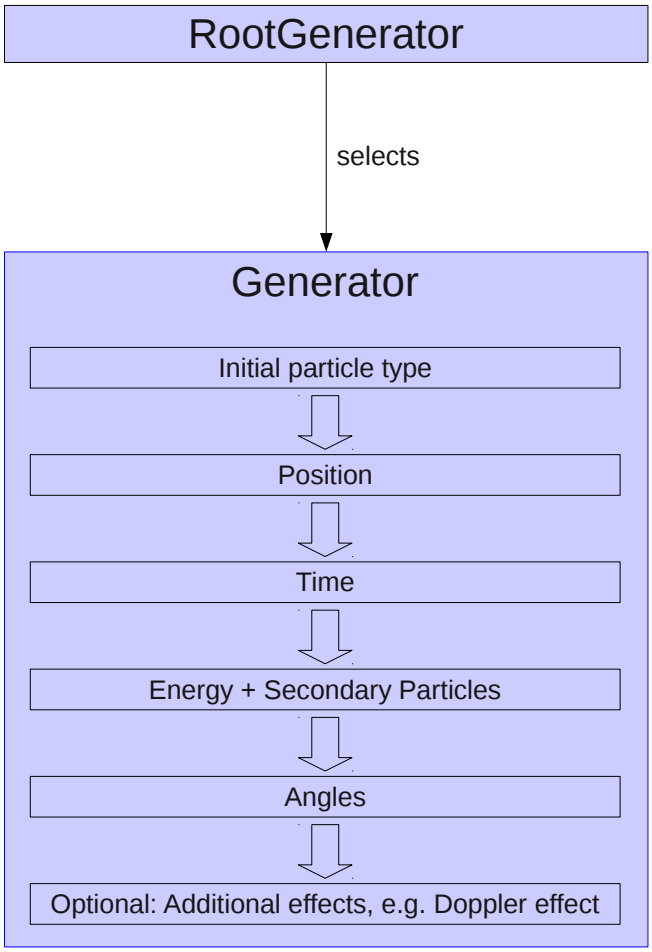

Figure 5.17: **Schematic view of the event generation**. When asked to initialize an event, the root generator selects randomly one of the available generators and asks it to initialize the event. The selected generator then performs the actual initialization and determines the position and time of the event as well as the types and starting properties of the particles in the event.

to the particle properties can be applied. An example for such a correction is the modification of the properties of a decay electron due to the Doppler effect - the decay process is simulated within the rest frame of the mother molecule, and the necessary transformation into the lab frame, which slightly modifies the particles energy and angles, is performed in this last step. The following mechanisms can be used to determine the energy of a particle:

Calibration sources

The most important physics processes relevant for KATRIN apart from the obvious tritium signal electrons are the simulation of calibration and background sources. Calibration sources used in the main KATRIN beam line are either electron guns or radioactive isotopes. Electron guns will be installed in different places of the experimental setup, in particular an angular defined mono-energetic electron gun.

Here, the final electrode design and in particular the precise emission characteristics are not yet known, but models based on the characteristics of prototype designs [84] have been implemented. Additionally, a meta-stable Krypton isotope, ^{83m}Kr, is a very interesting electron emitter for calibration purposes, since it has a prominent conversion electron line at 17.8 keV - relatively close to the tritium endpoint energy of 18.6 keV. The Krypton energy spectrum is available via the spectrum calculation module discussed previously and can be used in the event generation as well.

Background sources

One of the most important background sources in KATRIN is due to the decay of radioactive particles in the main spectrometer, in particular Tritium and Radon, which emanates from the getter pumps [85]. A radioactive decay occurring inside the main spectrometer leads to a high energetic (several keV up to several 100 keV for Radon) electron, which is likely to be trapped. Additionally, secondary electrons like shake-off and/or Auger electrons can occur in the decay process as well. These electrons are trapped in the main spectrometer and thus, despite the ultrahigh vacuum in the spectrometer section, can create a large number of secondary electrons via ionization processes with the rest gas, which can reach the detector. This effect has been observed and further investigated in the pre-spectrometer [85]. As far as the event generator is concerned, there are two ways radioactive decays can be simulated, both of which have been implemented: Only the primary electron can be simulated, or the changes in the electronic configuration of the nuclear remnant can be included, which causes the emission of additional Auger and Shake-off electrons during the event generation. The second background source in the main spectrometer are electrons from the spectrometer vessel and the wire electrodes. Here the detailed emission characteristics is currently under investigation and only basic toy models have been implemented so far.

Tritium generators

There are essentially two ways to generate tritium β-electrons. The first one is obvious, the electrons are simply started at their decay point with an energy sampled from the differential spectrum, Eq. (5.8). In order to save computation time, first a histogrammed differential spectrum is calculated, and then sampled from this histogram. Alternatively, one can compute the effective spectrum $\left(\frac{\mathrm{d}N}{\mathrm{d}E}\right)^{eff}(E)$, where the energy loss in the source is already taken into account:

$$\left(\frac{\mathrm{d}N}{\mathrm{d}E}\right)^{eff}(E) = \int_0^{E_0-E} \frac{\mathrm{d}N}{\mathrm{d}E'}(E+\epsilon)E_{loss}^{WGTS}(\epsilon)\mathrm{d}\epsilon \tag{5.34}$$

In that case, the electrons can be started at a later point of the KATRIN beam line, for example the pre-spectrometer entrance valve. This reduces the amount of necessary trajectory calculations, which can be of computational expensive. Dependent on the configuration of the trajectory calculation, the computation of a single trajectory through the transport section can be of the order of seconds, although significantly faster alternatives are available as well. The effective spectrum is shown together with a differential spectrum without energy loss in Fig. 5.18.

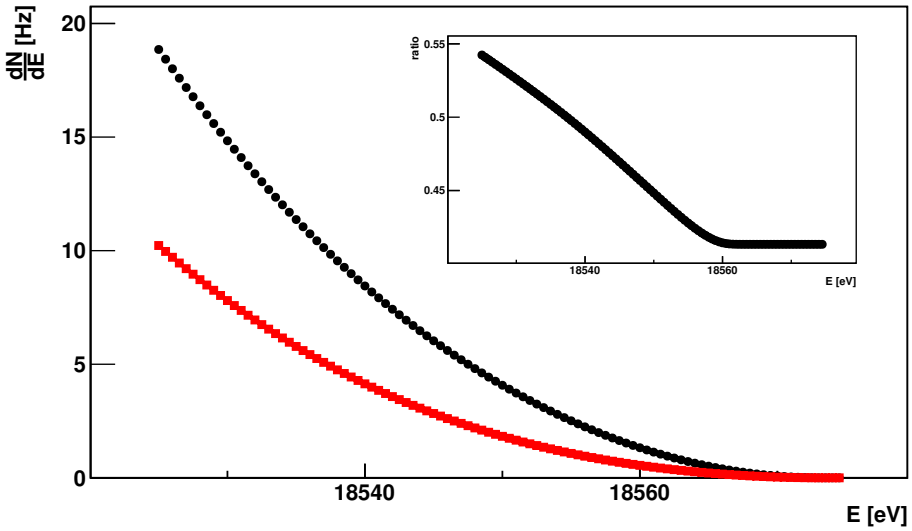

Figure 5.18: **Differential spectrum** with and without energy loss in the source for an endpoint energy of $E_0 = 18575$ eV. The black circles show how the differential spectrum without taking into account energy losses in the source. The red squares show the energy spectrum including these energy losses. Both spectra are normalized to the same source activity (about 10^{11} Bq).

Ion sources

So far, only electrons have been discussed, since they are by far the most important particles in KATRIN. It is of course also possible to compute the trajectories of other particles like ions. This is for example of interest in the differential pumping section DPS2-F, where tritium ions coming from the WGTS have to be prevented from reaching the spectrometer section. This is achieved with an electric dipole system designed in [86].

Direction

In addition to the energy, two starting angles are needed to fully specify the initial state of the particle. In case of a radioactive decay in an arbitrary volume, the starting angles are typically distributed isotropically, which is the first available option. This is no longer true for surface emission, where the emission characteristics is more complicated and based on the surface geometry. In addition to these possibilities to determine the starting direction, the program allows to define a Gaussian angular distribution, as electron guns used for calibration will be able to emit electrons in an angular defined way. A prototype of such an e-gun has been build and investigated in [84].

As a side note, it is also possible to use an ASCII file to fully specify the initial event properties.

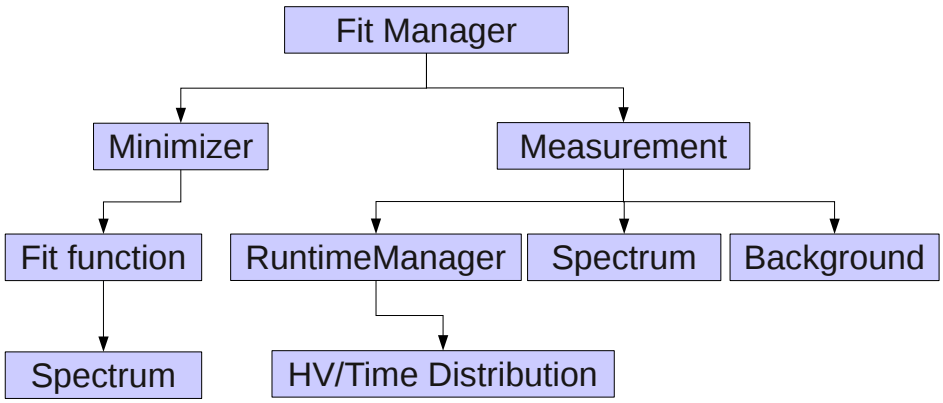

Figure 5.19: **Schematic overview over the analysis software**. For each simulated measurement, the measurement class computes signal and background for the measurement scheme defined in the run manager. This is then analyzed by the Minimizer. The spectrum calculation software is used both during the measurement simulation and the analysis. However, the configuration can be different to investigate systematic errors.

5.4 Sensitivity and Systematic Investigation Software

In order to predict the influence of experimental parameters on the sensitivity of the KATRIN experiment, additional analysis routines are needed to determine statistical and systematic errors. In order to investigate the statistical sensitivity and systematic error of an experimental scenario, a large number (typically 5000) of KATRIN experiments is simulated using the spectrum calculation software described above. The design sensitivity of KATRIN is then determined based on the distribution of fit results. The development and test of these routines constitute the last major contribution to Kassiopeia in this thesis. In addition to the spectrum calculation software, a few more steps are needed to arrive at an experimental count rate and finally a sensitivity. This is shown schematically in Fig. 5.19.

First of all, the experimental background has to be added. Typically, the background is assumed to be constant, however several background models can easily be inserted in the measurement simulation to study the impact of those non-standard, possibly even time dependent, backgrounds on the KATRIN sensitivity. Secondly, multiplying with the measuring time for that particular high voltage determines the expected number of counts N^{exp} in this setting:

$$N^{exp}(U) = t_U \cdot (n_{sig}(U) + n_{bg}(U,t)) \,. \tag{5.35}$$

The actual measured number of counts N^{exp}_{meas} then includes statistical fluctuations of N^{exp} by sampling from a Poissonian distribution with mean value N^{exp}:

$$N^{exp}_{meas}(U) = Poisson(N^{exp}(U)), \tag{5.36}$$

as shown in Fig. 5.20 Finally, the measured rate $n_{meas} = \frac{N_{meas}}{t_U}$ and its statistical error $\sigma_{n_{meas}} = \frac{\sqrt{N_{meas}}}{t_U}$ is computed and stored.

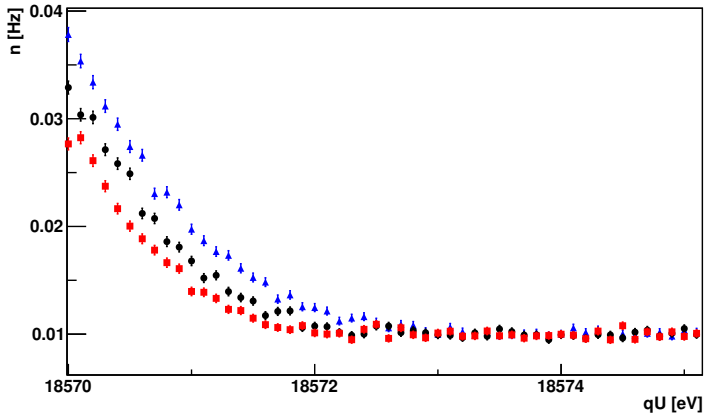

Figure 5.20: **Simulated measurement of the integrated spectrum** for different values of $m^2_{\overline{\nu}_e}$, an endpoint of $E_0 = 18575$ eV and a background rate of 10 mHz. Similar to Fig. 5.16, the red squares correspond to $m^2_{\overline{\nu}_e} = 1$ eV^2, black circles to $m^2_{\overline{\nu}_e} = 0$ eV^2 and the blue triangles to the unphysical $m^2_{\overline{\nu}_e} = -1$ eV^2. The error bars correspond to the statistical errors for one year of measurement time, equally distributed between $qU = 18545$ eV and $qU = 18581$ eV.

This simulated measurement is then used to determine the best estimates for E_0 and $m_{\overline{\nu}_e}$ by performing a χ^2 minimization:

$$\chi^2 = \frac{(n_{meas} - n_{theo})^2}{\sigma^2}. \tag{5.37}$$

where n_{theo} is a 4 parameter fit function

$$n_{theo} = A_{sig} \cdot n_{sig}(E_0, m^2_{\overline{\nu}_e}) + n_{bg}, \tag{5.38}$$

which contains E_0, $m^2_{\overline{\nu}_e}$ and the relative signal strength A_{sig} and the background rate n_{bg} as free parameters.

This procedure is then repeated several thousand times and the results stored in a ROOT [59] file. Based on the repetition of results, one can then extract the statistical sensitivity. Different experimental parameters can be used when simulating the measurement and performing the analysis. In that case, the corresponding systematic error can be read off as deviation from the mean value of the fit parameter of interest (typically the neutrino mass) from its true value, as shown in Fig. 5.21.

5.4.1 Measurement time distribution

The measurement time will not be distributed equally between all high voltage settings. An optimized time distribution shown in Fig. 5.22 increases the sensitivity on the neutrino mass by about a factor of two [25]. This time distribution has been optimized in order to minimize the statistical error on $m^2_{\overline{\nu}_e}$, while keeping the total measurement time constant. These optimizations have been done for different high voltage intervals: The statistical sensitivity of KATRIN decreases with a larger analysis interval, however systematic uncertainties increase due to the increased

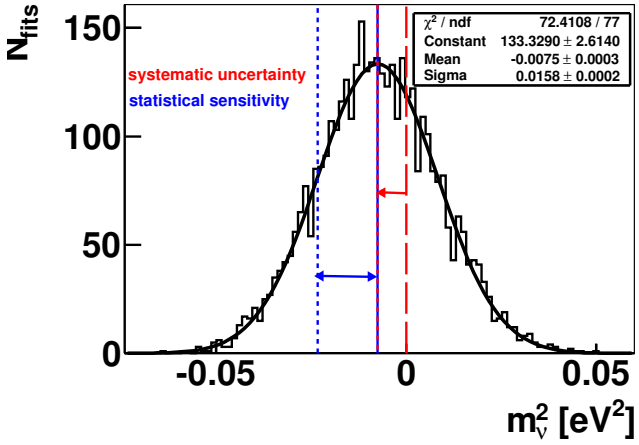

Figure 5.21: **Statistical and systematic errors**. By conducting a series of pseudo-experiments, the distribution of fit results can be used to obtain the statistical sensitivity. By using different parameters during the simulation and analysis of the experiments, the corresponding systematic error is given by the bias of the analysis.

influence of inelastic scattering further away from the endpoint. The most likely optimal compromise between these two contradictory effects seems to be the analysis interval of $[E_0 - 30\text{ eV}, E_0 + 5\text{ eV}]$.

5.4.2 Background models

The estimated design sensitivity of 200 meV (90% C.L.) of the KATRIN experiment stated in [25] is based on the simplest possible background model - a constant background rate, assumed to be 10 mHz. However, experience at the pre-spectrometer significantly improved the understanding of complex background mechanisms, see e.g. [85], which led to the formulation of more realistic background models. Of particular importance is background generated by radioactive decays. The most common radioactive isotopes in the rest gas of the spectrometer section are Radon and Tritium. Since an electron generated by such a decay has a large likelihood to be stored inside the spectrometer, even a single decay electron can generate a large number of secondary electrons. These electrons are more likely to leave the spectrometer and about half of them reach the detector[3]. Measurements at the pre-spectrometer show, that a single nuclear decay causes an increased background rate on the timescale of an hour [85]. It should be noted, that this background has a quite distinctive ring signature, which should allow to identify such background events in the analysis and remove them. However, due to the larger size of the main spectrometer, the background from radioactive decays will increase and many

[3]The other half leaves at the source side. In this case, it has to pass the source at least twice before coming back and has almost certainly (>99%) scattered at least once. In this case it cannot pass the retarding potential again. There is also a small fraction which leaves the spectrometer at the detector side, but outside of the flux tube, so these are not guided to the detector. Therefore, the likelihood for such an electron to be detected is a bit less than 50%.

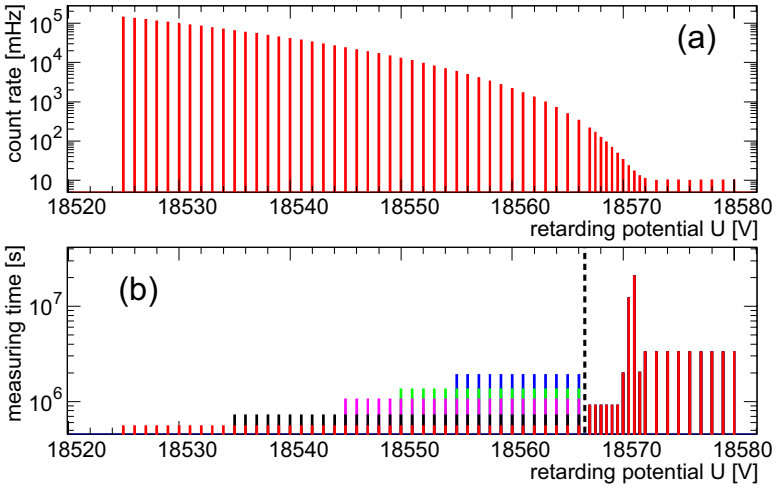

Figure 5.22: **Optimized time distribution** [25]. The top figure shows the simulated count rates at various retarding potentials. The bottom figure shows optimized measurement time distributions for different measurement intervals below the endpoint, ranging from $E_0 - 50$ eV to $E_0 - 20$ eV. The time distribution above the dotted line at 18568 eV is independent of the analysis interval while the remaining measurement time is distributed equally on the lower voltages.

of these rings will overlap and therefore the feasibility and efficiency of such a filter is not yet known. A "worst case" analysis with this software, which estimates this background based on measurements at the pre-spectrometer and simulations of the main spectrometer, but performs the analysis without any filtering using a constant background model, is ongoing [56].

5.4.3 Spectrum interpolation

Since in a full three dimensional configuration, the spectrum calculation requires a lot of computation time[4], an interpolation method has been developed. In principle, the signal rate given by Eq. 3.6 depends on three parameters, U, E_0, m_ν^2. However, in good approximation, only the difference $y = E_0 - U$ matters, the absolute value is not important. Further introducing $x = E - U$, one can rewrite Eq.(3.6) to:

$$N(y, m_{\overline{\nu}_e}^2) = \int_0^y \frac{\mathrm{d}\tilde{N}}{\mathrm{d}E}\left(y - x, m_{\overline{\nu}_e}^2\right) \tilde{R}(x)\mathrm{d}x \tag{5.39}$$

This allows to reduce the dimension of the interpolation from three to two and drastically reduces the time needed to compute the interpolation grid, however requires to ignore the dependence on the absolute kinetic energy of both the differential spec-

[4] about an hour per high voltage

trum and the response function and replace all these dependencies by a fixed energy E_{scale}. In this case, the approximated differential spectrum $\frac{\mathrm{d}\tilde{N}}{\mathrm{d}E}$ is given by:

$$\frac{\mathrm{d}\tilde{N}}{\mathrm{d}E} = C \cdot F(Z, E_{scale}) \cdot K(p, E_{scale}) \sum_i P_i \left(y - x - E_i\right) \sqrt{\left(\left(y - x - E_i\right)^2 - m^2_{\overline{\nu}_e}\right)} \Theta\left(y - x - E_i - m_{\overline{\nu}_e}\right). \quad (5.40)$$

The only dependence on the kinetic energy of the electron in the response function is mostly in the transmission function, the energy dependence of the energy loss function can be neglected. The transmission function is approximated as:

$$\tilde{T}(x) = \begin{cases} 0 & x < 0 \\ \frac{1-\sqrt{1-\frac{x}{E_{scale}}\frac{B_S}{B_A}}}{1+\sqrt{\frac{\Delta E}{E_{scale}}\frac{B_S}{B_A}}} & 0 \leq x \leq \Delta E \\ 1 & x > \Delta E \end{cases} \quad (5.41)$$

The difference between the count rates obtained with exact formula and the approximation is shown in Fig. 5.23. As can be seen, the approximation changes the rates of the integrated spectrum by a few per cent, therefore it must not be applied to real data. However if used consistently throughout a simulated KATRIN experiment, it will give a sensitivity, which will only be a few per cent incorrect[5] with respect to the exact computation, but significantly faster − once the necessary grids are calculated, any further analysis can be performed on a typical laptop in less than an hour, while the direct investigations of a full three-dimensional WGTS model requires access to a computing center. Therefore, the interpolation is extremely useful for a first investigation of the parameter space of interest. Afterwards, the most interesting scenarios can be investigated using the exact expressions, if necessary. Fig. 5.23 shows the interpolation error for a moderate grid spacing.

The CPU time can be further reduced by combining a one-dimensional and a two-dimensional interpolation: The influence of $m^2_{\overline{\nu}_e}$ on the spectral shape is also small. Using the identity

$$n_{sig}(y, m^2_{\overline{\nu}_e}) = n_{sig}(y, 0) + \Delta N_{sig}(y, m^2_{\overline{\nu}_e}) \quad (5.42)$$

one can compute a finely binned one-dimensional grid for $n_{sig}(y, 0)$, together with a more coarsely two-dimensional binned grid, which contains the difference between the rates for zero and non-zero neutrino mass $\Delta N_{sig}(y, m^2_{\overline{\nu}_e}) = n_{sig}(y, m^2_{\overline{\nu}_e}) - n_{sig}(y, 0)$. This is schematically depicted in Fig. 5.24. During the fit, the count rate is computed with a combined one- and two-dimensional interpolation based on Eq. (5.42). The default method is a linear interpolation, alternatively a cubic/bi cubic spline method can be used, which is slightly slower. Fig. 5.23 shows the interpolation error for a moderate grid spacing, together with the error of the approximation formula.

[5] it will actually be slightly worse, because the approximation is systematically too low

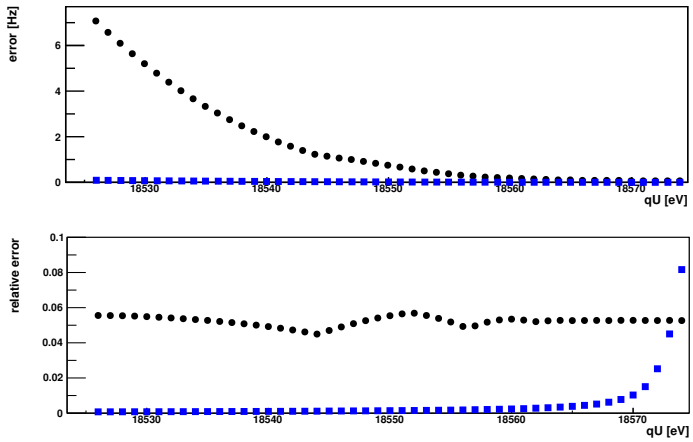

Figure 5.23: **Absolute and relative errors of the interpolation method**. The top figure shows the absolute error due to the approximative formula Eq.(5.39) (black circles) and the interpolation itself (blue squares), the lower plot the relative errors in the same color scheme. The approximation is correct to a few %. For the interpolation a one dimensional grid spacing of 0.01 eV and a 2 dimensional grid spacing of 0.1 eV $\times$ 0.01 eV^2($y \times m^2_{\overline{\nu}_e}$) has been used here. The rates where always calculated in the middle between grid points, where the interpolation error is maximal. For this binning, the interpolation error is almost independent of $m^2_{\overline{\nu}_e}$ and negligible in comparison to the error due to the approximation. The only exception are a few points at very high retarding potentials. However these are already in a region, where the measurement is background dominated.

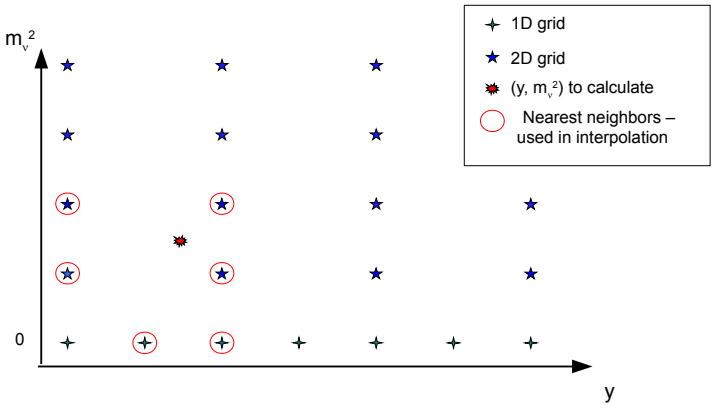

Figure 5.24: **Schematic layout of the interpolation grid**. Due to the weak dependence of the count rate on $m^2_{\overline{\nu}_e}$, a combination of a one-dimensional grid and a two dimensional grid is used. The one-dimensional grid stores the count rate for $m^2_{\overline{\nu}_e} = 0$ eV^2 only in dependence on the distance from the endpoint $y = E_0 - U$ with a smaller grid spacing than the two-dimensional grid, where the difference $\Delta N_{sig}(y, m^2_{\overline{\nu}_e}) = n_{sig}(y, m^2_{\overline{\nu}_e}) - n_{sig}(y, 0)$ is stored. This reduces the grid computing time.

6. Application and Results

This final chapter contains selected analyses performed with Kassiopeia during this thesis. In all cases, the spectrum calculation and the analysis module of Kassiopeia described in the previous chapter were used to investigate the sensitivity of the KATRIN experiment. The first section 6.1 shows that the analysis is unbiased and correctly reproduces input values and statistical errors from previous studies. In Sec. 6.2, the impact of the gas composition and the beam tube temperature on the KATRIN sensitivity is discussed in view of recent results from the Laser Raman system and the WGTS demonstrator. Finally, an envisioned KATRIN upgrade will be introduced in Sec. 6.3.

6.1 Validation of the simulation and analysis software

A simulation and analysis code usually needs to undergo validation tests to ensure its reliability. In this case, the validation procedure consists of two parts, the validation of the spectrum calculation itself, described in Sec. 6.1.1, and the verification of the analysis code in Sec. 6.1.2.

6.1.1 Verification of the spectrum calculation code

The most important test of the spectrum calculation software is the comparison with earlier calculations. Provided the same conditions are used, the obtained results should be identical (within numerical accuracy). Since all previous codes did not include any spatial inhomogeneities, this means that the voxelization described in Sec. 5.2.1 has to be switched off for such a comparison. On the other hand, including the voxelization allows to use a more realistic model of the experimental conditions in KATRIN, and consequently the results will differ slightly from earlier calculations.

Table 6.1 shows a comparison of the rates for the integrated spectrum between previous calculation methods [87], and two configurations of the spectrum calculation module: In the middle column, the spectrum calculation module was configured as

close as possible to [87]: The voxelization was switched off and only a zero dimensional model with the same parameters to describe the experimental setup as in [87] and [25] was used. In this case, the agreement is better than 1%; the remaining difference is due to the different descriptions of the final state distribution and different numerical integration routines. The right column shows the rates obtained with voxelization switched on. Here, the current best estimates of the experimental conditions were used, which differ slightly from the conditions in the other two columns. The most important differences are the addition of a non-zero exit pressure and a change of the source temperature from 27 K to 29 K. Also the actual shape of the magnetic field was used. Due to these differences, no exact agreement can be expected. In particular, due to the non-zero exit pressure, the column density and therefore the total source activity is slightly increased with respect to the other two cases. Therefore the rates are systematically increased by a few %.

Extensive more low level tests of all program components described in Sec. 5.2 have been performed successfully as well, but are not reported here. This includes, for example, tests of numerical integration routines using integrals which can be solved analytically, comparisons of response function and differential spectrum with earlier calculations, etc.

6.1.2 Verification of the analysis code

The next step in the verification procedure is the test of the analysis code. Any reliable analysis procedure must pass the following tests:

1. The analysis should be unbiased in the sense that the analysis of a "MC-experiment" reproduces the input values within errors.
2. The fit should describe the data, which in this case implies that the χ^2 distribution of the fit results must look as expected.
3. The analysis code also needs to reproduce the statistical sensitivity given in [25] for the same experimental parameters.

The validation tests outlined above can be done in parallel: A series of 5000 simulated KATRIN experiments is performed and analyzed with the analysis procedure

Table 6.1: Comparison of integrated spectrum rates

	K. Eitel [87]	this work	this work (voxelized)
$E_0 - qU$	Rate [Hz]	Rate[Hz]	Rate[Hz]
10	0.50	0.50	0.505
15	2.15	2.17	2.20
20	5.84	5.89	5.97
25	12.61	12.68	12.84
30	23.68	23.72	24.04
40	64.2	64.2	65.08
50	140.9	140.8	142.68

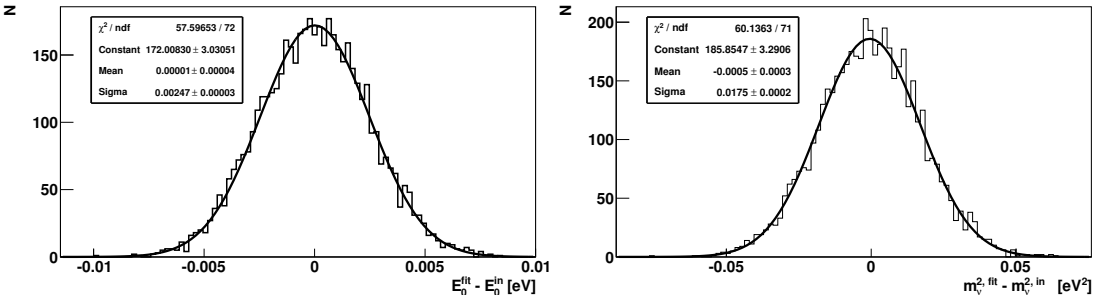

Figure 6.1: **Distribution of fit results** for E_0 (left) and $m^2_{\overline{\nu}_e}$ (right), together with a Gaussian fit. The analyzed interval was $[E_0 - 30\text{ eV}, E_0 + 5\text{ eV}]$, using the optimized measurement time distribution shown in Fig. 5.22. Since the mean values of the fitted Gaussians are compatible with zero, the fit is not biased. The statistical sensitivity of the KATRIN experiment is 2.5 meV for E_0, and 0.0175 eV^2 for $m^2_{\overline{\nu}_e}$ for this analysis interval.

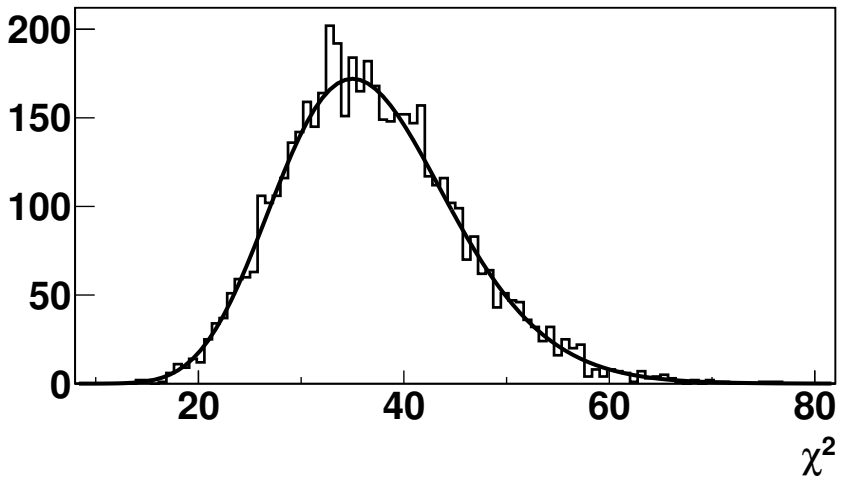

Figure 6.2: **χ^2 distribution of an analysis of 5000 simulated KATRIN experiments**. This distribution is for an measurement interval of $[E_0 - 30\text{ eV}, E_0 + 5\text{ eV}]$. Since close to the endpoint the difference between two measured voltages is only 0.5 V, whereas it is 1 V for most of total measurement interval, 41 different high voltage setting would be measured. Since the fit consists of 4 fit parameters, it has $37 = 41 - 4$ degrees of freedom. The χ^2 distribution follows perfectly the expected χ^2 distribution for 37 degrees of freedom (black curve) and the mean value of χ^2 is 37.07.

outlined in Sec. 5.4. The results of each fit and the corresponding χ^2 value can then be used to determine the outcome of these tests.

1. The distribution of these fit results, which is shown in Fig. 6.1 for a typical configuration, then determines both a possible bias and the statistical sensitivity. As is evident from Fig. 6.1 the first check is fulfilled.

2. The χ^2 distribution is also available from these fits as a quality check. As shown in Fig. 6.2 for the same configuration as above, it follows exactly the expected behavior, so the second requirement is also fulfilled.

3. Repeating the procedure outlined above for different analysis intervals results in Fig. 6.3 and concludes the validation procedure. As can be seen, the analysis reproduces the sensitivity from [25] within the statistical errors of the fit results.

It should be noted that for the interpolation method discussed in detail in Sec. 5.4.3, the reproduction of the design report sensitivity fails to a certain extend. The reason for that is that the approximation Eq. (5.40) computes systematically lower rates than the exact formula. In this case, the sensitivity estimated with the interpolation method is slightly worse than the exact method. For example, the statistical sensitivity obtained with the interpolation method is only

$$\sigma^2_{m^2_{\overline{\nu}_e}} = 0.019 \text{ eV}^2, \tag{6.1}$$

instead of $\sigma^2_{m^2_{\overline{\nu}_e}} = 0.0175 \text{ eV}^2$, for the reference measurement interval of $[E_0 - 30 \text{ eV}, E_0 + 5 \text{ eV}]$.

The analysis of previous experiments has also shown that the results for E_0 and $m^2_{\overline{\nu}_e}$ are strongly correlated, see e.g. [88]. This is also reproduced here as shown in Fig. 6.4. All the tests outlined above show that the analysis procedure works and can be used in investigations of systematic uncertainties.

6.2 Systematic errors associated with the source

An experiment reaches its optimal sensitivity when statistical and systematical errors are about of equal size. Therefore, understanding and reducing systematic errors is extremely important. The most important contributions to the systematic error for the neutrino mass determination in the KATRIN experiment are listed in Tbl. 6.2. Most of these systematic errors are associated with the WGTS. The understanding of energy losses, most notably the determination of the energy loss function, together with the knowledge of the final state distribution and the monitoring of the column density constitute the major systematic uncertainty. The energy loss of electrons in tritium will be measured with the KATRIN setup itself with increased precision, but so far the situation is unchanged with the respect to the KATRIN design report [25]. The situation is different for the other two main contributions to the systematic error, where new information has become available. This triggered a series of systematic investigations during this thesis, which are reported in the following.

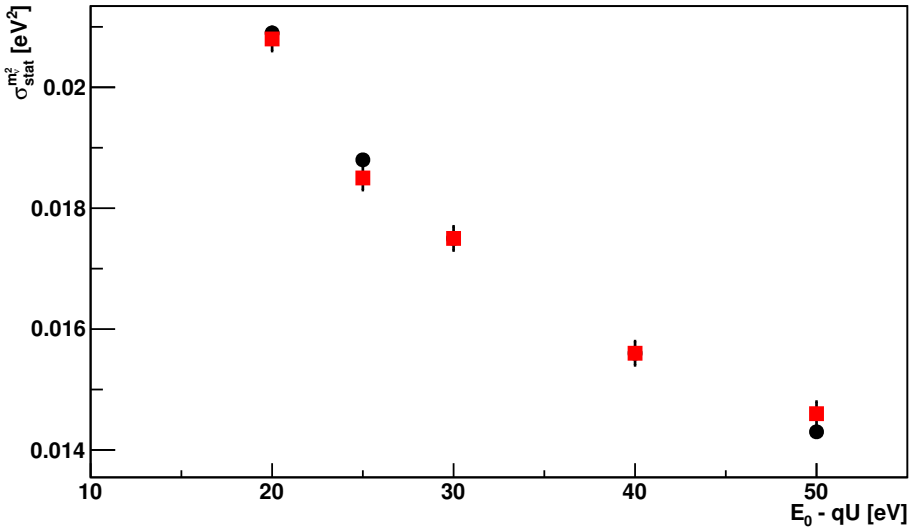

Figure 6.3: **Comparison of the statistical sensitivity** on m^2_ν between [25] and the analysis package from this thesis. The voxelization was switched off, so that identical experimental conditions could be used. The statistical uncertainties 30 eV below the endpoint coincide within visual precision. The error bars correspond to the statistical error of a Gaussian fit to the fit results.

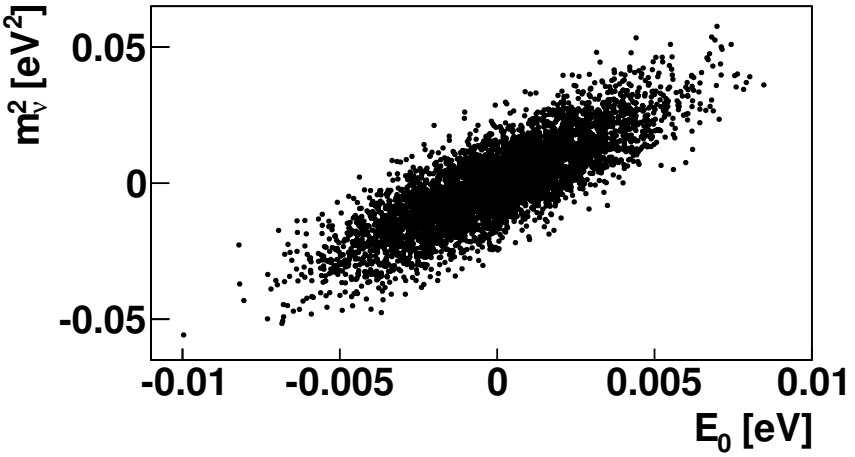

Figure 6.4: **Correlation between fit parameters**. The fitted $m^2_{\overline{\nu}_e}$ and E_0 are known to be strongly correlated [88].

Table 6.2: **Important systematic uncertainties on $m^2_{\overline{\nu}_e}$** [25].

source of systematic shift	systematic shift $\sigma_{syst}[10^{-3}\ \mathrm{eV}^2]$
description of final states	< 6
unfolding the energy loss function	$<$ 2-6
monitoring of ρ_d [1]	$< \sqrt{5} \cdot 0.65$
HV variations	<5
magnetic field variations in WGTS	< 2

[1] requires the relative stability of the beam tube temperature, the injection pressure, the tritium purity and the source activity to within 10^{-3} and an stability of the exit pressure to within 6%.

6.2.1 The Final State Distribution

As previously discussed in Sec. 5.1.1, the decay products HeT and HeD take away recoil energy as well energy stored in internal excitations. In particular, rotational and vibrational excitations take away around 2 eV (including recoil), which causes a modification close to the endpoint of the spectrum, where the sensitivity to the neutrino mass is most pronounced. Electronic excitations start playing a role only at about 20 eV below the endpoint and are therefore of secondary importance.

In addition to the recalculation of the final state distribution in [67, 68] mentioned in Sec. 5.1.1, significant progress has also been made on the monitoring side, in particular the LAser RAman system LARA, which monitors the gas composition is fully operational, and the temperature profile along the beam tube has been determined by the WGTS demonstrator test setup. Both of these measurements influence the description of the final states as discussed below. In order to obtain a rough estimate of the influence of temperature and gas composition on the final state distribution, a simple toy model is introduced first. This provides a useful simple cross check of the full analysis chain.

A Toy Model for the Final State Distribution

The final state distribution as depicted in Fig. 5.3 shows that there are notable differences between the rotational and vibrational states of HeT and HeD. However, after the Doppler effect is applied, the strong bin-to-bin variations are smeared out. As shown in Fig. 6.5 the distribution of rotational and vibrational excited states is qualitatively described by a Gaussian. Varying the width σ of this Gaussian and investigating the effect on the neutrino mass obtained as fit result led to the conclusion [25] that the width needs to be known to 1% in order to arrive at an acceptable systematic error of $6 \cdot 10^{-3}$ eV (cf. Tbl. 6.2). This triggered the recalculation of the final state distribution in a binning of 0.01 eV in [67] mentioned earlier. In this toy model, the width of the Gaussian approximation is important, but the position of the peak is not, since the differential spectrum (Eq. (5.8)) only depends on the difference between the endpoint E_0 and the final state energy E_f. Therefore a shift of the mean value, which corresponds to a shift of all (rovib) final states, would be absorbed in the fitted endpoint value.

The final state distribution is obtained by a weighted sum of the final state distributions of the tritiated hydrogen isotopologues T_2, DT and HT. The weights are given

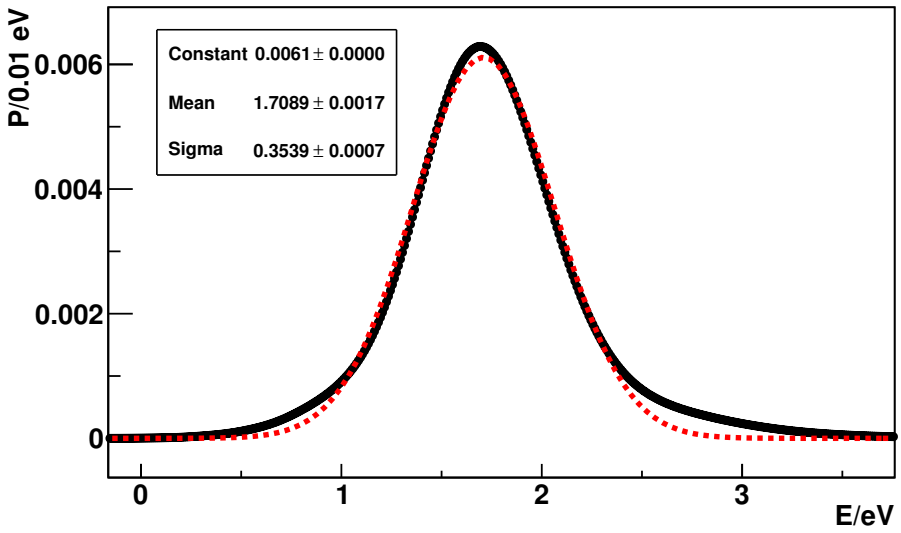

Figure 6.5: **Final state distribution** including the Doppler effect as shown in Fig. 5.4, together with a Gaussian fit (red dashed line). The mean value of the Gaussian is 1.7 eV, the width 0.35 eV.

by the gas composition. Additionally, the effective final state distribution including the Doppler effect is also influenced by the beam tube temperature. Therefore, uncertainties in either parameter contribute not only to the source activity, but to the systematic error of the final state distribution as well. Specifically, the systematic error associated with the final state distribution is given by the quadratic sum of the different contributions:

$$\sigma^{FSD}_{m^2_\nu} = \sqrt{\left(\sigma^{desc}_{m^2_\nu}\right)^2 + \left(\sigma^{\epsilon}_{m^2_\nu}\right)^2 + \left(\sigma^{T}_{m^2_\nu}\right)^2}. \tag{6.2}$$

These influences are examined in more detail in the following, starting with the gas composition measured with the Laser Raman system LARA.

6.2.2 Implication of LARA measurements for KATRIN

The Laser Raman system LARA mentioned in Sec. 3.2 as part of the inner loop is used to monitor the gas composition. This has a two-fold influence on the integrated spectrum measured in KATRIN. The precision, i.e. the sensitivity to changes to the tritium composition, is important to monitor the stability of the source since all other continuously monitoring devices measure the total activity. An additional determination of the gas mixture allows to disentangle changes to the total amount of gas (including non-β-active isotopes) and changes to the amount of tritium in the source. Non-β-active molecules need to be taken into account, since they contribute to the probability for the electron to scatter in the source and thus change the energy loss function. Changing the amount of tritium additionally changes the activity of the source and therefore directly the count rate at the detector. It is even possible that the activity remains constant if both the tritium mixture and the total gas content vary in opposite directions. For this purpose, a relative measurement is sufficient since only changes have to be discovered. Investigations during the design

phase of KATRIN lead to the specification of a precision of 10^{-3} in 250 s. The LARA system already has exceeded this precision using test samples and foresees to reach a precision of 10^{-3} below 100 s under KATRIN conditions, which more than fulfills the KATRIN requirement [25].

However, as pointed out in Sec. 5.2, the tritium composition also modifies the β-decay spectrum itself, because both the recoil energy and the final state distribution depend on the isotopologue. In this case, monitoring the changes to the gas composition is no longer sufficient, the measurement must determine the gas composition − it must not only be precise, but must also be accurate[1]. Since no requirement for the accuracy of LARA has been specified previously and the LARA group is currently working on the calibration of the LARA system, this effect is further investigated in [89] and the following, to ensure the LARA calibration does not add a significant additional contribution to the systematic error from the final state distribution.

Qualitative estimation

In order to obtain a rough estimation of the size of the effect, one can use the toy model discussed in the previous section. After the energy smearing due to Doppler effect is taken into account, all the bin-to-bin variations in the original distributions is smeared out and the final state distributions of HeT and HeD look quite similar. However, a small difference in the width of the corresponding Gaussian fit remains ($\sigma_{HeT} = 0.355$ eV, $\sigma_{HeD} = 0.344$ eV). Considering only the most abundant hydrogen molecules, T_2 and DT with their respective number densities n_{T_2} and n_{DT} and ignoring possible small contaminations with other hydrogen isotopologues, one can parameterize the gas composition with just one parameter, the purity ϵ

$$\epsilon = \frac{n_{T_2} + 0.5 n_{DT}}{n_{T_2} + n_{DT}}. \tag{6.3}$$

By computing the final state distributions for different mixtures of HeT and HeD and fitting each with a Gaussian, one can make use of the fact that with such a toy model a change of 0.01% for the width is critical [25], corresponding to a systematic error of $6 \cdot 10^{-3}$ eV. The width of these Gaussians is shown in Fig. 6.6 for several mixtures. With this simple approach, one can estimate that the systematic error due to the determination of the purity ϵ would be as important as $\sigma^{desc}_{m^2_\nu}$, if ϵ would be incorrect by about 15% with respect to the total amount of tritium in the source. However, since this has not been taken into account in the original error budget of Tbl. 6.2, the contribution of the LARA calibration on $\sigma^{syst}_{m^2_\nu}$ should be significantly smaller than $\sigma^{desc}_{m^2_\nu}$. Requiring $\sigma^{\epsilon}_{m^2_\nu} \approx 0.6 \cdot 10^{-3}$ eV $= 0.1 \cdot \sigma^{desc}_{m^2_\nu}$ indicates that the DT fraction needs to be accurate to about 2% of the total material content. This in turn indicates that the calibration of the LARA system has to ensure an accuracy of $\frac{\sigma_{n_{DT}}}{n_{DT}} < 10 - 15\%$.

Results and implications of the detailed simulation

While the estimation above indicates a much weaker requirement for the accuracy of the LARA system in comparison to the required precision, it is mandatory to

[1] see App. A.1 for the definition of precision and accuracy

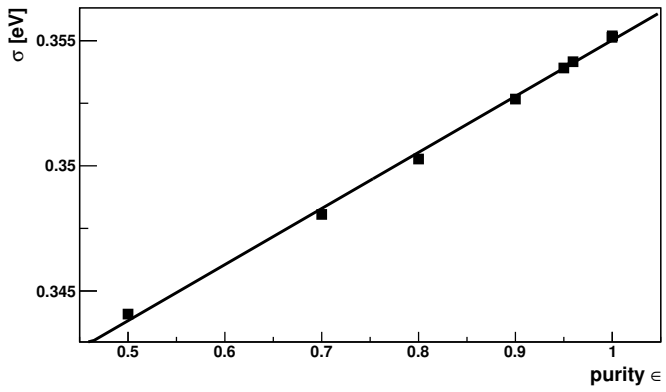

Figure 6.6: **Variation of the width of the final state distribution for different tritium compositions**. In all cases, the final state distribution for the respective mixture was fitted with a Gaussian distribution. According to [25], a change of the width of about 1%, or $0.0035eV$ would constitute a significant systematic error. From the slope of the linear fit σ_{FSD}^{Gaus} [eV] $= 0.3326(4) + 0.0224(4)\epsilon$, one can determine this critical value for the DT content, where the complete systematic error of the final state description would be due to the calibration of the LARA system, to $\frac{0.0035}{0.0224} \approx 0.15$. However, the purity should be determined significantly better than that, so that this additional contribution to the systematic error budget is small enough to be neglected.

crosscheck this with a more detailed investigation, since the Gaussian toy model does not describe the final state distribution quantitatively. The results of this simulation are reported in [89] and briefly summarized here. In this detailed simulation, the tritium mixture used in the calculation of simulated KATRIN spectra contained an slightly different tritium purity, $\epsilon' = \epsilon_{true} + \Delta\epsilon$, while the analysis was performed with a fixed tritium purity of $\epsilon_{true} = 95\%$, corresponding to a mixture of 90% T_2 and 10% DT. The results shown in Fig. 6.7 agree reasonably well with the toy model, indicating $\sigma_{m_\nu^2}^{desc} = \sigma_{m_\nu^2}^{\epsilon}$ at $\Delta\epsilon \approx 10\%$.

In order to avoid an additional contribution to the systematic error associated with the final state description, the systematic error from the LARA calibration should not contribute significantly to the overall uncertainty of the final state description of $6 \cdot 10^{-3}$ eV. The LARA group is confident that a relative accuracy for each species of 5% to 10% can be reached [89]. This implies in this simple two-species model with 90% T_2 and 10% DT, that the purity needs to be accurate to 1%. For a LARA calibration of 10% accuracy, the corresponding contribution of the systematic error would then be about $0.6 \cdot 10^{-3}$ eV, which fulfills this requirement according to both the toy model and the full simulation. Due to the high purity of the tritium gas, even an accuracy as low as 50% would determine the DT fraction incorrectly by only 5% with respect to the total amount of tritium in the source. This would correspond to an increase of the systematic error for the final state distribution by about 8%, which would still be barely acceptable.

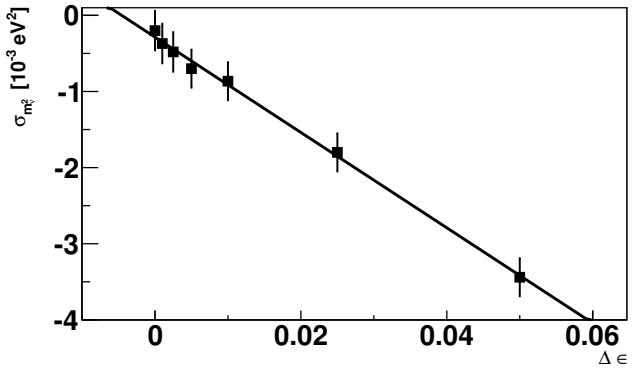

Figure 6.7: **Systematic error on m_ν^2 for different unrecognized DT contaminations** $\Delta\epsilon$. In this case, the full analysis chain was used: 4000 simulated KATRIN measurements were analyzed with a different tritium composition than used in the simulated measurement. The linear fit function is given by $\sigma^{\epsilon}_{m^2_\nu}[10^{-3}\ \mathrm{eV}^2 = -0.29(12) - 63(6)\Delta\epsilon$. The results are similar to the toy model, implying $\sigma^{desc}_{m^2_\nu} = \sigma^{\epsilon}_{m^2_\nu}$ for $\Delta\epsilon = \frac{6}{63} = 9.5\%$.

6.2.3 Implication of the Demonstrator Measurements

In addition to the Laser Raman system, which is already operational, a second important test experiment is ongoing. The WGTS demonstrator test setup is used to investigate the performance of the WGTS cooling system. The most important result of the demonstrator is that the temperature stability of 30 mK per hour which is required for the WGTS can not only be reached, but even be exceeded. However, there are also important open issues:

- The temperature profile measured with the demonstrator is inhomogeneous. How would this affect the density distribution in the source and ultimately the KATRIN systematical error, if the WGTS temperature profile would be similar?

- One possible remedy would be to "turn the WGTS tube around", so that only the rearmost electrons, which exhibit a larger scattering probability, would experience this temperature increase.

- The mean temperature is important, since it effects the density distribution $\rho(z)$ and the differential spectrum due to the Doppler effect. These effects are small, but no specification exists with respect to the accuracy of the temperature, only for its precision. The mean temperature also influences the throughput through the WGTS and the column density, but these quantities can be measured and monitored directly, so it is not necessary to rely on the gas dynamics simulation to compute them from the thermodynamical boundary conditions.

These issues will be discussed in the following.

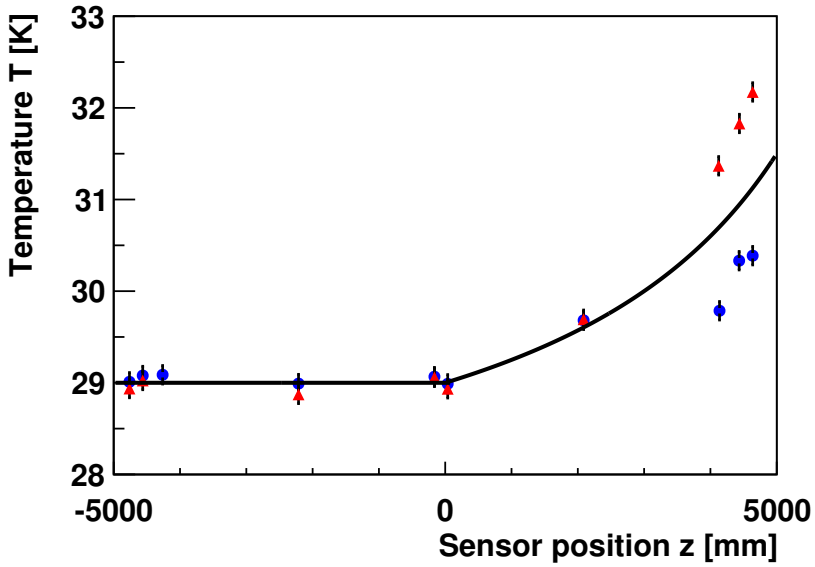

Figure 6.8: **Temperature profile with an analytic descriptions**. This figure shows the temperature profile measured with the PT500 temperature sensor of the WGTS demonstrator, as already shown in Fig. 5.9, together with an empirical analytic description, Eq. (6.4).

Influence of a non uniform temperature distribution

As outlined in Sec. 5.1.3, the temperature profile along the beam tube as measured with the WGTS demonstrator is inhomogeneous and has a strong increase towards the front side by about 3 K. This increase is most likely due to heat conduction via the vapor pressure capillaries, which enter the system at the front side. While counter measures, in particular an additional thermal coupling of these capillaries to the helium circuit supplying the inner radiation shield (cf. Sec. 3.2 are presently under discussion, the influence of the existing temperature profile for the WGTS as a worst case scenario is investigated in the following.

As shown in Fig. 6.8, the temperature profile can qualitatively be described by the following empirical equation:

$$T(z) = T_0 + \frac{2}{3} \cdot \Delta T \left(\frac{9\ \mathrm{m}}{9\ \mathrm{m} - z} - 1 \right) \quad \text{for } z > 0\ \mathrm{m}, \tag{6.4}$$

with $T_0 = 29$ K and $\Delta T = 3$ K.

Such a temperature profile has a two-fold influence on the integrated spectrum measured with KATRIN. First, it changes the thermodynamical boundary conditions of the WGTS, and therefore the density profile and even the column density as shown in Fig. 6.9. Second, the Doppler effect is modified due to the different beam tube temperature. The different column density will be determined by calibration measurements, independently of the temperature profile. However the influence of the Doppler effect can only be investigated using the measured temperature profile.

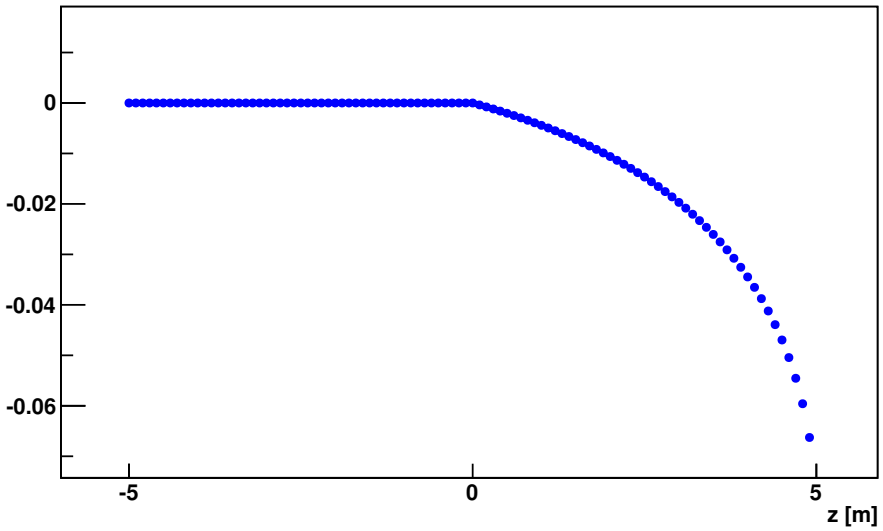

Figure 6.9: **Influence of an inhomogeneous beam tube temperature on the density distribution**. This figure shows the ratio $\frac{\rho(T_0)-\rho(T(z)}{\rho(T_0)}$ for $T_0 = 29$ K and $T(z)$ according to Eq. (6.4) with $\Delta T = 3$ K, as depicted in Fig. 6.8.

To disentangle these effects, 5000 KATRIN measurements have been simulated for different parameters of the temperature profile given above and analyzed in turn with different experimental conditions, summarized in Tbl. 6.3: The first line of Tbl 6.3, shows a worst case scenario: Here, the temperature increase has been ignored and the analysis has been carried out using a constant temperature profile. This includes the systematic shifts both due to the different column density and the different Doppler effect. It results in a systematic shift of $\sigma^{syst}_{m^2_{\nu_e}} = 7.5 \cdot 10^{-3}$ eV^2. In reality, the column density is measured independently and the simulation could be corrected for this effect, therefore this is very conservative. In the second investigated scenario, the temperature profile was inverted for the analysis, thereby putting the temperature increase at the rear side. Due to the symmetry of the WGTS, this ensures that the average values of all quantities including the column density are identical, but the z dependence of temperature and density still differs, leading to a different influence of the Doppler effect on the spectrum. The latter approach is therefore only sensitive to the Doppler effect and implicitly assumes that the column density is known exactly from other monitoring devices and is therefore somewhat optimistic. In this case, the systematic shift disappears. Furthermore, two simulations were performed, decreasing the temperature increase to $\Delta T = 0.3$ K. In this case, the systematic shift disappears for both cases.

The influence of the temperature profile measured at the demonstrator exceeds the allowed systematic error of $0.65 \cdot 10^{-3}$ eV^2 [25] for the most pessimistic case. Therefore counter measures have to be taken, which have to reduce this heat influx by at least one order of magnitude.

In addition to an improved thermal coupling of the vapor pressure capillaries suspected of causing this heat influx to the helium cryocircuit, it is under discussion to redesign the entire WGTS so that the connection of the vapor pressure pipes are

Table 6.3: **Systematic uncertainties for different temperature profiles in simulated KATRIN measurements and their analysis.**

ΔT^{meas}_{front}[K]	ΔT^{meas}_{rear}[K]	ΔT^{ana}_{front}[K]	ΔT^{ana}_{rear}[K]	$\sigma^{syst}_{m^2_{\overline{\nu}_e}}[10^{-3}$ eV$^2]$
3	0	0	0	7.3(3)
3	0	0	3	-0.5(3)
0.3	0	0	0	0.5(3)
0.3	0	0	0.3	-0.3(3)
0	3	0	0	7.5(3)

located at the rear side, thereby effectively inverting the WGTS tube. This would have the additional advantage that the tritium supply line would be shortened by 10 m. However, as can be seen by comparing the first and last row of Tbl. 6.3, the systematic uncertainty does not depend on whether this heat influx happens at the front or rear side. This may seem surprising, since one would expect the influence of the rearmost electrons on the spectrum to be smaller, since these electrons feature a larger scattering probability. While this is the case and therefore the influence of the Doppler effect is reduced, in the first scenario, the systematic error is mostly due to a change in the throughput and column density. This is an integral quantity and therefore independent on the location of the temperature increase. Therefore, this change in the design would lead to no significant improvement on the systematical effect of the temperature profile.

Influence of the mean temperature

While the PT500 sensors reach a precision of 1 mK at 30 K, the foreseen calibration procedure of the PT500 temperature sensors is only accurate to about 100 mK. For monitoring purposes, this is sufficient, since the temperature sensors only have to detect changes to the temperature, which would lead to changes to the column density ρd. However, the differential spectrum is sensitive to the mean temperature via the Doppler effect. In order to verify that the calibration is sufficiently accurate, a similar strategy to the LARA calibration has been employed: The impact via the Doppler effect can again be estimated using the final state "toy model" introduced in Sec. 6.2.1. Similarly to the influence of the gas composition, the width of the final state distribution depends on the temperature. As shown in Fig. 6.10, this indicates a required accuracy of the temperature of a few hundred mK.

As previously for the LARA case, this has been crosschecked using the full analysis chain. In this case, the density profile used in the measurement simulation and analysis was identical, but for the computation of the Doppler effect, different values of the temperature were used. The results are shown in Fig. 6.11. They agree with the results obtained with the toy model:

$$\Delta T_{cal} \lesssim 600 \text{ mK}. \tag{6.5}$$

for a systematic error of $\sigma^{T}_{m^2_{\overline{\nu}}} = 0.6 \cdot 10^{-3}$ eV$^2 = 0.1\sigma^{desc}_{m^2_{\overline{\nu}}}$.

The error of the mean beam tube temperature is dominated by the systematic uncertainty of the PT500 sensors of about 200 K [73], which already fulfills this requirement.

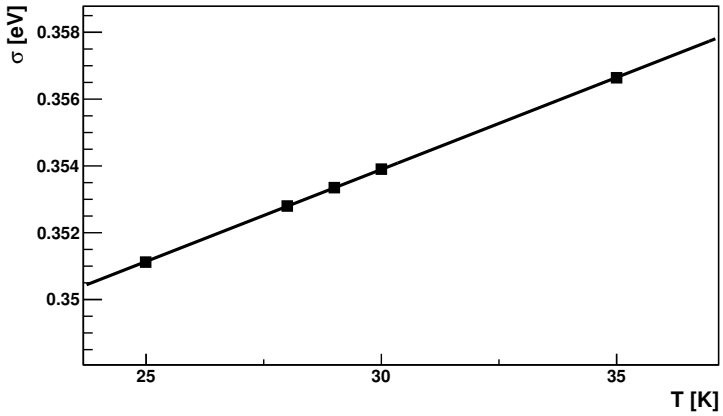

Figure 6.10: **Variation of the width of the Doppler smeared final state distribution for different temperatures**. As in Fig. 6.6, a Gaussian distribution was fitted through the final state distribution for each temperature and the width is given by the width σ of this Gaussian. From the slope of the linear fit $\sigma_{FSD}^{gaus}[\mathrm{eV}] = 0.33736(5) + 0.000551(2)T/\mathrm{K}$, one can compute that the total allowed error for the width final state distribution of 0.00355 eV (1% of the width), corresponds to a requirement for the accuracy of the temperature of about $\frac{0.00355}{0.000551}$ K $\approx$ 6.4 K. However, as in the LARA case, this contribution should be avoided altogether; requiring as before that the systematic error due to the measurement of the mean temperature is about factor of 10 smaller than the overall final state uncertainty leads to $\Delta T_{cal} \lesssim 600$ mK.

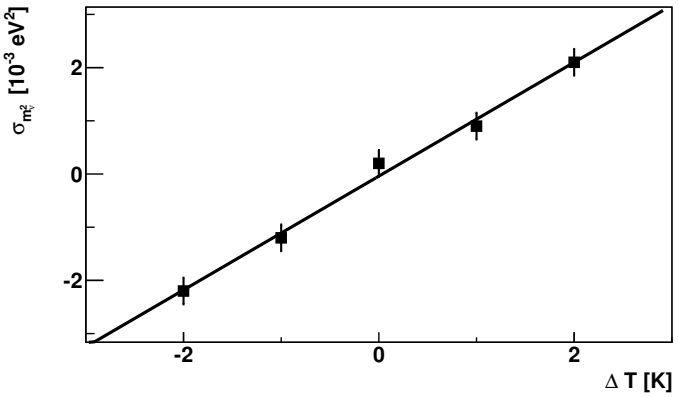

Figure 6.11: **Systematic errors due to the Doppler effect**. 5000 KATRIN measurements have been simulated with a mean temperature of $T_{meas} = 29$ K and analyzed with different temperatures $T_{ana} = T_{meas} + \Delta T$, using the same density profile. Therefore, this only includes the influence of the Doppler effect and ignores the changes to the column density, since these can be independently measured. The linear fit $\sigma_{m_\nu^2}$ [10^{-3} eV^2] $= -0.04(11)+1.07(8)T$[K] implies $\sigma_{m_\nu^2}^{desc} = \sigma_{m_\nu^2}^{T} = 6{\cdot}10^{-3}$ eV^2 at about $T = 6$ K, in good agreement with the toy model estimation.

In summary, the final state toy model constitutes a useful crosscheck to the full analysis chain and provides qualitatively similar results. Regardless of the method, the accuracy of the both the LARA system and the temperature sensors on the beam tube should not lead to significant additional uncertainties; provided the ongoing calibration efforts work as expected, the total systematic error due to the final state distribution according to Eq. (6.2) only increases by about 1%. However, the situation is different for the non-uniform temperature profile observed at the WGTS demonstrator. In order to avoid additional systematic effects, the temperature inhomogeneity needs to be reduced by at least one order of magnitude.

6.3 Potential improvements to KATRIN

In comparison to its predecessors Mainz and Troitsk, the KATRIN experiment reaches its improved sensitivity by increasing the source activity and correspondingly the size of the flux tube, while simultaneously reducing systematic errors identified by the Mainz and Troitsk experiments. Given the technical challenges already involved in reaching the sensitivity of 200 meV, it is unlikely, that a more sensitive successor experiment using the same principle could be build. Such an experiment would require an even larger spectrometer vessel to accumulate sufficient statistics in a reasonable amount of time. Leaving aside the tremendous technical challenges in designing such a vessel, already the transport of such a vessel to the KIT Campus North as essentially the only place where the necessary amount of tritium could be handled, would either require the construction of several new roads for the transportation or the relocation of several houses in certain smaller German villages. The alternative would be to build this vessel on site, which would mean building the infrastructure necessary for its construction first. Neither option is likely to be financially possible and certainly not cheap. Therefore it is important to get the optimal efficiency from the KATRIN setup, in particular the main spectrometer vessel. This section briefly summarizes initial investigations with respect to foreseen improvements of the KATRIN setup, which led to a more detailed investigation in [90].

As outlined above, constructing a new spectrometer is out of question, therefore the remaining possibilities for improvement are the source and the detector. The only source believed to constitute a significant improvement over a windowless gaseous tritium source would be an atomic tritium source. Since in this case the daughter nucleus would be atomic $^3He^+$, which does not have any rotational or vibrational states, this would eliminate the systematic uncertainty associated with the final states of molecular ^3HeT. However, designing an atomic tritium source of the required intensity seems extremely challenging. This leaves a potential upgrade of the main detector as most viable option: By using a detector with an energy resolution of about 1eV at an electron energy of 18.6 keV, a differential spectrum could be measured instead of an integral one. Since an integration implies by definition a loss of information, one can expect an improvement of the sensitivity on the neutrino mass.

6.3.1 The improved KATRIN setup

The hypothetical experimental setup would consist of the standard KATRIN beam line discussed in Chapter 3, however the detector would be replaced with an ultra-

high resolution detector with an energy resolution around 1 eV. This approach combines the advantages of using a tritium source, namely high rates and known systematics, with the advantageous of bolometric measurements − the excellent energy resolution when measuring a differential spectrum as opposed to an integral one. Such an energy resolution has already been achieved with microcalorimeters, and could possibly also be achieved by measuring the synchrotron radiation of single electrons. With such a detector, it would no longer be necessary to use the main spectrometer to perform the energy analysis, instead it would be operated with a fixed retarding potential like the pre-spectrometer, in order to reduce the rate of decay electrons at the detector. In that case KATRIN no longer measures an integrated spectrum, but a differential one, which is modified due to energy losses in the source. In addition, also the detector resolution needs to be taken into account. Therefore this effective spectrum $\left(\frac{\mathrm{d}N}{\mathrm{d}E}\right)^{eff}(E)$ defined previously in Eq. (5.34) needs to be convoluted with the detector resolution function $R(E, \Delta E)$, which is assumed to be described by a Gaussian distribution with mean value E and width $\sigma = \Delta E$ in the following.

$$N(E) = \int_{-\infty}^{+\infty} \left(\frac{\mathrm{d}N}{\mathrm{d}E}\right)^{eff}(E)\, R(E', \Delta E')\mathrm{d}E' \tag{6.6}$$

In practice, the integral runs over the interval of $[-5\Delta E, +5\Delta E]$. As before, 5000 simulated measured spectra for 3 years measurement time have been calculated and analyzed in the way outlined above, using Eq. (6.6) instead of Eq. (3.6) and combining the simulated data in 1 eV binning. The retarding potential was fixed, therefore all energies above the retarding potential are measured simultaneously for the complete measurement time.

6.3.2 Sensitivity of the improved setup

In order to estimate the sensitivity of an improved KATRIN setup, a serious of simulations for various energy resolutions, measurement intervals, and background rates have been performed. The results are summarized in Fig. 6.12 and Fig. 6.13: It is evident that the sensitivity on $m^2_{\overline{\nu}_e}$ increases by about a factor of 2-3 in comparison to the standard KATRIN sensitivity of 0.017 eV^2 within three years measurement time. This improves the statistical sensitivity on $m_{\overline{\nu}_e}$ itself to about or below 100 meV, dependent on the experimental parameters. Since the experimental setup will be largely identical to the first phase of KATRIN, it will be extremely well understood, and additional measures for a reduction of systematical uncertainties could be taken.

However, as shown in Fig. 6.13, achieving an excellent energy resolution is mandatory in this case. If an energy resolution of only 2.5 eV would be achieved, the improvement in sensitivity in comparison to the standard KATRIN setup is already quite small and not worth the effort.

Regardless, this approach for a second phase of KATRIN also offers additional advantages regarding background discrimination and known systematic uncertainties:

- Due to the extremely good energy resolution, almost all background from the external sources like the main spectrometer can be discriminated using the measured energy. Since the analyzed energy range is reduced from a few keV

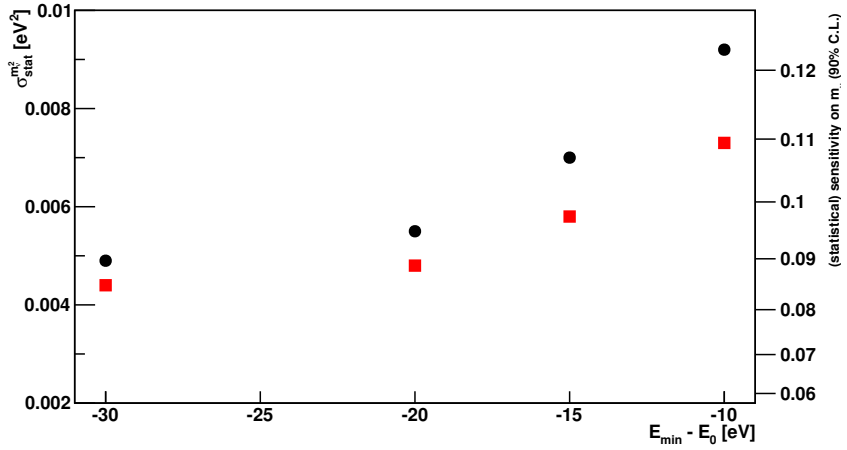

Figure 6.12: **Estimated sensitivity for an upgraded KATRIN experiment**. This figure shows the statistical error on $m^2_{\overline{\nu}_e}$ and the corresponding 90% C.L. on $m_{\overline{\nu}_e}$ for three years measurement time and different analysis intervals for two different background rates. Black circles (red squares) correspond to 10(1) mHz background, equally distributed over the entire analysed interval. As can be seen, with an energy resolution of 1 eV a statistical sensitivity below 100 meV can be reached within that time period.

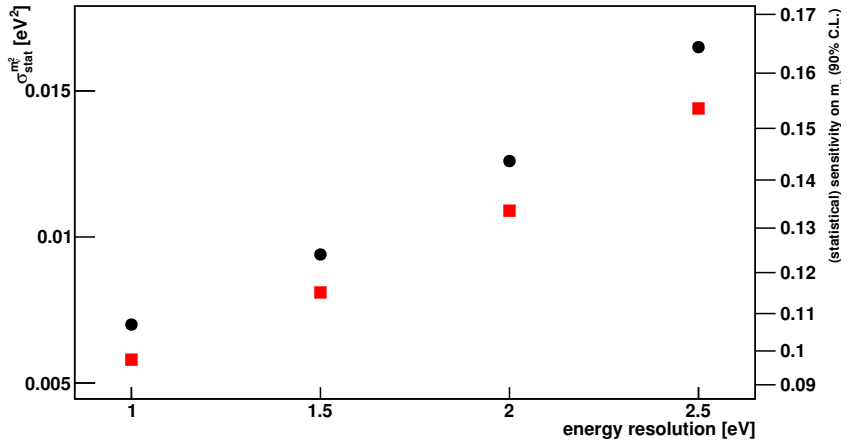

Figure 6.13: **Estimated sensitivity for an upgraded KATRIN experiment for different energy resolutions**. Here, the sensitivity of the improved setup is shown for different energy resolutions, three years measurement time and an analysis interval starting 15 eV below the endpoint. As in Fig. 6.12, black circles (red squares) correspond to 10(1) mHz background. Evidently, a good energy resolution is mandatory. In case the energy resolution would be only 2.5 eV, the improvement over the standard KATRIN setup is already quite small.

to a few eV, the contribution of the known backgrounds drops by 2-3 orders of magnitude. The background assumptions here are chosen rather conservative, since the intrinsic background of the new detector is not known.

- The influence of the spectrometer transmission characteristics disappears from the analysis, provided one analyzes an energy interval which is about 1.5 eV smaller than the transmitted energy interval. In this case, the spectrometer operates at full transmission over the entire analysis interval and high voltage fluctuations smaller than this safety gap do not change the transmission characteristics at all. This eliminates one of the major systematic uncertainties with respect to the original KATRIN setup.

- The systematic error can be further reduced by choosing a smaller analysis interval. Energy losses due to inelastic scattering could be completely eliminated from the region of interest by choosing an analysis interval of only 10 eV. Consequently, another major systematic uncertainty would be completely eliminated. However, the loss in statistical sensitivity would already be quite severe: as shown in Fig. 6.12, the statistical sensitivity on $m_{\bar{\nu}}$ is about 20% lower than for an analysis interval of 20 eV. Therefore, the latter seems to be a more likely compromise between statistical sensitivity and systematical uncertainties. This choice would still exclude multiple scattering events from the region of interest.

However, there are also several caveats and open questions:

- The systematic uncertainty taken over from the existing KATRIN setup would then be dominated by the uncertainty associated with the excited states of ^{3}HeT. Since this is a theoretical uncertainty associated with the computation of the β-decay spectrum itself, it is difficult to reduce this further.

- The energy resolution has a large impact on the sensitivity and will contribute significantly to the systematic error. Therefore, the detector characteristics need to be very well understood.

- The technology used is still open, but will definitely bring its own challenges with it. In particular, the transfer of the β-electrons into the detector with no or at least controlled energy losses will be a tremendous challenge. In the bolometric case, surface effects of the bolometer would have to be precisely understood. In case the synchrotron option is chosen, one would almost certainly need to trap a single electron somewhere, in order to measure the synchrotron radiation with high precision (within a reasonable amount of space). Trapping and releasing these electrons without accidental changes to the electron energy will also be challenging.

Nevertheless, the approach seems promising to potentially allow the KATRIN collaboration to reach a sensitivity below 100 meV, provided such a detector can be build and the electrons can be injected in a controlled way. Further investigations about the possible technical realizations of this improved setup can be found in [90]. Regardless, a major R&D effort will of course be necessary to realize this improved setup.

7. Summary and Outlook

In order to reach the projected sensitivity of 200 meV with the KATRIN experiment, an understanding of the experimental setup, in particular the different sources for systematic uncertainties is mandatory. To this end, a dedicated simulation and analysis framework, which encompasses the complete KATRIN setup is indispensable. This thesis contributed significantly to this framework, called Kassiopeia. Furthermore, dedicated simulation and analysis tools were developed and integrated in Kassiopeia during this thesis. The first of these modules allows to compute the integrated spectrum measured in KATRIN, incorporating important corrections to this spectrum, such as:

- radiative corrections due to photon emission during the β-decay process
- energy remaining with the daughter molecule HeT/HeD, either in excited states or in the recoil energy
- the Doppler effect due to the thermal motion of the gaseous tritium molecules
- energy losses due to inelastic scattering
- changes to the transmission characteristics due to variations of magnetic fields and electric potentials

The spectrum calculation also allows for the first time to take into account inhomogeneities of key experimental parameters. These inhomogeneities influence the above quantities and therefore the integrated spectrum. This is achieved by using a detailed model of the whole KATRIN experiment, including for example the temperature of the WGTS beam tube and therefore of the tritium gas, as well as different magnetic field strengths and electric potentials throughout the system.

In addition, an event generation framework has been developed, which constitutes an important part of the application of Kassiopeia to compute particle trajectories in order to simulate signal and background processes within the KATRIN beam line in detail. This includes for example different possibilities for the β-decay itself, as well

as different calibration and background sources. Furthermore, an analysis module allows the determination of systematic influences of experimental parameters on the neutrino mass.

In light of results from two recent tests of monitoring devices, the WGTS demonstrator and the Laser Raman system, which determine important input parameters for the experimental model, the spectrum calculation and analysis modules were applied to investigations of the impact of these test experiments on the KATRIN sensitivity, in particular the systematic error. The first test setup, the WGTS demonstrator is dedicated to fully test the stability of the complex WGTS cooling system using original components. Thereby it also allows to determine the beam tube temperature profile, an important ingredient of the gas dynamics calculation. Additionally, the Laser Raman system, which is part of the inner Tritium loop, measures the gas composition. Both the temperature and the gas composition have an effect not only on the gas dynamics, but also on the differential spectrum itself: Both affect the effective final state distribution, which is a weighted mean of the final state distribution of the respective daughter molecules HeT and HeD. Furthermore, the temperature dependent Doppler effect effectively causes a smearing of the final state distribution. Both effects were not investigated in detail before, indeed, a final state distribution of HeD has only been published recently. The studies show that no significant additional systematic uncertainties on $m_{\overline{\nu}}^2$ are caused by these effects, provided both the temperature sensors on the WGTS beam tube and the Laser Raman system reach their foreseen accuracy. In this case, the corresponding systematic errors on $m_{\overline{\nu}}^2$ would be below $0.6 \cdot 10^{-3}$ eV^2, and can be neglected in comparison to the estimated systematic uncertainty due to the description of the final state distribution itself, which is $6.0 \cdot 10^{-3}$ eV^2. However, the temperature profile observed at the WGTS demonstrator could lead to additional systematic uncertainties, if it would still be present in the fully assembled WGTS due to its influence on the gas dynamics. The corresponding systematic error could be even larger than the already critical value obtained here $\sigma_{m_{\overline{\nu}}^2}^{syst} = 7.5 \cdot 10^{-3}$ eV^2 due to the fact that a larger number of pumping chambers will be operated in the WGTS and therefore the heat influx increases. Therefore, counter measures have to be taken. In particular, improving the thermal coupling between the capillaries of the vapor pressure on the beam tube and the 27 K He cryogenic circuit is mandatory.

As a further application of this framework, the sensitivity of an envisioned upgrade of the KATRIN setup has been determined. In this scenario, the existing KATRIN detector would be replaced by an ultra-high resolution detector with an energy resolution of only 1 eV at 18.6 eV. This would allow to measure directly the differential β-spectrum instead of an integrated one by operating the main spectrometer with a fixed retarding potential. Such a high energy resolution could be achieved using a bolometric measurement. Alternatively, the precise measurement of the synchrotron radiation of a single electron could also be employed. The feasibility of these technologies needs to be further investigated, but the initial results reported here show that the KATRIN experiment could reach a sensitivity below 100 meV with such a detector.

While the spectrum calculation itself already provides a useful tool and may remain essentially unchanged, several key ingredients of the underlying experimental model will be determined more accurately with dedicated calibration measurements when

the KATRIN experiment is fully assembled. This includes in particular the energy loss and the transmission function of the KATRIN experiment. In addition, a three dimensional gas dynamics simulation is being developed. Also, the three-dimensional configuration of the experimental model currently does not take into account the fact that scattering processes may change the detector pixel of an decay-electron emitted in a given part of the source. The angular change caused by scattering of electrons with the residual gas is quite small (mostly below 1°). Nevertheless, this "cross-talk" between different regions of the source could be included in the future, but it would have to be determined by a high-statistics simulation of the entire KATRIN setup, consisting of more than one billion events, and verified with the rear-section e-gun. Therefore, special emphasis has been put on a modular object oriented design which allows to incorporate new results and alternative computation strategies easily, without having to change already existing methods.

A. Appendix

A.1 Accuracy, precision, trueness

Often, ”precision” and ”accuracy” are used as synonyms or they are mixed up. The term ”trueness” is hardly known in the scientific community. However, the terminology is clearly defined in international norms and guides, e.g. [91].

The following listing is a direct quote from the *JCGM 200:2008 International vocabulary of metrology − Basic and general concepts and associated terms (VIM)* section 2.13-2.15 [91].

(Measurement) accuracy Closeness of agreement between a measured quantity value and a true quantity value of a measurand

(Measurement) trueness Closeness of agreement between the average of an infinite number of replicate measured quantity values and a reference quantity value

(Measurement) precision Closeness of agreement between indications or measured quantity values obtained by replicate measurements on the same or similar objects under specified conditions

Therefore, trueness is related to the systematical uncertainty, whereas precision is related to the statistical uncertainty. Accuracy includes both.

A.2 Kassiopeia configuration files

This section contains some of the Kassiopeia configuration files.

The file UserConfiguration.txt specifies technical details:

```
############################################################
# UserConfiguration File
#
# This is an example of a UserConfiguration file
# The order of the sections is important:
#   1. Prelimiary Configuration -- Verbosity:
#      Set this first so all subsequent printing to the screen
# and log file is performed at the appropriate level.
#   2. Parameter Replacement Variables:
#      This is second so that everything after it is subject
# to the specified parameter replacements.
#   3a. Preliminary Configuration -- Default Directories:
#       The default directories are needed to find the other
# configuration files and the data files.
#   3b. Local Configuration Files:
#       If there are any Configuration files you want to use
#that have custom names or locations, specify them here.
############################################################
@configkey(User)


############################################################
# Preliminary Configuration: Verbosity Level and Debug Flags
############################################################

<PreliminaryConfiguration>

    # The verbosity level
    # Kassiopeia can give you information about your simulation
    # with different levels of detail:
    #   Error: only errors and fatal errors
    #   Warning: warnings
    #  Global: general messages, like which config files are used
    #   Run: basic information about your simulation
    #   Event: information about the events
    #   Track: information about start and end of each track
    <<VerbosityLevel=Event>>

    # Debug flags
    # Debug messages can be activated in different modules of the code.
    # The flags can be used only if the debug preprocessor flag is set
    # (run ./configure --help to see how to do this)
    # All debug flags are off by default.
    # Example: <<DebugOn=Core>>
```

```
</PreliminaryConfiguration>

################################################################
# Parameter Replacement Variables
################################################################

# Example
#<ParameterReplacement>
#    <<Variable=RunNumber>>
#    <<Value=12345>>
#</ParameterReplacement>

################################################################
# Preliminary Configuration: Default Directories and Deactivating Toolboxes
################################################################

<PreliminaryConfiguration>
    # The path to your default-named configuration files
    # (anything that's not specified below)
    <<OptionHome=/home/wkaefer/KASSIOPEIA/branches/SSCbranches/DopplerTest/etc>>

    # The path to your input files for scattering, field calculation, SSC ...
    <<DataHome=/home/wkaefer/KASSIOPEIA/branches/SSCbranches/DopplerTest/Data>>

    # To deactivate a toolbox:
    # <<DeactivateManager=KEY>>
    # Available keys: DAQ, Field, Generator, Geometry, SSC, StepStrategy
</PreliminaryConfiguration>

################################################################
# Local Configuration Files
#   Specify the Key and FileName.
#
################################################################

# Example:
#<ConfigFile>
#    <<Key=Geometry>>
#    <<FileName=../ConfigDirectory/SomeGeometryConfigFile.txt>>
#</ConfigFile>
```

The file SSCConfiguration.txt contains the configuration of the spectrum calculation module.

```
1
 ########################################################################
# Source Spectrum Generation SSC configuration
########################################################################
@configkey(SSC)

########################################################################
# SSCTemperature1D
# standard temperature profile

<SSCTemperature1D>
<<Name=Temperature1D>>
<<T0=30.>>  #nominal beam tube temperature
<<deltaT=0.03>>  #longitudinal deviation towards pump port
</SSCTemperature1D>




########################################################################
# SSCDensity1D
# 1D density profile, specified by pressure ratio and either injection
# pressure or column density rhod.
# needs a predefined SSCTemperature or an inline definition

<SSCDensity1D>
<<Name=Density1D>>
<<TemperatureName=Temperature1D>>
<<P_in=0.3368>>   # injection pressure in Pa
<<P_ex/P_in=0.05>> # ratio: exit pressure / injection pressure
<<rhod=5.0E21>>    # column density
<<CalculateDensity=P_in>> # choose between P_in or rhod
<<length=10.>>     # length (m)
<<radius=0.045>>   # radius (m)
</SSCDensity1D>

########################################################################
# SSCGasDynamics1D
# manages a 1D density and temperature profile.
# just add names or define these object inside the following block.

<SSCGasDynamicsCalculator1D>
<<Name=GasDynamics1D>>
<<TemperatureName=Temperature1D>>
<<DensityName=Density1D>>
</SSCGasDynamicsCalculator1D>
```

```
########################################################################
# SSCFieldMap

<SSCFieldMap0D>
<<Name=FieldMap0D>>
<<B_max=6.0>># max. magnetic field (T)
<<B_A=3E-4>># magnetic field in analysing plane (T)
<<R_A=4.5>># radius of analysing plane (m)
</SSCFieldMap0D>


########################################################################
# SSCDetector

<SSCDetector0D>
<<Name=Detector0D>>
<<Efficiency=0.9>> # efficiency for detecting an electron in detector
<<Background=0.01>># background rate at detector (Hz)
<<DetectorPositionZ=13.98>> # m. position of coordinate system in analysis plane
</SSCDetector0D>


<SSCWGTS>
<<Name=WGTS1>>
<<MagfieldName=Magfield3KATRIN>>  # name of used magneticField
<<GasDynamicsName=GasDynamics1D>>
<<BeamtubeLength=10.>>   # length (m)
<<BeamtubeRadius=0.045>> # radius (m)
<<NSlices=1000>>         # number of long. slices (along beam axis)
<<NRings=1>> # number of rings in each slice
<<NSegments=1>> # number of segments in each ring
<<NCenterSegments=1>> # number of central segments in innermost ring
<<NRebinnedSlices=10>> # number of slices after rebinning (long.)
<<Shape=WGTS>> # decide density shape (CONSTANT or WGTS)
<<SlicingType=FLUXTUBE>> # decide type of source slicing (FLUXTUBE or DETECTOR)
<<Flux=0.0192>> # transported magnetic flux (Tm^2 !!)
<<FieldMapName=FieldMap0D>>
<<UseStandardWGTS=true>>
 #
</SSCWGTS>

########################################################################
#a constant background
<KSCBackgroundConst>
<<Name=mybgconst>>
<<Rate=0.01>>
```

```
</KSCBackgroundConst>


<SSCFinalStates>
    <<Name=SSCFinalStates1>>
    <<FSDModel=0>>
    <<TritiumPurity=0.95>>
</SSCFinalStates>
#########################################################################
#differential spectrum with final states for T2 and DT
<KSCDifferentialSpectrumFSD>
<<Name=myT2SpecFSD>>
<<Endpoint=18575.>>
<<NeutrinoMassSquared=0.>>
<<Z=2>>
<<FinalStatesName=SSCFinalStates1>>
</KSCDifferentialSpectrumFSD>
#
#


#########################################################################
#a differential spectrum with neutrino mixing
<KSCDifferentialSpectrumMixing>
    <<Name=myT2SpecMixing>>
    <<Endpoint=18575>>
    <<Z=2>>
    <<TritiumPurity=0.95>>
    <<Masses=0.9:5.0>>
    <<MixingElements=0.5:0.5>>
</KSCDifferentialSpectrumMixing>

#########################################################################
#a  spectrum of decay lines
<KSCLineSpectrum>
<<Name=dummy>>
#can consist of gaussians, lorentzians and voigtians
<KSCGaussian>
#<<Name=mygaus>>
<<Mean=18000>>
<<Sigma=2>>
<<Alpha=1>>
</KSCGaussian>


<KSCLorentzian>
#<<Name=mylorent>>
<<Mean=18000>>
<<Gamma=3>>
```

```
<<Alpha=1>>
</KSCLorentzian>

<KSCVoigt>
#<<Name=myvoigt>>
<<Mean=18000>>
<<Sigma=2>>
<<Alpha=1>>
<<Gamma=3>>
</KSCVoigt>
</KSCLineSpectrum>

########################################################################
#spectrum with wgts energy loss
<KSCEffectiveSpectrum>
<<Name=myeffspec>>
<<WGTSName=WGTS1>>
<<AddDifferentialSpectrum=myT2SpecFSD>>
<<DetectorName=Detector0D>>
<<FieldmapName=FieldMap0D>>
<SSCElossAseev>
<<convsteps=1000>>
<<hconv=0.1>>
</SSCElossAseev>
</KSCEffectiveSpectrum>



########################################################################
#response function
<KSCResponse>
<<Name=myresponseAseev>>
<KSCTransmission>
<<FieldmapName=FieldMap0D>>
</KSCTransmission>
<SSCElossAseev>
<<NConvolutions=4>>
<<convsteps=2000>>
<<hconv=0.1>>
</SSCElossAseev>
</KSCResponse>

#standard integrated spectrum
<KSCSSCIntegratedSpectrum>
<<Name=myintspec>>
<<WGTSName=WGTS1>>
<<AddDifferentialSpectrum=myT2SpecFSD>>
<<ResponseName=myresponseAseev>>
<<DetectorName=Detector0D>>
```

```
</KSCSSCIntegratedSpectrum>


#this spectrum is used to generate an interpolation grid
# it uses a simplified parametrization of the integrated spectrum
<SSCIntegratedSpectrumKSOP>
        <<Name=myksopspec>>
        <<WGTSName=WGTS1>>
        <<AddDifferentialSpectrum=myT2SpecFSD>>
        <<ResponseName=myresponseAseev>>
        <<DetectorName=Detector0D>>
</SSCIntegratedSpectrumKSOP>

#this spectrum uses the interpolation grid to compute the integrated spectrum
<KSCSpectrumInterpolate>
        <<Name=myspecInterpol>>
        <<LibraryFilename=test.root>>
</KSCSpectrumInterpolate>



######################################################################
#the runtimemanager is in charge of managing the simulated measurement time:
<KSCRuntimeManager>
<<Name=myrt>>
<<MeasTimeDistributionfile=time-3y-jopti30eV10mHz.dat>>
<<ScanMethod=Integral>>
</KSCRuntimeManager>

#for differential (KATRINII) measurement
<KSCRuntimeManager>
<<Name=myrtdiff>>
<<MeasTimeDistributionfile=time-3y-diff.dat>>
<<ScanMethod=Integral>>
</KSCRuntimeManager>

######################################################################
#the measument class generates a "measured" spectrum,
#with signal, background and
#statistical errors based in the measurement time distribtion of the runmanager
<KSCMeasurement>
<<Name=mymeas>>
<<AddBackground=mybgconst>>
<<SpectrumName=myintspec>>
<<RuntimeManagerName=myrt>>
<<Smearing=on>>
</KSCMeasurement>
```

```
# for a differential measurement, use this class instead.
<KSCMeasurementDifferential>
<<Name=mymeasdiff>>
<<AddBackground=mybgconst>>
<<SpectrumName=myeffspec>>
<<RuntimeManagerName=myrtdiff>>
<<Smearing=on>>
<<MinEnergy=18565>>
<<MaxEnergy=18580>>
<<BinWidth=1.>>
<<Resolution=1.>>
</KSCMeasurementDifferential>
```

Particle generators are configured in GeneratorConfiguration.txt:

```
 ############################################################
# Particle generation configuration
############################################################
#
# Define here which particle generator you want to use for your simulation
# You can use several generators at the same time and weight them.
# If only one generator is used, the weight is ignored...
#
#
#
# A fully configured generator needs the following information:
# A) rules for position generation
# B) rules for direction generation
# C) rules for time generation
# D) rules for energy generation
# E) rules for special actions (at hte moment, only doppler effect)
# F) combination of these building blocks to a generator
# G) Special generators:
#  some generators do not allow these random combination of properties
# like the PAGEGeneratorASCII. These will be listed here..
#
# This file contains a full list of available options.
#
#
############################################################
# WARNING!
# Some Mechanisms can only be combined with certain other mechanisms.
#
#
#
#
############################################################
# A) Position:
############################################################
# This section lists the available Position Creators:
# fixed position generator
# following tritium gas distribution in WGTS beam tube (using SSC)
# equally distributed in a volume,
# equally distributed on surface.
#

@configkey(Generator)

#
#fixed position creator::
<PAGEPositionCreatorFix>
<<Name=myposFix>>
```

```
<<StartPositionX=-0.615441.0>>
<<StartPositionY=-0.344749>>
<<StartPositionZ=-0.471114>>
</PAGEPositionCreatorFix>

# position creation for signal electrons
#using the tritium gas distribution in the WGTS:
#only makes sense for tritium and to some extend krypton in the WGTS.
#ensure coordinate system consistency
#between SSC and the rest of the simulation!
<PAGEPositionCreatorSSC>
<<Name=myposSSC>>
<<WGTSName=WGTS1>>
</PAGEPositionCreatorSSC>

<PAGEPositionCreatorDisk>
    <<Name=myposDisk>>
    <<RMax=0.42>>
    <<NormalvectorX=0.>>
    <<NormalvectorY=0.>>
    <<NormalvectorZ=1.>>
    <<OriginX=0.>>
    <<OriginY=0.>>
    <<OriginZ=0.>>
</PAGEPositionCreatorDisk>



<PAGEPositionCreatorSurface>
<<Name=mypossurface>>
<<GeometryName=PreSpectrometer>>
<<SurfaceDistance=0.01>>
<<SurfaceOption=1>>
# Options: 1 will start particles inside the surface,
# 0 will start them outside
</PAGEPositionCreatorSurface>

<PAGEPositionCreatorVolume>
<<Name=myposVolume>>
<<GeometryName=PreSpectrometer>>
#<<RMin=0>> #optional restriction of the geometry.
#<<RMax=10>> #optional restriction of the geometry.
#<<ZMin=-2.5>> #optional restriction of the geometry in z direction
#<<ZMax=2.5>> # optional restriction of the geometry in z direction
</PAGEPositionCreatorVolume>

##################################################################
# B) direction:
##################################################################
```

```
# available are:
# a) Fixed angles
# b) gaussian angular distribution, e.g. for an angular defined egun
# c) Isotropic: the standard for radioactive decays
# d) Surface: only in combination with the position generation on a surface.
#
#
<PAGEDirectionCreatorFix>
<<Name=mydirFix>>
<<Theta=0.>>#polar angle to z axis, in degrees
<<Phi=0.>>#azimuthal angle in  degrees
</PAGEDirectionCreatorFix>

<PAGEDirectionCreatorGauss>
<<Name=mydirGauss>>
<<Theta=10>>#polar angle to z axis, in degrees
<<SigmaTheta=10>>#polar angle to z axis, in degrees
<<Phi=0.>>#azimuthal angle in  degrees
<<SigmaPhi=10>>#polar angle to z axis, in degrees
</PAGEDirectionCreatorGauss>

#polar angle theta = 0 points towards the detector, range [0,180]
#azimuthal angle phi range [0,360]
<PAGEDirectionCreatorIsotropic>
<<Name=dirIsotropic>>
<<ThetaMin=0.>>
<<ThetaMax=180.>>
<<PhiMin=0.>>
<<PhiMax=360.>>
</PAGEDirectionCreatorIsotropic>

<PAGEDirectionCreatorSurface>
<<Name=mydirSurface>>
# needs to be  used in combination to a position creator of type surface!
# this is checked automatically
</PAGEDirectionCreatorSurface>

<PAGEDirectionCreatorGold>
    <<Name=mydirGold>>
    <<NormalvectorX=0.>>
    <<NormalvectorY=0.>>
    <<NormalvectorZ=1.>>
</PAGEDirectionCreatorGold>


##############################################################
# C) time
##############################################################
# available are:
```

```
# decay: exponential decay
# equidistant
# fix

#no idea whether these numbers make any sort of sense...
<PAGETimeCreatorDecay>
<<Name=mytimeDecay>>
<<Starttime=0>>
<<DecayConstant=100000000>>
<<NMolecules=1e18>>
</PAGETimeCreatorDecay>

<PAGETimeCreatorEquidistant>
<<Name=mytimeEqui>>
<<StartTime=0.0>>
<<Frequency=1000>> #Hz
</PAGETimeCreatorEquidistant>

<PAGETimeCreatorFix>
<<Name=mytimeFix>>
<<StartTime=4.29958E-9>>
</PAGETimeCreatorFix>

################################################################
# D) energy
################################################################
#
# basic energy creators: these use standard distributions:
# equally distributed, gaussian and simply fixed.
#
# equally distributed:

<PAGEEnergyCreatorEqual>
    <<Name=myEnergyEqual>>
    <<MinimumEnergy=18000>> #eV
    <<MaximalEnergy=19000>> #eV
</PAGEEnergyCreatorEqual>

<PAGEEnergyCreatorFix>
    <<Name=myEnergyFix>>
    <<Energy=308705>>
</PAGEEnergyCreatorFix>

<PAGEEnergyCreatorGauss>
    <<Name=myEnergyGauss>>
    <<MeanEnergy=18000>>
    <<SigmaEnergy=10>>
</PAGEEnergyCreatorGauss>
```

```
#radioactive decay generators
#simple krypton generator
<PAGEEnergyCreatorKrypton>
    <<Name=myEnergyKrypton>>
    <<Filename=krypton>>
    <<MinimumEnergy=17000>>
    <<MaximalEnergy=50000>>
</PAGEEnergyCreatorKrypton>

#advanced Krypton generator
#generates conversion and auger electrons. Many electrons per event are possible.
<PAGEEnergyCreatorKryptonEvent>
    <<Name=myEnergyKryptonEvent>>
    <<DoConversion=1>>
    <<ForceCreationOfConversionElectron=1>>
    <<DoAuger=1>>
</PAGEEnergyCreatorKryptonEvent>

#Radon generator
#generates shake off, conversion, auger and shell reorganization electrons.
#Many electrons per event are possible.
<PAGEEnergyCreatorRadonEvent>
    <<Name=myEnergyRadon>>
    <<IsotopeNumber=219>>
    <<DoShakeOff=1>>
    <<ForceCreationOfShakeOffElectron=1>>
    <<DoConversion=1>>
    <<ForceCreationOfConversionElectron=1>>
    <<DoAuger=1>>
    <<DoShellReorganization=1>>
</PAGEEnergyCreatorRadonEvent>

#tritium generators
<PAGEEnergyCreatorTritium>
    <<Name=myTritium>>
    <<SSCDifferentialSpectrumName=DifferentialSpectrum1>>
#needs to be defined in SSCConfiguration.txt.
    <<MinimumEnergy=18500>>
    <<MaximalEnergy=18600>>
    <<NBins=1000>>
</PAGEEnergyCreatorTritium>

/*
#this takes a rather long time to initialize, only use it for large statistics.
<PAGEEnergyCreatorTritiumwithWGTSEnergyLoss>
    <<Name=myTritiumwithELOSS>>
    <<SSCIntegratedSpectrumName=IntegratedSpectrum1>>
      #needs to be defined in SSCConfiguration.txt.
    <<MinimumEnergy=18550>>
```

```
    <<MaximalEnergy=18600>>
    <<NBins=1000>>
</PAGEEnergyCreatorTritiumwithWGTSEnergyLoss>
*/
################################################################
# E) special actions:
################################################################

<PAGESpecialCreatorSSCDoppler>
<<Name=mySSCDoppler>>
<<SSCPositionCreatorName=myposSSC>> #only works with sscpositioncreator
</PAGESpecialCreatorSSCDoppler>


################################################################
# F) combination to generators:
################################################################
#
#
/*
<PAGEGenerator>
<<Name=EGun>>
<<Weight=1>>
<<PID=11>>
<<PositionCreatorName=myposFix>>
<<TimeCreatorName=mytimeFix>>
<<DirectionCreatorName=dirIsotropic>>
<<EnergyCreatorName=myEnergyFix>>
</PAGEGenerator>
*/


################################################################
#G) special generators
################################################################
#this one reads  an ascII file or Kassiopeia root output file:
#it expects either an absolute path or a relative path
# to the execution directory
#you can specify the starting parameters with
# position, energy, angle (FileFormat=EnergyAngle)
#or position, momentum (FileFormat=Momentum)
#if you would like to repeat a single track of a large run,
#you can specifiy the path to the root output file
#choose FileFormat=RootOutput
#and give the event no and track no of the particle you want to simulate again

<PAGEGeneratorASCII>
<<Name=File>>
<<Filename=../Data/PAGEGeneratorASCII_Inputfile_Example.txt>>
```

```
    <<FileFormat=EnergyAngle>>
    #<<FileFormat=Momentum>>
    #####
    #<<Filename=../Output/Run17.root>>
    #<<FileFormat=RootOutput>>
    #<<EventId=93>>
    #<<TrackId=0>>
</PAGEGeneratorASCII>
```

Bibliography

[1] Pauli, W. *Dear radioactive ladies and gentlemen. Phys. Today* **31N9** (1978) 27.

[2] Fermi, E. *Versuch einer Theorie der β-Strahlen. Zeitschrift f. Phys. A* (1934).

[3] Cowan, C. L. *et al. Detection of the free neutrino: A Confirmation. Science* **124** (1956) 103.

[4] Peasley, J. *The particle zoo.* `http://www.particlezoo.net/`.

[5] Danby, G. *et al. Observation of High-Energy Neutrino Reactions and the Existence of Two Kinds of Neutrinos. Phys. Rev. Lett.* **9** 1 (1962) 36.

[6] Nakamura, K. *et al.* (Particle Data Group). *Review of particle physics. J. Phys.* **G37** (2010) 075021.

[7] DONUT collaboration. *Observation of tau neutrino interactions. Physics Letters B* Physics Letters B 504(3) 218–224 (2001).

[8] Ahmad, Q. R. *et al.* (SNO). *Measurement of the charged current interactions produced by B-8 solar neutrinos at the Sudbury Neutrino Observatory. Phys. Rev. Lett.* **87** (2001) 071301. nucl-ex/0106015.

[9] Fukuda, Y. *et al.* (Super-Kamiokande). *Evidence for oscillation of atmospheric neutrinos. Phys. Rev. Lett.* **81** (1998) 1562. hep-ex/9807003.

[10] Hosaka, J. *et al.* (Super-Kamiokande). *Solar neutrino measurements in Super-Kamiokande-I. Phys. Rev.* **D73** (2006) 112001. hep-ex/0508053.

[11] Klapdor-Kleingrothas, H. and Zuber, K. *Teilchenastrophysik.* Teubner Studienbücher Physik, Stuttgart (1997).

[12] Davis, R. *A review of measurements of the solar neutrino flux and their variation. Nucl. Phys. Proc. Suppl.* **48** (1996) 284.

[13] Bahcall, J. and Ulrich, R. K. *Solar models, neutrino experiments, and helioseismology. Rev. Mod. Phys.* **60** 2 (1988) 297.

[14] Aliu, E. *et al.* (The K2K Collaboration). *Evidence for Muon Neutrino Oscillation in an Accelerator-Based Experiment. Phys. Rev. Lett.* **94** 8 (2005) 081802.

[15] Adamson, P. *et al.* (MINOS Collaboration). *Measurement of Neutrino Oscillations with the MINOS Detectors in the NuMI Beam. Phys. Rev. Lett.* **101** (2008) 131802. URL http://link.aps.org/doi/10.1103/PhysRevLett.101.131802.

[16] Eguchi, K. *et al.* (KamLAND Collaboration). *First Results from KamLAND: Evidence for Reactor Antineutrino Disappearance. Phys. Rev. Lett.* **90** 2 (2003) 021802.

[17] Wolfenstein, L. *Neutrino oscillations in matter. Phys. Rev. D* **17** (1978) 2369. URL http://link.aps.org/doi/10.1103/PhysRevD.17.2369.

[18] Agafonova, N. *et al. Observation of a first candidate event in the OPERA experiment in the CNGS beam. Physics Letters B* **691** 3 (2010) 138 . URL http://www.sciencedirect.com/science/article/pii/S0370269310007537.

[19] Bellini, G. *et al.* (Borexino collaboration). *Measurement of the solar B8 neutrino rate with a liquid scintillator target and 3 MeV energy threshold in the Borexino detector. Phys. Rev. D* **82** 3 (2010) 033006.

[20] Arpesella, C. *et al.* (Borexino Collaboration). *Direct Measurement of the Be7 Solar Neutrino Flux with 192 Days of Borexino Data. Phys. Rev. Lett.* **101** 9 (2008) 091302.

[21] CHOOZ collaboration. *Limits on Neutrino Oscillations from the CHOOZ Experiment. Phys. Lett.* **B466** (1999) 415. hep-ex/9907037.

[22] Daya-Bay collaboration. *A precision measurement of the neutrino mixing angle theta(13) using reactor antineutrinos at Daya Bay* (2007), hep-ex/0701029.

[23] Double Chooz collaboration. *Double Chooz: A search for the neutrino mixing angle* θ_{13} (2006), hep-ex/0606025.

[24] RENO collaboration. *RENO: An Experiment for Neutrino Oscillation Parameter* θ_{13} *Using Reactor Neutrinos at Yonggwang* (2010), arXiv:1003.1391.

[25] Angrik, J. *et al.* (KATRIN). *KATRIN design report* FZKA-7090 (2004).

[26] Wilson, R. W. and Penzias, A. A. *Isotropy of Cosmic Background Radiation at 4080 Megahertz. Science* **156** (1967) 1100. URL http://adsabs.harvard.edu/abs/1967Sci...156.1100W.

[27] Fixsen, D. J. *et al. The Cosmic Microwave Background Spectrum from the Full COBE/FIRAS Data Set. Astrophys. J.* **473** (1996) 576. astro-ph/9605054.

[28] Ade, P. A. R. *et al.* (Planck collaboration). *Planck early results. I. The Planck mission. A&A* **536** (2011) A1. URL http://dx.doi.org/10.1051/0004-6361/201116464.

[29] Jarosik, N. *et al. Seven-Year Wilkinson Microwave Anisotropy Probe (WMAP) Observations: Sky Maps, Systematic Errors, and Basic Results. Astrophys. J. Suppl.* **192** (2011) 14. 1001.4744.

[30] Brandbyge, J. *et al. The effect of thermal neutrino motion on the non-linear cosmological matter power spectrum. Journal of Cosmology and Astroparticle Physics* **2008** 08 (2008) 020. See also `http://users-phys.au.dk/haugboel/projects.shtml`, URL `http://stacks.iop.org/1475-7516/2008/i=08/a=020`.

[31] Frieman, J. A. *et al. The Sloan Digital Sky Survey-II Supernova Survey: Technical Summary. Astron. J.* **135** (2008) 338. 0708.2749.

[32] Reid, B. A. *et al. Cosmological Constraints from the Clustering of the Sloan Digital Sky Survey DR7 Luminous Red Galaxies. Mon. Not. Roy. Astron. Soc.* **404** (2010) 60. 0907.1659.

[33] Klapdor-Kleingrothaus, H. V. *et al. Evidence for Neutrinoless Double Beta Decay. Mod. Phys. Lett.* **A16** (2001) 2409. hep-ph/0201231.

[34] Klapdor-Kleingrothaus, H. V. and Krivosheina, I. V. *The evidence for the observation of 0nu beta beta decay: The identification of 0nu beta beta events from the full spectra. Mod. Phys. Lett.* **A21** (2006) 1547.

[35] Aalseth, C. E. *et al. Comment on 'Evidence for Neutrinoless Double Beta Decay'. Mod. Phys. Lett.* **A17** (2002) 1475. hep-ex/0202018.

[36] Schonert, S. *et al.* (GERDA). *The GERmanium Detector Array (GERDA) for the search of neutrinoless beta beta decays of Ge-76 at LNGS. Nucl. Phys. Proc. Suppl.* **145** (2005) 242.

[37] Akimov, D. *et al. EXO: An advanced Enriched Xenon double-beta decay Observatory. Nucl. Phys. Proc. Suppl.* **138** (2005) 224.

[38] Pedretti, M. *et al. CUORE experiment: The search for neutrinoless double beta decay. Int. J. Mod. Phys.* **A23** (2008) 3395.

[39] Hirata, K. S. *et al. Observation in the Kamiokande-II Detector of the Neutrino Burst from Supernova SN 1987a. Phys. Rev.* **D38** (1988) 448.

[40] Bionta, R. M. *et al. Observation of a Neutrino Burst in Coincidence with Supernova SN 1987a in the Large Magellanic Cloud. Phys. Rev. Lett.* **58** (1987) 1494.

[41] Loredo, T. J. and Lamb, D. Q. *Bayesian analysis of neutrinos observed from supernova SN 1987A. Phys. Rev.* **D65** (2002) 063002. astro-ph/0107260.

[42] Marmier, P. and Sheldon, E. *Physics of Nuclei and Particles, Vol. VI.* Academic Press, New York (1969).

[43] Behrens, H. and Jänecke, J. *Landolt-Bornstein, New Series.* Springer, Berlin (1969). Group I, Vol. 4., Nuclei - Numerical Tables for Beta-Decay and Electron Capture.

[44] Curran, S. C., Angus, J. and Cockroft, A. L. *The Beta-Spectrum of Tritium. Phys. Rev.* **76** 6 (1949) 853.

[45] Hanna, G. C. and Pontecorvo, B. *The β-Spectrum of H^3. Phys. Rev.* **75** 6 (1949) 983.

[46] Robertson, R. G. H. *et al. Limit on ν_e mass from observation of the β decay of molecular tritium. Phys. Rev. Lett.* **67** 8 (1991) 957.

[47] Beamson, G., Porter, H. Q. and Turner, D. W. *The collimating and magnifying properties of a superconducting field photoelectron spectrometer. Journal of Physics E: Scientific Instruments* **13** 1 (1980) 64.

[48] Lobashev, V. M. *The search for the neutrino mass by direct method in the tritium beta-decay and perspectives of study it in the project KATRIN. Nucl. Phys.* **A719** (2003) 153.

[49] Sturm, M. *Aufbau und Test des Inner-Loop-Systems der Tritiumquelle von KATRIN.* Ph.D. thesis, Karlsruher Institut für Technologie (2010).

[50] Grohmann, S. *et al. Precise temperature measurement at 30 K in the KATRIN source cryostat. Cryogenics* **51** 8 (2011) 438 . URL `http://www.sciencedirect.com/science/article/pii/S0011227511001135`.

[51] Bornschein, B. *et al. Tritium tests with a technical PERMCAT for final clean-up of ITER exhaust gases. Fusion Engineering and Design* **69** 1-4 (2003) 51 . 22nd Symposium on Fusion Technology, URL `http://www.sciencedirect.com/science/article/pii/S0920379603002345`.

[52] Sturm, M. *et al. Monitoring of All Hydrogen Isotopologues at Tritium Laboratory Karlsruhe Using Raman Spectroscopy. Laser Physics* **20** 2 (2010) 493.

[53] Grohmann, S. *Stability analyses of the beam tube cooling system in the KATRIN source cryostat. Cryogenics* **49** (2009) 413.

[54] KATRIN rear section working group. *KATRIN Rear Section conceptual design report v1.1* (2011).

[55] Furse, D. L. (2013). PhD thesis, Massachusetts Institute of Technology, (in preparation).

[56] Mertens, S. (2012). PhD thesis, Karlsruhe Institute of Technology, (in preparation).

[57] Formaggio, J. *et al. Kassiopeia Users Guide 1.50.* Kassiopeia development group. KATRIN internal document.

[58] World Wide Web Consortium. *Extensible Markup Language.* `http://www.w3.org/TR/2006/REC-xml-20060816/`.

[59] Brun, R. *et al. Root Users Guide 5.26.* `http://root.cern.ch/`.

[60] Galassi, M. *et al. GNU Scientific Library Reference Manual (3rd Ed.).* Network Theory Ltd.

[61] Glück, F. *Axisymmetric magnetic field calculation with zonal harmonic expansion. Progress In Electromagnetics Research B* **32** (2011) 351.

[62] Glück, F. *Axisymmetric electric field calculation with zonal harmonic expansion. Progress In Electromagnetics Research B* **32** (2011) 319.

[63] Reich, J. *Magnetfeldmessungen und Designarbeiten für das EMCS Luftspulensystem am KATRIN Hauptspektrometer* (2009). Diploma thesis, Universität Karlsruhe (TH) (in german).

[64] Lazić, P., Štefančić, H. and Abraham, H. *The Robin Hood method - A novel numerical method for electrostatic problems based on a non-local charge transfer. J. Comput. Phys.* **213** (2006) 117. URL `http://dx.doi.org/10.1016/j.jcp.2005.08.006`.

[65] Renschler, P. *KESS - A new Monte Carlo simulation code for low-energy electron interactions in silicon detectors* (2011). PhD thesis, Karlsruhe Institute of Technology.

[66] Repko, W. and Wu, C. *Radiative corrections to the end point of the tritium β decay spectrum. Phys. Rev.* **C28** (1983) 2433.

[67] Doss, N. *et al. Molecular effects in investigations of tritium molecule β decay endpoint experiments. Phys. Rev.* **C73** (2006) 025502.

[68] Doss, N. and Tennyson, J. *Excitations to the electronic continuum of $^3HeT^+$ in investigations of the $T_2\beta$-decay experiments. J. Phys. B: At. Mol. Opt. Phys.* **41** (2008) 125701.

[69] Saenz, A. *et al. Improved molecular final-state distribution of HeT^+ for the β-decay process of T_2. Phys. Rev. Lett.* **84** (2000) 242.

[70] Aseev, V. *et al. Energy loss of 18 keV electrons in gaseous T_2 and quench condensed D_2 films. Eur. Phys. J.* **D10** (2000) 39.

[71] Leiber, B. *Non-axially symmetric field and trajectory calculations for the KATRIN-experiment* (2010). Diploma thesis, Karlsruhe Institute of Technology.

[72] Glück, F. *et al. Air Coil System And Magnetic Field Sensor System, Design report* (2009). KATRIN internal document.

[73] Bode, T. *Experimentelle Untersuchung der thermischen Eigenschaften der KATRIN Tritiumquelle am WGTS-Demonstrator* (2011). Diploma thesis, Karlsruhe Institute of Technology.

[74] Dieter, A. *Analyse ausgewählter Temperaturdaten des WGTS Demonstrators von KATRIN* (2011). Bachelor thesis, Karlsruhe Institute of Technology.

[75] Sharipov, F. *et al. Influence of temperature variations and acoustic waves on the column density. Calculations of the velocity distribution function.* KATRIN Report, 2009.

[76] Kaspar, J. *Influence of energy scale imperfections on neutrino mass sensitivity in the KATRIN experiment.* Diploma thesis, Universität Prag, 2003.

[77] Sharipov, F. *Numerical calculation of tritium flow through the KATRIN beam line*. KATRIN Report, 10-ME-2100-0, 2003.

[78] Sharipov, F. *Calculations of tritium flow between the buffer vessel up to the first vacuum system*. KATRIN Report, 10-ME-2102-0 2004.

[79] Sharipov, F. and Kalempa, D. *Separation phenomena in the tritium source and numerical simulations of turbo-molecular pumps*. KATRIN Report 2005.

[80] Shakov, E. M. *Generalization of the Krook kinetic equation. Fluid dynamics* **3** 1 (1968) 142.

[81] Sharipov, F. and Seleznev, V. *Data on Internal Rarefied Gas Flows* (1998). URL `http://link.aip.org/link/?JPR/27/657/1`.

[82] Valougeorgis, D., Pantazis, S. and Sharipov, F. *Numerical simulation of end effects in the WGTS unit* (2011).

[83] Hoetzel, M. *Berechnung von KATRIN Messspektren unter Einbeziehung der Eigenschaften der fensterlosen gasförmigen Tritiumquelle* (2009). Diploma thesis, Universität Karlsruhe (TH) (in german).

[84] Hein, H. *Angular defined photo-electron sources for the KATRIN experiment* (2010). Diploma thesis, Universität Münster.

[85] Frankle, F. M. *et al. Radon induced background processes in the KATRIN pre-spectrometer. Astropart. Phys.* **35** (2011) 128. 1103.6238.

[86] Windberger, A. *Berechnungen und Simulationen zum Verhalten von Ionen in der differenziellen Pumpstrecke des KATRIN-Experiments* (2010). Diploma thesis, Karlsruhe Institute of Technology.

[87] Eitel, K. *private communication* (2009).

[88] Otten, E. *The Mainz Neutrino Mass Experiment. Prog. Part. Nucl. Phys* **32** (1994) 153.

[89] Kaefer, W., Schloesser, M. and Hoetzel, M. *Investigation on the requirements for accuracy of the KATRIN Laser Raman System* (2012). KATRIN internal document.

[90] Mertens, A. (2012). Diploma thesis, Karlsruhe Institute of Technology, in preparation (in german).

[91] for Guides in Metrology, J. C. *JCGM 200:2008 International vocabulary of metrology – Basic and general concepts and associated terms (VIM)* (2008).

[92] Cham, J. *phdcomics*. `http://www.phdcomics.com/`.

Acknowledgements

Dank gebürt den folgenden Personen und Institutionen, ohne die die vorliegende Arbeit nicht möglich gewesen wäre:

- dem Karlsuher House of Young Scientists (KHYS) für die Förderung eines dreimonatigem Auslandsaufenthals am Massachussetts Institute of Technology.
- meinem Betreuer Prof. Guido Drexlin, dafür, dass er mir ermöglicht hat, diese Arbeit im Rahmen des KATRIN Experiments anzufertigen und mir dabei immer imt Rat und Tat zur Seite stand.
- Prof. Wim de Boer für die Übernahme des Korreferendariats dieser Arbeit.
- Markus Steidl, Klaus Eitel und Lutz Bornschein für die Vorortbetreuung.
- meinen Korrekturlesern Markus Hoetzel, Stefan Groh, Udo Schmitt und Lutz Bornschein die sich ganz oder teilweise durch dieses Werk gekämpft haben und durch es durch kritische Anmerkungen verbessert haben.
- Markus Hötzel, Alexander Lebschy, Amadeus Dieter und Tobias Bode, die wesentlich zum Gelingen dieser Arbeit beigetragen haben.
- Stefan Groh für die zuverlässige und professionelle Organsation des Pizza Mittwochs sowie Michael Sturm und Marie-Christine Kauffmann für die regelmäßige Rettung vor Kantinen"essen".
- Markus Hötzel, Pascal Renschler, Johannes Schwarz, Michael Sturm, Udo Schmitt, Susanne Mertens, Lutz Bornschein und allen anderen Kollegen am Institut für Kernphysik, dem Institut für Experimentelle Kernphysik, dem Tritiumlabor Karlsruhe und der KATRIN Kollaboration in ihrer Gesamtheit für viele fruchtbare Diskussionen über Physik, Fussball und andere wichtige Dinge im Leben.
- Jorge Cham, der mir immer wieder bewusst gemacht hat, wie schön das Leben als Doktorand doch ist [92].
- meine Eltern und sonstigen Verwandten dafür, dass sie im Laufe der Zeit den Versuch aufgegeben haben, herauszufinden, was ich eigentlich genau mache und wie lange das wohl noch dauern wird.
- Allen, die ich im Eifer des Gefechts vergessen habe.

Erklärung

Ich erkläre hiermit, dass ich die vorliegende Arbeit selbständig verfasst und keine anderen als die angegebenen Quellen und Hilfsmittel verwendet habe.

Eggenstein-Leopoldshafen, den 13. Dezember 2011

Wolfgang Käfer